Study of heavy ion induced fission in a lighter actinide ^{227}Pa using NAND facility

Thesis submitted to the University of Calicut
in partial fulfillment of the requirements
for the award of the degree of

Doctor of Philosophy in Physics

by

N. Saneesh

Under the guidance of

Dr. A. M. Vinodkumar

Department of Physics
University of Calicut
Kerala 673635
India

April 2024

UNIVERSITY OF CALICUT

DR.A.M.Vinodkumar
Professor
Department of Physics

Calicut University P.O.
Kerala INDIA 673 635
Tel: 0494-2407415
Mob: 9645078924
Email: amv@uoc.ac.in

DP/AMV/2024/10/16

16 October 2024

CERTIFICATION OF SUPERVISOR

This is to certify that all the corrections/ suggestions from the adjudicators have been incorporated in the thesis and that the content in the thesis and the soft copy are one and the same.

University of Calicut
Date: 16/10/24

DR.A.M.Vinodkumar

DEPARTMENT OF PHYSICS * UNIVERSITY OF CALICUT * UNIVERSITY OF CALICUT-673635

UNIVERSITY OF CALICUT

CERTIFICATE ON PLAGIARISM CHECK

1.	Name of the Research Scholar	SANEESH. N	
2.	Title of thesis / dissertation	Study of heavy ion induced fission in a lighter actinide ^{227}Pa using NAND facility	
3.	Name of the Supervisor	Dr. A. M. Vinodkumar	
4.	Department/Institution	Department of Physics, University of Calicut, Kerala.	
5.	Similar content (%) identified	Non Core: Introduction/ Theoretical overview/Review of literature/ Materials & Methods/ Methodology	Core: Analysis/Result/Discussion/ Summary/Conclusion/ Recommendations
		5	2
	Acceptable maximum limit (%)	10	10
6.	Software used	iThenticate	
7.	Date of verification	18-04-2024	

*Report on plagiarism check, specifying included/excluded items with % of similarity to be attached.

M.P. MOHAMMED KOYA LIBRARY P.O. CALICUT UNIVERSITY UNIVERSITY OF CALICUT

JAMSHEER N. P.
Assistant Librarian
University of Calicut
Malappuram - 673 635

Checked by (with name , designation & signature)

Name and signature of the Researcher SANEESH. N 22/4/24

Name and signature of the Supervisor. Dr. A. M. Vinodkumar 18-04-2024

The Doctoral Committee* has verified the report on plagiarism check with the contents of the thesis, as summarized above and appropriate measures have been taken to ensure originality of the Research accomplished herein.

Name & Signature of the HoD/HoI (Chairperson of the Doctoral Committee)

Dr. MOHAMED SHAHIN THAYYIL
Professor & Head, Department of Physics
University of Calicut, Kerala (INDIA) - 673635

*In case of languages like Malayalam, Tamil etc..on which no software is available for plagiarism check, a manual check shall be made by the Doctoral Committee, for which an undertaking certificate has to be attached.

DEPARTMENT OF PHYSICS UNIVERSITY OF CALICUT-673635

UNIVERSITY OF CALICUT

DR.A.M.Vinodkumar
Professor
Department of Physics

Calicut University P.O.
Kerala INDIA 673 635
Tel: 0494-2407415
Mob: 9645078924
Email: amv@uoc.ac.in

DP/AMV/2024/4/20

20 April 2024

CERTIFICATE

Certified that the work presented in this thesis entitled 'Study of heavy ion induced fission in a lighter actinide ^{227}Pa using NAND facility' is a bonafide work done by Mr. N. Saneesh under my guidance for the award of the degree of Doctor of Philosophy in Physics, at Department of Physics, University of Calicut, and that this work has not been included in any other thesis submitted previously for the award of any degree and has undergone plagiarism check using *iThenticate* software at C. H. M. K. Library, University of Calicut, and the similarity index found within the permissible limit.

University of Calicut
Date: 20/04/2024

DR.A.M.Vinodkumar

DEPARTMENT OF PHYSICS * UNIVERSITY OF CALICUT * UNIVERSITY OF CALICUT-673635

DECLARATION

I hereby declare that the work presented in this thesis entitled '**Study of heavy ion induced fission in a lighter actinide ^{227}Pa using NAND facility**' is based on the original work done by me under the guidance of Dr. A. M. Vinodkumar, Professor, Department of Physics, University of Calicut, and has not been included in any other thesis submitted previously for the award of any degree. It is also declared that the thesis undergone plagiarism check using *iThenticate* software at C. H. M. K. Library, University of Calicut, and the similarity index found within the permissible limit. I also declare that the thesis is free from AI generated contents.

University of Calicut

Date: 20/4/2024

N. Saneesh

DEPARTMENT OF PHYSICS * UNIVERSITY OF CALICUT * UNIVERSITY OF CALICUT-673635

Publications

International Journals

1. **N. Saneesh**, K.S. Golda, A. Jhingan, S. Venkataramanan, T. Varughese, Mohit Kumar, Meenu Thakur, Ruchi Mahajan, B.R. Behera, P. Sugathan, A. Chatterjee and M.B. Chatterjee, Performance results of National Array of Neutron Detectors (NAND) facility at IUAC.
   Nuclear Instruments and Methods in Physics Research Section A **986**, 164754 (2021).

2. **N. Saneesh**, Divya Arora, A. Chatterjee, K.S. Golda, Mohit Kumar, A.M. Vinodkumar and P. Sugathan, Evaluation of detection efficiency and neutron scattering in NAND detector array: FLUKA simulation and experimental validation.
   Nuclear Instruments and Methods in Physics Research Section A **1013**, 165682 (2021).

3. **N. Saneesh**, Divya Arora, A. Chatterjee, Neeraj Kumar, Anamika Parihari, Chandra Kumar, I. Ahmed, S. Kumar, Mohit Kumar, Akhil Jhingan, K. S. Golda, A. M. Vinodkumar and P Sugathan, Impact of multichance fission on fragment-neutron correlations in ^{227}Pa
   Phys. Rev. C **108**, 034609 (2023).

4. Akhil Jhingan, **N. Saneesh**, M. Kumar, Ruchi Mahajan, Meenu Thakur, Gurpreet Kaur, K. Kapoor, Neeraj Kumar,M. Shareef, R.Dubey, S. Appannababu, E. Prasad, Hardev Singh, K. S. Golda, R. Ahuja, B. R. Behera and P. Sugathan, Development of a time of flight spectrometer based on position sensitive multi-wire proportional counters for fission fragment mass distribution studies
   Review of Scientific Instruments **92**, 033309 (2021).

Conference Proceedings

1. **N. Saneesh**, Divya Arora, Gurpreet Kaur, Mohit Kumar, S.K. Duggi, A.M. Vinodkumar, K. S. Golda, A. Jhingan, A. Chatterjee, and P. Sugathan, Mass gated neutron multiplicity measurements in ^{19}F+ ^{208}Pb system.
   DAE Symp. Nucl. Phys. **63**, 460 (2018).

2. **N. Saneesh**, S. Venkataramanan, Mohit Kumar, and P. Sugathan, Characterization of multiplicity filter module.
   DAE Symp. Nucl. Phys. **63**, 1176 (2018).

3. N. K. Rai, A. Gandhi, A. Sharma, **N. Saneesh**, M. Kumar, G. Kaur, A.Parihari, D. Arora, N. K. Deb, S. Biswas, T. K. Ghosh, K. S. Golda, A.Jhingan, P. Sugathan, B. K. Nayak, and Ajay Kumar, Measurement of neutron multiplicity to investigate the nature of nuclear dissipation.
   DAE Symp. Nucl. Phys. **63**, 396 (2018).

4. Mohit Kumar, Honey Arora, **N. Saneesh**, K. S. Golda, B. R. Behera, A. Jhingan, P. Sugathan, Development of MWPC for detection of evaporation residues in GPSC at IUAC.
   DAE Symp. Nucl. Phys. **64**, 854 (2019).

5. Shruti, H. Arora, **N. Saneesh**, Kajol Chakraborty, D. Arora, Amninderjeet Kaur, Amit, Chetan Sharma, Subodh, K.S. Golda, A. Jhingan, M. Kumar, H. Singh, H.J. Wollersheim, J. Gerl, P. Sugathan, and B.R. Behera, Average Neutron Multiplicty Measurements from the Fission Process of ^{48}Ti+ ^{232}Th System
   DAE Symp. Nucl. Phys. **65**, 221 (2021).

6. **N. Saneesh**, Divya Arora, A. Chatterjee, Neeraj Kumar, Anamika Parihari, Chandra Kumar, I. Ahmed, S. Kumar, Mohit Kumar, Akhil Jhingan,

K. S. Golda, A. M. Vinodkumar, and P. Sugathan, Role of neutron emission in the fission of ^{227}Pa nucleus at medium excitation energies
DAE Symp. Nucl. Phys. **66**, 347 (2022).

7. Divya Arora, **N. Saneesh**, N. Kumar, A. Parihari, M. Kumar, I. Ahmed, S. Kumar, C. Kumar, K.S. Golda, A. Jhingan, J. Gerl, Hans J. Wollersheim, and P. Sugathan, Investigating multi-chance fission via mass gated prescission neutron multiplicty measurement of ^{250}Cf
DAE Symp. Nucl. Phys. **66**, 351 (2022).

Acknowledgements

Walking down memory lane, the last ten years have been decisive in shaping my academic and scientific career. As I come to the end of my Ph.D., I extend my heartfelt gratitude to everyone who has bestowed their love and extended their supporting hands.

It gives me immense pleasure to acknowledge Prof. A M Vinodkumar, my thesis supervisor, for his guidance and constant encouragement. His decades of expertise in Nuclear reactions synergized the scientific content of thesis. His strict time lines for experiment and manuscript helped me to complete the thesis well within the stipulated time.

I want to extend my heartfelt thanks to Dr. Sugathan, Scientist H, my group leader at IUAC, New Delhi. He has been a guiding force for me over the past decade. Working with him has been a blessing, as I have gained essential knowledge in areas like Monte Carlo calculation and nuclear instrumentation. I cannot adequately express my gratitude for his unwavering professional and personal support throughout these years.

Dr. Ambar Chatterjee's over four decades of experience in nuclear physics experiments have been invaluable to me. I am indeed lucky to associate with him and learn various analytical and computational tools at a very initial stage of my carrier. Barring his age, his active participation in all discussions serves as a great motivation for me and others. I wholeheartedly thank Dr. Ambar Chatterjee for his unparalleled suggestions and support.

I express my gratitude to Dr. Avinash Pandey, Director of IUAC, for his unwavering support during this time. His inspiring words continuously drive us forward with passion in the field of science. Additionally, I am thankful to the Former Director, Dr. D Kanjilal, who consistently encouraged our generation to pursue higher education.

I am deeply grateful to Dr. Akhil Jhingan, Scientist G at IUAC, who serves as my group in-charge. His extraordinary skills in the domain of nuclear instrumen-

tation and radiation detectors helped me greatly in understanding the principles of radiation detection and signal processing. I am particularly thankful to him for his valuable suggestions in the development of fission detectors.

I'd like to give a special mention to Dr. Lisha for her insightful suggestions during the initial stages of manuscript preparation. Her support during both the highs and lows of my journey has been invaluable to me.

I am very much thankful to Dr. Golda, Mr. Mohit Kumar, Dr. Madhavan, Dr. Subir Nath, Dr. J. Gehlot, Ms. Gonika and all other Nuclear Physics group members at IUAC for their support and encouragements. I thank Mr. Sunil Ojha and other Pelletron group members for providing quality beams and extending their support round the clock during experiments. I thankfully remember the beam tuning expertise of Mr. N. S. Panwar, whose assistance proved invaluable on numerous occasions during my experiment.

I am thankful to all the teachers of Department of Physics, University of Calicut for all the help and support during the Ph.D period. A special mention to Dr. Libu Alaxander, the coordinator of Ph. D progress presentation, for scheduling my presentation upon request without any hesitation. I fondly remember my friends from the user community of IUAC, Dr. Meenu Thakur, Dr. Ruchi Mahajan, Dr. Gurpreet, Dr. Shareef Muhammad, Dr. Laveen, Dr. Neeraj Kumar, Dr. Visakh, Dr. Jisha P., and Dr. Sanila S. for making various experiments stress free and enjoyable. The experience gained during these experiments have provided a platform to learn new experimental and analytical techniques. I thank my batch mates Rajveer Sharma and Kedar Mal, and the research scholars of IUAC for providing a friendly atmosphere at IUAC.

My strong bond with my family has played a crucial role in making me. My parent's commitment and sincerity towards the tiniest of things have a profound influence in my life. I am indebted to my family for their unconditional love. To Chandu and Tanu, whose smiling faces and quanta of energy keep me going forward every single day.

Contents

List of Figures **vii**

List of Tables **xi**

1 Introduction **1**

1.1 Bohr - Wheeler theory 3

1.1.1 Fission width (Γ_f) 5

1.1.2 Particle emission width (Γ_ν) 9

1.2 Shell effects 11

1.3 Influence of angular momentum on fission 13

1.4 Statistical model of compound nucleus decay 15

1.5 Challenges in heavy ion induced fission studies 17

1.5.1 Need of dynamical calculations 17

1.5.2 A semi-empirical approach : GEF model 18

1.6 Motivation of the thesis 20

1.7 Outline of the thesis 24

Bibliography 26

2 Development of a multi-neutron detector facility and its performance evaluation **31**

2.1 Importance of neutron measurements 31

2.2 Multi-neutron detector facility at IUAC 32

2.3 Nuclear radiation detectors 34

2.3.1 Neutron detectors : BC501A 34
2.3.2 Fission fragment detectors : MWPC 36
2.3.3 Design and development of MWPC detectors 36
2.4 Electronics 39
2.4.1 Pulse shape discrimination (PSD) module 39
2.4.2 Fast-timing pre-amplifiers 40
2.4.3 High voltage supplies for PMTs of BC501A 41
2.5 Data acquisition system 41
2.6 Performance evaluation of BC501A detectors 42
2.6.1 Energy linearity 43
2.6.2 n - γ discrimination 45
2.6.3 Timing response 46
2.7 Performance evaluation of MWPC detectors 47
2.7.1 Two-dimensional position information 48
2.7.2 Linearity 50
2.7.3 Timing response 52
2.8 Measurement of cross-talk probability 53
2.9 Beam dump radiation shield 55
2.10 In-beam measurements 57
2.11 Summary Conclusion 60
Bibliography 62

3 Measurements and Monte Carlo calculations of various detector features 68

3.1 Experimental method for efficiency measurement 70
3.2 Neutron energy spectrum of ^{252}Cf 71
3.3 Experiment description 74
3.3.1 The detectors 74
3.3.2 Experimental setup 75
3.3.3 Signal processing and data collection 76

3.4 FLUKA simulation of BC501A characteristics 79
3.4.1 Validation of FLUKA simulation 80
3.4.2 Estimation of α, β and γ values for NAND detector . . . 82
3.4.3 Simulation of recoil proton response 84
3.4.4 Intrinsic efficiency of 5" $\times$ 5" BC501A detectors 86
3.5 Scattering of neutrons by materials 88
3.6 Estimation of neutron emission flux 90
3.7 Summary and conclusions 91
Bibliography 93

4 Measurement of mass distribution and neutron multiplicity in ^{227}Pa : Experimental aspects 99
4.1 Pelletron Accelerator at IUAC 101
4.2 Target details 103
4.3 Measurement techniques 104
4.4 Experimental setup 105
4.4.1 Fission detectors : MWPC 106
4.4.2 Neutron detectors : BC501A 107
4.5 Signal processing electronics and data acquisition 109
Bibliography 116

5 Data analysis methods 119
5.1 Data analysis to find mass distribution and TKE of fission fragments 120
5.1.1 Velocity reconstruction method 122
5.1.2 Energy loss correction 126
5.2 Analysis methods to find average neutron multiplicity 127
5.2.1 Measurement of neutron kinetic energy 131
5.2.2 Moving source model : Kinematic calculation 132
5.2.3 Moving source model : Watt formula 135
5.2.4 Relative angle between neutron sources and neutrons . . . 136

5.3 Mass gated pre-scission neutron multiplicity 139
Bibliography 141

6 Results and discussion : Impact of multi-chance fission 144

6.1 Results of mass distribution, $< \nu_{pre} >$ and mass gated ν_{pre} measurements 145
6.1.1 Mass distribution 146
6.1.2 Average neutron multiplicity 148
6.1.3 Mass gated pre-scission neutron multiplicity 150
6.2 GEF model calculations 151
6.3 Validation of GEF model calculation 153
6.4 Multi-chance fission and its impact on experimental observables . 154
6.4.1 Mass distribution : Theory and measurements 154
6.4.2 $Mass$ - TKE correlation : GEF model 156
6.4.3 $Mass$ - TKE correlation : Measurements 159
6.4.4 $Mass$ - ν_{pre} correlation 160
6.5 Summary and Conclusion 163
Bibliography 165

7 Summary and future outlook 168

Bibliography 173

List of Figures

1.1 A schematic representation of potential energy of an excited compound nucleus used in the Bohr - Wheeler theory to describe the fission process. E^* and $E^* - B_f - \epsilon$ represent the excitation energies at the ground state and saddle point. 6

1.2 Potential energy as function of elongation calculated according to the liquid drop model, and macro-microscopic approach 12

1.3 RLDM calculations showing the changes in ground state and saddle point energies with increase in L. 14

1.4 A schematic representation of heavy ion collision with a target nucleus and subsequent evolution of the di-nuclear system. 15

1.5 A conceptual view of multi-chance fission 19

1.6 Mass distribution of fragments of the U, Np, and Pu isotopes at different excitation energies 21

2.1 A photograph of the National Array of Neutron Detectors facility. 33

2.2 Pictorial representation of scintillation pulses from an organic liquid scintillator 35

2.3 A schematic of the electrode configuration of MWPC detectors. . 37

2.4 Test results of *Rhombus delay chips* used for finding the position information in X and Y direction 38

2.5 Photograph of an MWPC detector after assembling the electrodes. 39

2.6 Light output spectrum of monoenergetic γ-rays from ^{137}Cs. 43

2.7 The response linearity of BC501A detectors for recoil electron energy ranging from ≈ 0.3 MeV to 4.15 MeV. 44
2.8 The histogram showing $n - \gamma$ discrimination based on Z/C technique at 120 KeVee threshold from a BC501A detector. 45
2.9 A block diagram of signal processing electronics used for the offline examination of MWPC detectors. 48
2.10 Raw position signals extracted from the ends of X and Y position electrodes. 49
2.11 Interaction positions derived from the raw position signals. 50
2.12 Position response linearity of an MWPC detector. 51
2.13 Time of flight spectrum of elastically scattered ^{48}Ti beam detected using MWPC. 52
2.14 Schematic representation of a segment of NAND detectors used for cross-talk measurement. 53
2.15 TOF spectra of neutrons and γ rays from ^{252}Cf. 57
2.16 Two dimensional histograms showing n-γ discrimination. 58

3.1 The distribution of nuclear temperature as function of fragment mass. 72
3.2 Vector diagram showing the emission of neutrons from an accelerated fragment and the interdependence of velocity vectors in c.m. and laboratory frame. 73
3.3 Schematic of the experimental setup and electronics for signal processing and data collection. 75
3.4 Histograms representing various parameters measured in the experiment 77
3.5 Measured intrinsic efficiency, in percentage, of a 5" × 5" BC501A detector as a function of neutron energy. 79
3.6 Pulse height distribution for 511 keV γ-rays for a 5" × 5" BC501A detector. 83

3.7 Measurement and simulation of light output for monoenergetic neutrons 86
3.8 The intrinsic efficiency of 5" × 5" organic scintillator, BC501A as function of incident neutron energy. 87
3.9 Spatial distribution of normalized neutron fluence, after scattering from 4 mm thick sample material. 89

4.1 A schematic of the Pelletron accelerator facility at IUAC. 102
4.2 Schematic view of the experiment setup used for measuring neutron multiplicity in coincidence with fission. 105
4.3 Inside view of the scattering chamber. 107
4.4 Images of signals derived from MWPC and BC501A detectors. . . 109
4.5 Signal processing electronics for fission detectors. 110
4.6 Signal processing electronics for neutron detectors. 110
4.7 A block diagram of electronics used for the analog signal processing and data acquisition. 112
4.8 Figure shows a typical coincidence condition applied for binary fission measurements. 113
4.9 Histograms representing various signals of the MWPC detectors . 114
4.10 Histograms represent various signals acquired from a BC501A detector. 115

5.1 A schematic of co-ordinates (θ,ϕ) of the hit position of one of the fragments 120
5.2 Velocity vector diagram of fission fragments in the laboratory and centre of mass frames. 123
5.3 Time of flight correlation of complementary events recorded using two MWPC detectors for ^{19}F+^{208}Pb reaction. 125
5.4 *Energy per nucleon* versus *range* relationship of fission fragments . 126
5.5 Spatial distribution of neutron fluence emitted by moving sources. 129

5.6 Kinetic energy distribution of neutrons emitted by moving sources at various angles. 130
5.7 Two dimensional plot of time of flight versus zero-cross over recorded in a BC501A detector. 132
5.8 Velocity vector diagram of neutrons emitted by a moving source. . 134
5.9 The Cartesian co-ordinate system, defining relative angles with respect to the direction of CN and fission fragments. 137

6.1 Mass distribution of fission fragments at three excitation energies. 146
6.2 Examples of the three-moving-source fits to double differential neutron multiplicity spectra. 149
6.3 Distribution of total kinetic energy of fission fragments as function of mass. 150
6.4 Pre-scission neutron multiplicity measured for ^{227}Pa in the range of E* = 24.2 - 59.6 MeV. 153
6.5 Comparison of experimental mass distribution with GEF model calculations. 155
6.6 GEF predicted $Mass$ - TKE correlations for ^{227}Pa at different excitation energies. 158
6.7 Comparison of experimental $Mass - TKE$ correlations in ^{227}Pa with GEF calculations. 159
6.8 Correlation between experimental ν_{pre} and fragment mass compared with GEF model calculation. 161

List of Tables

2.1 Cross talk probability between two detectors as a function of distance. 55

2.2 Comparison of neutron multiplicity measurements in super heavy mass region with a reference reaction. 59

3.1 FLUKA calculation of neutron detection efficiencies for 6" × 2" organic scintillator at different energy thresholds. 82

3.2 Neutron flux on neighbouring detectors after interactions from 4mm thick material placed in neutron beam path. 90

4.1 The relative angles θ_n, θ_{nf1}, and θ_{nf2} of BC501A detectors N1 - N16, used in the present experiment. 108

6.1 Results of three-Gaussian fit to the mass distribution 148

6.2 Experimentally obtained pre-scission neutron multiplicities of ^{227}Pa at different excitation energies. 150

6.3 Results of the coupled channels calculation to estimate the average angular momentum of the compound nucleus. 152

6.4 GEF model calculation showing the probabilities of various fission chances. 157

Chapter 1

Introduction

In 1938, Otto Hahn and Fritz Stassmann observed a strange disintegration in their study of uranium irradiation with thermal neutrons. They were astonished to discover that when uranium (Z = 92) was bombarded with thermal neutrons, it resulted in the creation of barium (Z = 56), rather than the expected lighter actinides (Z = approximately 90) or transuranium elements (Z > 92). In the letter to the editor, they wrote, *"As chemists we really ought to revise the decay scheme and insert the symbols Ba (Z=56), La (Z=57), Ce (Z=58), in place of Ra (Z=88), Ac (Z=89), Th (Z=90). However, as nuclear chemists working very close to the field of physics, we cannot bring ourselves yet to take such a drastic step, which goes against all previous experience in nuclear physics. There could perhaps be a series of unusual coincidences that have given us false indications"* [1]. What made them so hesitant to announce a discovery that later won the Nobel Prize and redefined the centres of global power? It was in this process, a huge transfer of mass between the parent and daughter nuclei was observed, unlike the well-known alpha or beta decay, where the atomic number of the daughter nuclei changes by one or two units up or down in the periodic table. Unlike the celebrated discovery of Higgs boson in 2012, which was predicted theoretically in 1964, the discovery of fission was unexpected and entirely against the then understanding of nuclear reactions.

Why was the possibility of fission ignored completely? The prime reason was the consensus that nothing heavier than an alpha particle could be emitted in a nuclear decay. This assumption was heavily influenced by Gamow's theory of alpha decay, published in 1928, which provided substantial theoretical backing to this notion [2]. According to Gamow's theory, the probability of barrier penetration decreases exponentially w.r.t. $\sqrt{Z_b Z_B Q}$, where Z_b and Z_B are the atomic numbers of daughter nuclei and Q is the energy released in the decay process. As Z_b and Z_B become close to each other, the product $Z_b Z_B$ becomes large, and the probability for the emission of particles heavier than alpha becomes very low. Considering the capture of a thermal neutron by uranium, the probability for symmetric fission ($Z_b \approx Z_B$) is $\approx 10^{-453}$ times less probable than alpha emission [3]. Such calculations would have instilled immense confidence to ignore any notions of nuclear fission. However, it is essential to note that these calculations heavily depend on the validity of the direct-reaction mechanism [3].

Lise Meitner, who was part of Hahn's research group, recognized that the behavior of heavy nuclei under neutron bombardment differed significantly from the quantum mechanical picture given by Gamow's theory. So, Meitner and Robert Frisch treated the problem classically, where the heavy nucleus resembled a charged liquid drop [4, 5]. Just as molecules within a drop move collectively, they postulated that nucleons would behave similarly. The concept of surface tension of the nucleus from Bohr's theory, published in 1937, was invoked to account for the attractive forces that bind the nucleus. As the nucleus becomes very heavy, the Coulombic repulsion among protons diminishes the surface energy. The nucleus would remain stable against fission until the surface energy balanced the electrostatic forces. Through a rough estimation, they determined that for Z $\approx$ 100, the Coulombic repulsion entirely cancels out the surface energy [5].

For extremely heavy nuclei such as uranium, with Z close to 100, the fission barrier would be relatively small. They hypothesised that in such nuclei, if the

collective motion of nucleons is made violent by adding energy, like neutron capture, the drop may divide itself into two smaller drops. Further, Meitner and Frisch estimated the total kinetic energy of fission fragments to be around 200 MeV [4]. Later, Frisch performed experiments employing ionization chambers and detected the large pulses generated by fission fragments in the energy range of $\approx$ 200 MeV [6]. Thus, far from being impossible, fission becomes an inevitable feature in the decay of very heavy nuclei under violent perturbation. In nearly six months after the discovery of fission, Niels Bohr and John Wheeler formulated the first mathematical framework to explain the phenomenon [7]. Bohr-Wheeler theory, even today, remains the foundation for most of the theoretical endeavours to explain various aspects of fission phenomena.

1.1 Bohr - Wheeler theory

Bohr and Wheeler developed on a comprehensive theoretical analysis of the fission process, aiming to address some key questions such as the energy released per fission, the stability of the nucleus under deformation, and the fission decay width. Initially, the energy release per fission was qualitatively assessed and later confirmed through experiments by Meitner and Frisch [4, 6]. The remaining two significant aspects are briefly addressed in this section. In Bohr - Wheeler theory, a nucleus is resembled to a charged liquid drop, a concept first proposed by Gamow in 1930 [8]. According to this theory, a nucleus is considered as a uniformly charged, incompressible liquid drop held together by nuclear forces. To analyze the energetics of the nucleus, Weizsacker's semi-empirical formula was used. The Semi-empirical formula describes the binding energy of the nucleus of atomic number Z and mass number A in the following form,

$$B_{LDM}(A,Z) = a_v A - a_s A^{2/3} - a_c \frac{Z(Z-1)}{A^{1/3}} - a_A \frac{(A-2Z)^2}{A} + a_p \frac{[(-1)^N + (-1)^Z]}{2A^{3/4}} \tag{1.1}$$

where N is the neutron number, a_v, a_s, a_c, a_A, and a_p represent the coefficients of the volume, surface, Coulomb, asymmetry, and pairing energy terms, respectively, in the binding energy formula. The nuclear stability against deformation was formulated by considering a small distortion of a spherical nucleus.

Consider a small axially symmetric deformation in a spherical nucleus. The radius of the deformed nucleus can be written as:

$$R(\theta) = R_0\Big[1 + \sum_l \alpha_l P_l(cos\theta)\Big] \tag{1.2}$$

where R_0 is the radius of the undeformed spherical nucleus, θ is the angle of the radius vector with respect to the body fixed frame of the nucleus, and α is the deformation parameter. Higher-order terms above $l = 2$ are neglected, considering small distortions. The deformation causes changes in surface (E_S) and Coulomb energies (E_C) terms of the formula 1.1. The change in E_S can be written in terms of the surface energy of the undeformed nucleus (E_{S0}) as follows:

$$\Delta E_S = E_S - E_{S0} = E_{S0}\ \frac{2}{5}\ \alpha_2^2 \tag{1.3}$$

Similarly, the change in E_C can be written as,

$$\Delta E_C = E_C - E_{C0} = E_{C0}\ \frac{-1}{5}\ \alpha_2^2 \tag{1.4}$$

where E_{C0} is the Coulomb energy of undeformed nucleus. Thus the total change in energy due to the deformation is,

$$\Delta E = \Delta E_S + \Delta E_C = \frac{1}{5}\ \alpha_2^2\ (2\ E_{S0} - E_{C0}) \tag{1.5}$$

In essence, the Bohr-Wheeler theory shows that nuclear stability against fission is dictated by a balance between the surface and Coulomb energies of the undeformed nucleus. The condition $\Delta E = 0$ implies that the surface energy is

counterbalanced by the Coulomb energy, and then the nucleus undergoes spontaneous fission.

The fissionability of nuclei is quantitatively expressed by *fissility* (χ), defined as,

$$\chi = \frac{E_{C0}}{2\ E_{S0}} = \frac{Z^2/A}{2\ a_s/a_c} = \frac{Z^2/A}{(Z^2/A)_{crit.}} \tag{1.6}$$

From the coefficients of surface and Coulomb terms of binding energy formula, we can estimate $(Z^2/A)_{crit.} = (2\ a_s/a_c) \approx 50$. By incorporating isospin of the nucleus, $(Z^2/A)_{crit.}$ can be parametrized as,

$$(Z^2/A)_{crit.} = 50.0883\ \left[1 - 1.7828\ \left(\frac{N-Z}{A}\right)^2\ \right] \tag{1.7}$$

$\Delta E = 0$ gives $\chi = 1$, and the system becomes critically unstable against fission. For lighter nuclei, $\chi < 0.65$, and for heavier nuclei in the actinide region, $1.0 < \chi < 0.65$. Lower values of χ signify less fissionable or more stable nuclei, and vice versa for higher values of χ.

1.1.1 Fission width (Γ_f)

The decay width (Γ) of a process is a measure of the probability of the process occurring within a given amount of time. In the Bohr - Wheeler theory, it is assumed that the compound nucleus (CN) is equilibrated in all degrees of freedom. Light particle emission and fission are two mutually competing decay modes whose relative probability or emission width is decided by the excitation energy and angular momentum (E^*, l). The calculation of fission width (Γ_f) is described as follows: Bohr - Wheeler theory pictures fission as the shape evolution of the compound nucleus from the ground state configuration towards scission against the potential energy barrier [7]. The probability of this transition is governed by the density of the states available at the ground state and the transition state, called the saddle point. A typical potential energy curve of an

excited CN as a function of deformation is shown in the Figure 1.1.

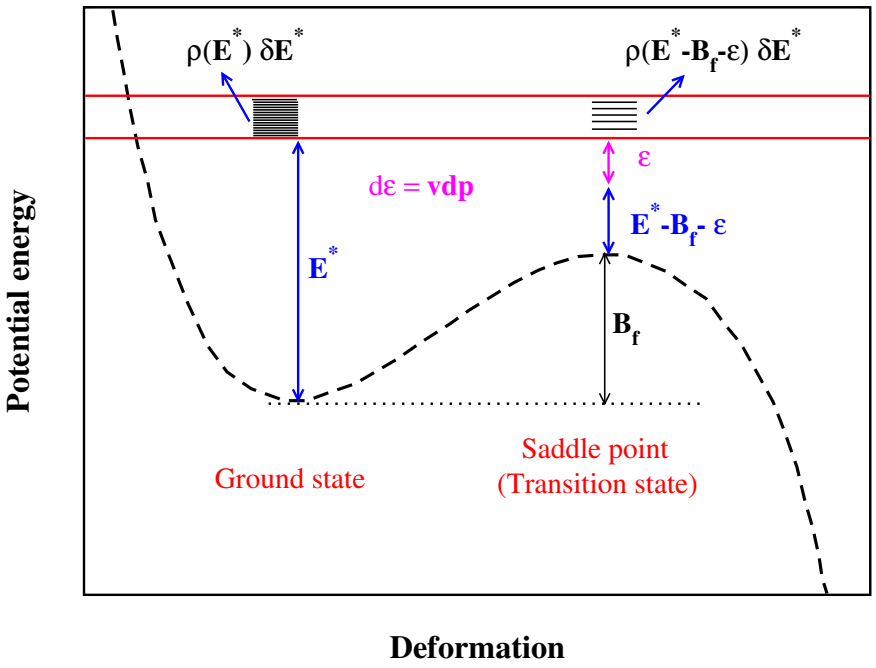

Figure 1.1: A schematic representation of potential energy of an excited compound nucleus used in the Bohr - Wheeler theory to describe the fission process. E^* and $E^* - B_f - \epsilon$ represent the excitation energies at the ground state and saddle point.

Let $\rho(E^*)$ be the density of states at the ground state of the CN at an excitation energy E^*. So, the number of intrinsic states between the energy E^* and δE^* is given by $\rho(E^*)\ \delta E^*$. Under the assumption that the number of nuclei and available states are equal (one nucleus at each state), we can write the number of nuclei in the ground state as $\rho(E^*)\ \delta E^*$. Similarly, from the Figure 1.1, the number of intrinsic states at the saddle point can be written as $\rho(E^* - B_f - \epsilon)\ \delta E^*$ where ϵ is the collective kinetic energy of elongation and B_f is the fission barrier. Let v and p be the speed and momentum associated with the collective motion. The number of states passing over the saddle point is estimated from the number of collective states whose momenta lies between p and $p + dp$. The number of collective states at the saddle point is given by $vdp/h = d\epsilon/h$. Knowing this, the number of nuclei a crossing the barrier per unit time can be obtained from the product of the number of collective states

and the number of intrinsic states.

$$a = (d\epsilon/h)\ \rho(E^* - B_f - \epsilon)\delta E^* \tag{1.8}$$

Therefore, the total number of nuclei (A) crossing the barrier per unit time,

$$A = \int_0^{E^*-B_f} a = \frac{\delta E^*}{h} \int_0^{E^*-B_f} \rho(E^* - B_f - \epsilon)d\epsilon \tag{1.9}$$

From this, the fission probability per unit time, also called the fission rate, is calculated as the ratio of the number of nuclei crossing the saddle point per unit time to the number of nuclei in the ground state,

$$fission\ rate,\ r = \frac{(\frac{\delta E^*}{h}) \int_0^{E^*-B_f} \rho(E^* - B_f - \epsilon)d\epsilon}{\rho(E^*)\delta E^*} \tag{1.10}$$

$$r = (\frac{1}{h}) \frac{\int_0^{E^*-B_f} \rho(E^* - B_f - \epsilon)d\epsilon}{\rho(E^*)} \tag{1.11}$$

According to the radioactive decay law,

$$N = N_0\ e^{-rt} = N_0\ e^{-\frac{t}{\tau}} \tag{1.12}$$

$$\Gamma_{BW} = \frac{\hbar}{\tau} = \frac{\int_0^{E^*-B_f} \rho(E^* - B_f - \epsilon)d\epsilon}{2\pi\rho(E^*)} \tag{1.13}$$

In other words, Bohr - Wheeler theory shows that the fission width is solely dependent on the total number of intrinsic states available at the saddle point and level density at the ground state. Equation 1.13 shows that the precise calculation of level density is very essential to estimate the fission width. The formalism used for the calculation of level density is described in the following subsection.

Nuclear level density

The Fermi gas model is one of the simplest models used for calculating the level density of excited nuclei of energy E^*. According to the Fermi gas model, the level density $\rho(E^*)$ is related to E^* in the form,

$$\rho(E^*) = C \ \exp\left(2\sqrt{aE^*}\right) \tag{1.14}$$

where C is a constant and a is the level density parameter which is related to the nuclear temperature by the relation, $T = \sqrt{(E^*/a)}$.

In the case of heavy ion induced fission, the projectile imparts significant angular momentum to the compound nucleus. The level density shows a strong dependence on angular momentum. Therefore, angular momentum dependent formalism for level density has to be used to estimate fission width in heavy ion induced fission studies. The angular momentum dependent level density formula proposed by Bohr and Mottelson [9] is given by,

$$\rho(E^*, l) = \left(\frac{2l+1}{24}\right) \left(\frac{\hbar^2}{2I}\right)^{3/2} \left(\frac{\sqrt{a}}{E^{*2}}\right) \exp(2\sqrt{aE^*}) \tag{1.15}$$

where I is the rigid body moment of inertia about the axis of rotation and E^* is the available thermal energy given as $E^* = E - \frac{l(l+1)\hbar^2}{2I}$. An approximate form of fission width can be derived using Equations 1.13 and 1.15 under the condition $E^* >> B_f$. Equation 1.13 becomes,

$$\Gamma_{BW} = \frac{1}{2\pi} \int_0^{E^*-B_f} \left(\frac{E^*}{E^* - B_f - \epsilon}\right)^2 \ \exp\left(2\sqrt{a\big(E^* - B_f - \epsilon\big)} - 2\sqrt{aE^*}\right) d\epsilon \tag{1.16}$$

At higher excitation energies, $E^* >> B_f$, $\left(\frac{E^*}{E^*-B_f-\epsilon}\right)$ will be ≈ 1, and on further simplification, we get the following simplified form to Bohr - Wheeler

fission width,

$$\Gamma_{BW} = \frac{T}{2\pi}\ \exp\left(-\frac{B_f}{T}\right) \tag{1.17}$$

where T is the nuclear temperature. After the inclusion of collective degrees of freedom in the ground state of the CN [10], Equation 1.17 has been modified to the following form :

$$\Gamma_f = \Gamma_f^{BW}\ \frac{\hbar\omega}{T} \tag{1.18}$$

$$\Gamma_f = \left(\frac{\hbar\omega}{2\pi}\right)\ \exp\left(-\frac{B_f}{T}\right) \tag{1.19}$$

where ω is the frequency of harmonic oscillator potential at the ground state. For an excited compound nucleus, particle emission is another prominent decay channel that competes with fission. To estimate the probability of fission decay, the emission widths of particles have to be accounted.

1.1.2 Particle emission width (Γ_ν)

The probability of particle emission (neutrons or charged particles), which competes with fission decay at higher excitation energy, was calculated from statistical arguments presented by Weisskopf [11]. Consider the emission of a particle from a compound nucleus A at excitation energy E^* that forms a daughter nucleus B,

$$A(E^*) \rightarrow B + n \tag{1.20}$$

Let ϵ be the kinetic energy of the emitted particle and E_0 be its binding energy. Then the excitation energy of B will be $E_B{=}E^* - E_0 - \epsilon$. Let $W_n(\epsilon)d\epsilon$ be the probability per unit time of the emission of the particle with kinetic energy between ϵ and $\epsilon + d\epsilon$. It is possible to calculate $W_n(\epsilon)d\epsilon$ as function of the inverse

cross-section $\sigma(E^*, \epsilon)$ in the following form [11],

$$W_n(\epsilon)d\epsilon = \sigma(E^*, \epsilon)\ \frac{n\ m}{\pi^2\hbar^3}\ \frac{\rho_B(E_B)}{\rho_A(E^*)}\ \epsilon\ d\epsilon \tag{1.21}$$

where m is the mass of the emitted particle, n denotes the number of states for the spin of the particle, $\rho_B(E_B)$ and $\rho_A(E^*)$ are the number densities of the daughter and parent nuclei, respectively. For particles of spin s, n is given by $(2s+1)$. Inverse cross-section is the mean cross-section for the collision of a particle of kinetic energy ϵ with a nucleus at excitation energy $E^* - E_0 - \epsilon$ to form a CN at excitation energy E^*. The total probability per unit time is then obtained by integrating $W_n(\epsilon)d\epsilon$ w.r.t. ϵ as,

$$rate = \frac{1}{\tau} = \int W_n(\epsilon)d\epsilon \tag{1.22}$$

Finally, the emission width of a particle of type i is obtained by the following formula,

$$\Gamma_i = \frac{(2s_i+1)\ m_i}{\pi^2\ \hbar^2}\ \frac{1}{\rho_A(E^*)}\ \int \rho_B(E_B)\ \sigma(E^*, \epsilon)\ \epsilon\ d\epsilon \tag{1.23}$$

The inverse cross-section can be determined by the classical conception: any particle hitting the nucleus will be absorbed [11]. This corresponds to the geometrical cross-section, without considering the energy dependence in the interaction. Then we get the expression,

$$\sigma(E^*, \epsilon) = \sigma_0\big(1 - \frac{V}{\epsilon}\big)\ if\ \epsilon > V \tag{1.24}$$

$$= \ 0 \qquad\qquad if\ \epsilon < V \tag{1.25}$$

$$\sigma_0 = \pi R^2\ ;\ V = Z_1 Z_2 e^2/R \tag{1.26}$$

where R is the radius of the nucleus and V is the Coulomb energy.

The liquid-drop model (LDM) of the nucleus is quite successful in accounting for the general collective behavior of nuclei. It provides an understanding of

the fission process on the basis of the competition between the cohesive nuclear force and the disruptive Coulombic repulsion between protons. But it does not provide an accurate description of nuclear properties such as the extra-stability of certain nuclei, fission barrier systematics or the ground-state masses of nuclei, as well as asymmetry in the mass distribution during actinide fission. These discrepancies have been attributed to microscopic factors, notably the presence of shell structures similar to electron shells in atoms. Another notable deviation from the LDM prediction is the rapid decline of fission barriers at higher angular momentum in the compound nucleus. Addressing this, angular momentum effects have been incorporated into the LDM framework, giving rise to the Rotating Liquid Drop Model (RLDM).

1.2 Shell effects

Shell effects generally refer to the influence of the shell structure of nucleons on the evolution of an excited CN. To investigate this, a microscopic approach known as the shell model has been developed, based on the mutual interactions among nucleons within a nucleus. Though the Shell model calculation accounts for many nuclear properties, a completely quantitative microscopic calculation to describe properties like nuclear mass, fission barrier, etc. was difficult. A major breakthrough emerged in 1967 when V. M. Strutinsky introduced a macro-microscopic model that incorporates microscopic shell effects as a correction to the macroscopic liquid drop energy [12]. The model assumes nucleon shells and other quantum effects as a small deviation from the homogeneous distribution considered in the liquid drop model. This energy difference, which is the correction to LDM energy, can be expressed as,

$$\delta U = U - \bar{U} \tag{1.27}$$

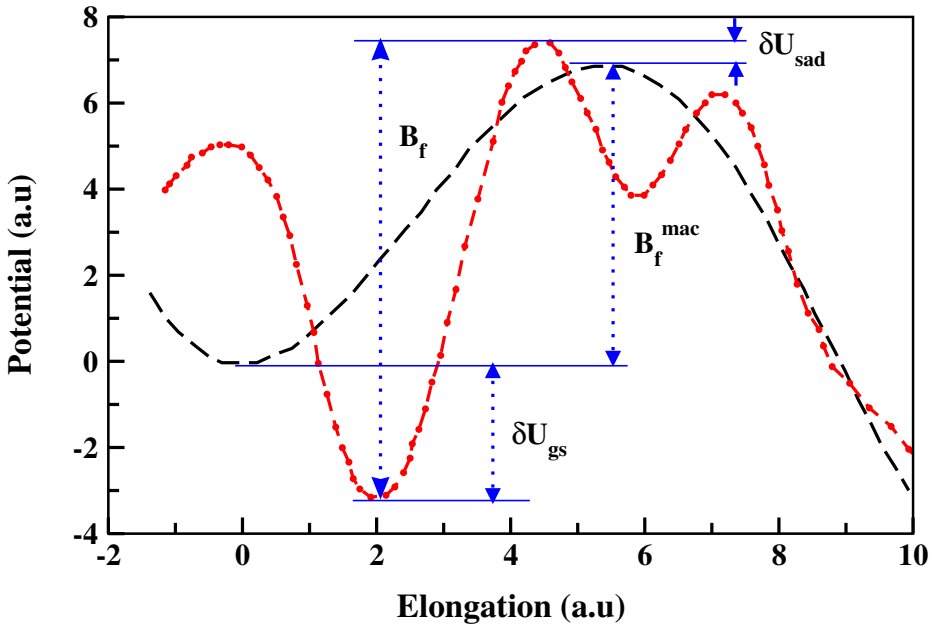

Figure 1.2: Potential energy as function of elongation calculated according to the liquid drop model, and macro-microscopic approach [13].

where U represents the energy corresponding to the "shell" quantal distribution and $\bar{U}$ is that of the uniform distribution [12]. Shell correction manifests as a modification in nuclear masses denoted as, $\delta M = M_{exp} - M_{LDM}$. Figure 1.2 highlights the importance of shell correction. This figure presents a schematic drawing of the potential energy as a function of elongation relative to the macroscopic ground state energy of a nucleus. The dashed (black) and dot-dashed (red) curves, respectively show the potential energies calculated using LDM, and the LDM after incorporating shell corrections. Shell effect modifies the fission barrier (B_f) predicted by LDM as,

$$B_f \approx B_f^{mac} - \delta U_{shell} \approx B_f^{mac} - \delta M \tag{1.28}$$

where B_f^{mac} is the macroscopic barrier calculated using the liquid drop model, and δU_{shell} is the shell correction energy mainly at the ground-state.

The shell structure also modifies the nuclear level density. Therefore, it is crucial to incorporate the shell correction to the level density, as well as the damping of shell effects with excitation energy. Typically, phenomenological

relations are used to describe the thermal damping of the shell effects. Ignatyuk's formula [14] is one such widely used formula that incorporates the shell effect and its attenuation with increase in excitation energy, as

$$a(E^*) = \bar{a}\Big(1 + \frac{\delta M}{E^*}\ f(E^*)\Big) \tag{1.29}$$

$$f(E^*) = 1 - \exp(-E^*/E_D) \tag{1.30}$$

where $\bar{a}$ is the asymptotic level density parameter derived from the Fermi-gas model, and E_D(or $\gamma = 1/E_D$) defines the rate at which shell effects diminish with rising excitation energies. γ has typical values between 0.04 to 0.07 MeV^{-1} [15].

1.3 Influence of angular momentum on fission

The advent of heavy ion beams has opened up new paths in fission research. One significant opportunity it offers is the investigation of fission at extremely high angular momentum (L) of CN. Bohr-Wheeler theory calculates the potential energy of the nucleus from the counter-acting surface and Coulomb energies; not showing any dependence of L on the fission barrier. Since the rotational energy acts in concert with the disruptive Coulomb forces, a decrease in fission barrier can be expected with increase in L. To address this, Cohen, Plasil, and Swiatecki introduced the Rotating Liquid Drop Model (RLDM) [16]. According to RLDM, the effective potential energy of a rotating, incompressible, uniformly charged liquid drop is given by

$$E_{eff} = E_S + E_C + E_R \tag{1.31}$$

where E_S and E_C are surface and Coulomb energies. The rotational energy E_R is given by $E_R = \frac{L^2}{2I}$, where I is the moment of inertia of the configuration.

The liquid drop model by Cohen and Swiatecki [17, 18] suggests a spherical ground states, whereas the shapes at the saddle point are elongated. Conse-

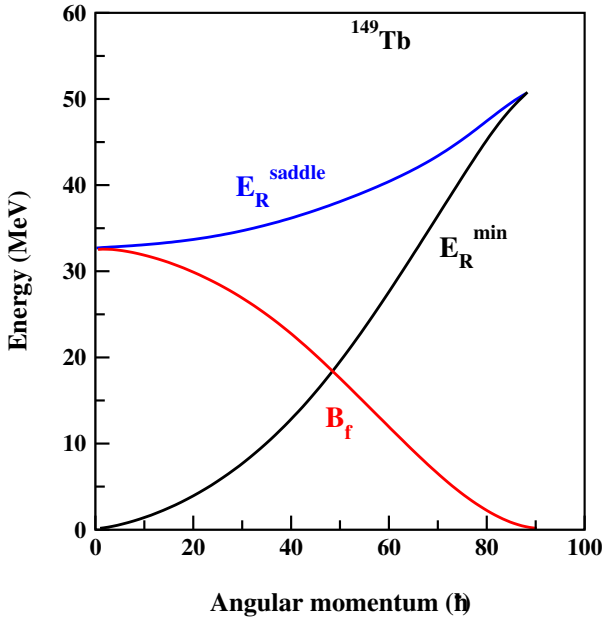

Figure 1.3: RLDM calculations showing the changes in ground state (E_R^{min}) and saddle point (E_R^{saddle}) energies with increase in L for ^{149}Tb. The black and blue solid lines respectively show the increase in E_R^{min} and E_R^{saddle} with increase in L. The difference of these two curves, B_f, is also shown (red solid line) [19].

quently, as L increases, assuming the shapes remain constant, rotational energy both at the ground state (E_R^{min}) and saddle point (E_R^{saddle}) increases, as shown in Figure 1.3. However, E_R^{min} increases more rapidly than E_R^{saddle} of the elongated saddle-point shape. Eventually, at some higher value of L, typically $L < 100\ \hbar$, the ground state energy becomes equal to the saddle point energy. In this simple shape-constrained picture, this is the point at which the fission barrier (B_f=$E_R^{saddle} - E_R^{min}$) vanishes. In essence, angular momentum imposes an absolute limit towards the stability to all nuclei.

It is crucial to note that as nuclei rotate, their shapes do change with increasing angular momentum. In fact, these changes in shape and the resulting changes in energy form the foundation of the RLDM [16]. Though RLDM provided a qualitative description of the impact of angular momentum, comparison with measurements [20, 21] has shown that the theory overestimates the fission barrier. To address this limitation, improvisations were made in the Rotating Finite-Range Model (RFRM), introduced by Mustafa *et al.* [22], and A. J. Sierk

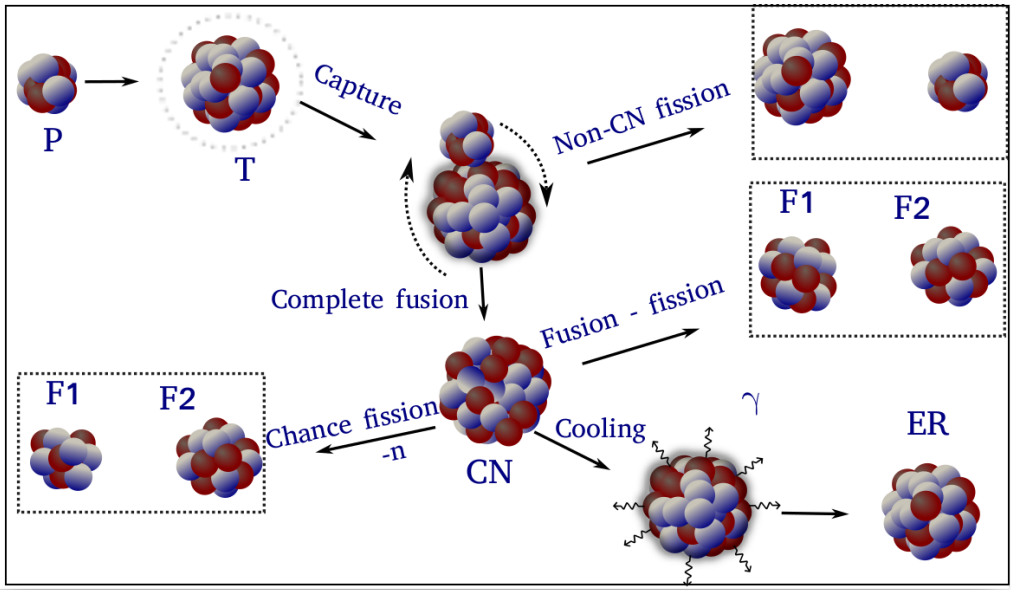

Figure 1.4: A schematic representation of heavy ion collision with a target nucleus and subsequent evolution of the di-nuclear system.

[23]. RFRM demonstrated remarkable improvement in quantitative predictability of fission barrier [24].

1.4 Statistical model of compound nucleus decay

Figure 1.4 is a schematic representation of a typical heavy ion collision and the subsequent evolution of the composite system. The composite system formed by the capture of a heavy ion projectile with the target can undergo various exit channels, as depicted. An early re-separation of the composite system before equilibration ends up in non-compound fission path known as quasi-fission. Conversely, the equilibration in all degrees of freedom results in the formation of compound nucleus (CN). Depending on the impact parameters of collision, the spin of the CN will be distributed among the allowed L values. Moreover, the decay of this CN through particle emission opens up numerous additional channels with different (E^*, L) values. For such complex many-body systems with a large number of possible states, it is difficult or impossible to study the full microscopic dynamics. An appropriate method to deal such systems is statistical

approach. Bohr-Wheeler theory, discussed earlier, is one such theory developed with statistical framework to describe the fission process.

Bohr-Wheeler theory computes the fission width (Γ_f) from the total number of intrinsic states at the saddle point and the intrinsic level density at the ground state as expressed by Equation 1.13. The underlying assumption is that fission is a slow process such that it does not disturb the phase-space (level density) equilibrium configuration. When a CN undergoes fission, the distortion to the phase-space at the saddle point is restored rapidly, such that equilibrium continues. Under this assumption, the decay of CN through fission or evaporation channels is calculated. The total decay width (Γ_T) can be written as,

$$\Gamma_T \;=\; \Gamma_f + \Gamma_n + \Gamma_p + \Gamma_\alpha + \Gamma_\gamma \tag{1.32}$$

where Γ_f is the fission width, Γ_n, Γ_p, Γ_α, and Γ_γ are the the particle emission widths for neutrons, protons, alpha particles and γ-rays respectively.

From the Equation 1.32, the probability of various decay channels can be calculated as,

$$P_f = \frac{\Gamma_f}{\Gamma_T};\; P_n = \frac{\Gamma_n}{\Gamma_T};\; P_p = \frac{\Gamma_p}{\Gamma_T} \tag{1.33}$$

The decay chain of the CN persists depending on the relative probabilities of various channels until:

1. The process is terminated by a fission event or,
2. The excitation energy of the CN drops below particle binding energy and ends up as evaporation residue.

To investigate the fission process, different classes of detector systems were used to detect the observables at different stages of the decay chain as shown in Figure 1.4. Measurement of fragment angular distribution, mass distribution, total kinetic energy distribution, etc. are some of the efficient methods used for the investigation. Until the 1980s, the existing data regarding the nuclear fission

process had been effectively described by the statistical models put forward by Weisskopf [11], Bohr and Wheeler [7], in addition to the contributions of Cohen and Swiatecki [17, 18]. These models were complemented by the shell correction proposed by Strutinsky [12] and Ignatyuk [14].

1.5 Challenges in heavy ion induced fission studies

A major confrontation with the statistical theory was observed when the experimental pre-scission neutron multiplicity (ν_{pre}) was compared with the theory [25]. It was found that the statistical theory underestimates the pre-scission neutron multiplicity, particularly at higher excitation energies. The observation of higher ν_{pre} than the statistical model prediction directly implies that fission occurs relatively slowly, which enhances the probability of neutron emission.

1.5.1 Need of dynamical calculations

The statistical model relies on the validity of phase-space equilibrium. However,at higher excitation energies where the fission rate is high, if the phase-space equilibrium at the saddle point is not restored, the overall Γ_f will be decreased. Experimental results affirm that the dynamical evolution of the di-nuclear system towards the saddle point is constrained by dissipative forces. The net effect of dissipation is the delay or hindrance in the shape evolution from nearly symmetric ground state to a highly deformed saddle point configuration. Consequently, a dynamical calculation incorporating appropriate forms of dissipative forces must be performed to describe the observables of fission induced by heavy ions at higher excitation energies. This forms the basis of the dynamical calculation.

The Langevin equation serves as a suitable dynamical equation to describe the fission process [26, 27]. It initiates with a compound nucleus (CN) in a nearly spherical shape and follows the trajectory of its evolution, termed the

Langevin trajectory, in small time intervals until scission occurs. Over the past two decades, numerous studies have been conducted based on both one-dimensional [26, 28] and multidimensional [27, 29, 30] Langevin equations to analyze experimental data concerning various aspects of fusion-fission reactions. However, these calculations demand substantial computational resources.

1.5.2 A semi-empirical approach : GEF model

In recent years, there has been a growing demand for theoretical codes with enhanced predictive capabilities and good consistency in correlating various fission observables. The General description of Fission observables (GEF) code [13] is a semi-empirical model developed to meet this need. GEF makes use of many theoretical concepts, primarily of a broad nature, avoids microscopic calculations with their approximations to minimize the high computational needs. Drawing from a substantial empirical data set, GEF constructs a comprehensive description of fission observables. The underlying theoretical framework, based on established concepts, defines the code in a qualitative way. About 100 parameters in the formalism are linked to the underlying physics, offering a quantitative specification of the model. These parameters were fine-tuned once using benchmark experimental data and remain the same across a wide range of excitation energies for all systems.

For the fission decay, GEF code begins with a compound nucleus characterized by a specific excitation energy and angular momentum (E^*, $< L >$) and then calculates the sequential decay of the system. Throughout the calculation, correlations between different quantities are maintained, and no parameter adjustments are required.

For the present thesis, which investigates fragment-neutron correlations in the fission of a lighter actinide nucleus within the excitation energy range of $\approx$ 30-60 MeV, GEF model calculations have been used extensively. While a comprehensive overview of fission process modelling in GEF is provided in [13, 31], the

following subsection emphasizes a key conceptual idea relevant to the present thesis.

Multi-chance fission

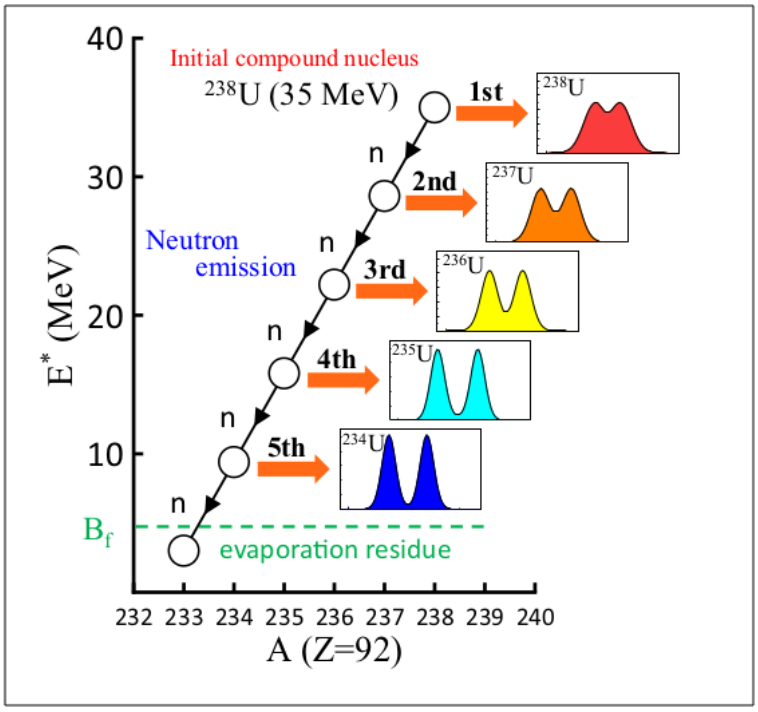

Figure 1.5: A conceptual view of multi-chance fission for the case of ^{238}U [32].

At high excitation energy and angular momentum, the decay pathway of a compound nucleus is largely determined by the competition between the particle emission width (Γ_i) and the fission width (Γ_f). Fission can occur directly from the parent nucleus (Z_{CN}, A_{CN}), termed first-chance fission, or from the daughter nuclei formed after particle emission(s). When the excitation energy (E^*) of a heavy nucleus is sufficiently high that the energy after particle emission(s) falls near or above the fission barrier of the daughter nuclei, the observed events may involve a sequence of fission-chances, such as first, second, third, and so forth. This phenomenon of sequential fission decay of a compound nucleus preceded by particle emission is called multi-chance fission. The GEF model accounts for multi-chance fission by evaluating the competition between Γ_i and Γ_f as a

function of excitation energy and angular momentum.

Figure 1.5 depicts a conceptual description of multi-chance fission. It shows the sequences of fission events of ^{238}U following neutron emission and the consequent changes in the mass distribution [32]. Notably, after each chance, the reduction in excitation energy opens up various fission modes that were less prominent in earlier chances. Multi-chance fission plays a central role in the emergence of different fission modes at medium excitation energies.

1.6 Motivation of the thesis

Over the decades of intense studies in the fission of actinide nuclei, there is a consensus that the fragment mass distribution is asymmetric at lower excitation energies. The macro-microscopic model described it as a manifestation of fragment shell effects [12]. With increase in nuclear excitation energy, the shape of mass distribution changes from asymmetric to symmetric Gaussian whose mean is around $A_{CN}/2$, where A_{CN} is the mass number of the compound nucleus. These macro-microscopic theories clubbed with phenomenological corrections [14] provide a vivid picture of spontaneous and induced fissions at lower ($<$ 30 MeV), medium (30 $<$ E $<$ 50 MeV) and higher ($>$ 50 MeV) excitation energies. A plethora of experimental data shows that, generally, the influence of fragment shells on mass distribution is prominent at lower E^*, diminishes for $E^* > 30$ MeV and becomes very small or negligible above $E^* \approx 40$ MeV, though the boundaries are not strictly defined in the theory.

Recent experimental results of mass distribution studies through multi-nucleon transfer (MNT) stand remarkably away from these expectations [33–35]. In their experiments, the multi-nucleon transfer method was employed to populate neutron-rich compound nuclei of elements such as Th, Pa, U, Np, Pu, Am, Cu and Bk at $E^* \approx 10$ - 70 MeV [33–35]. Surprisingly, even at very high $E^* \approx 60$ - 70 MeV, the mass spectra of these systems have shown shell influenced asymmetric fission. The mass spectra of some of the isotopes are depicted in Figure

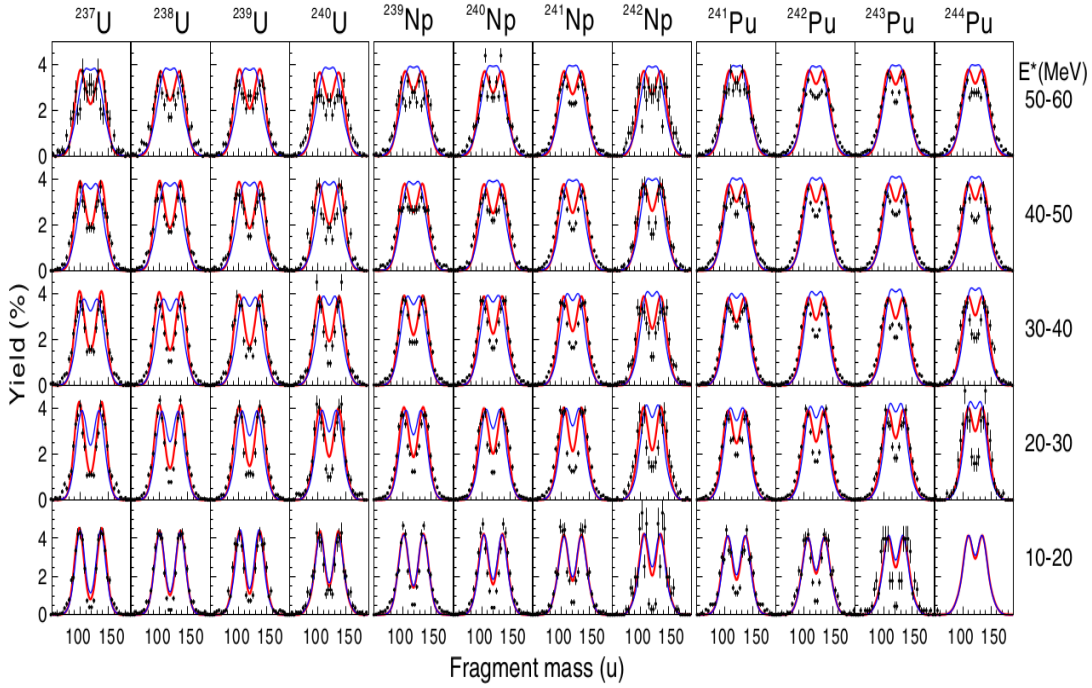

Figure 1.6: Mass distribution of fragments of the U, Np, and Pu isotopes at different excitation energies. Solid lines represent Langevin calculations with (red curves), and without (blue curves) the inclusion of multi-chance fission [33].

1.6. Multi-dimensional Langevin calculation that incorporates the multi-chance fission, could reproduce the distribution fairly well at all energies studied. It was concluded that the observed mass spectrum is brought about by sequential fission : fission followed by neutron emission. Depending on the particle emission width (Γ_n) in comparison to Γ_f, the compound nucleus may emit multiple neutrons and ends on lower E^* where shell effects are prominent. A series of experimental [33–35] and theoretical studies [32, 36] carried out on neutron-rich actinide nuclei emphasize the the necessity of considering multi-chance fission to describe the fragment mass distribution.

Unlike fission induced by MNT, the complete fusion of a heavy projectile with a target results in the formation of neutron-deficient CN in the actinide region. The probability of a higher chance fission is lower in such systems compared to CN formed via MNT. Therefore, an early washout of shell effects as a function of E^* can be expected in these nuclei. However, if the MCF, particularly the higher

chance fission contributes significantly at any given excitation energy, the fission modes may change. In such scenarios, the fission decay has to be analyzed by invoking the revival of microscopic effects to explain the experimental results. An example is the deformation-dependent quasi-fission reported in the reaction of ^{16}O+^{238}U around the Coulomb barrier energies [37]. The increase in mass width around and below barrier energies was attributed to quasi-fission induced by the high static deformation of the ^{238}U target. Below the capture barrier energies, the collision of the projectile with the tip of the deformed target can lead to the formation of a di-nuclear system that separates before full equilibration. This incomplete mass equilibration results in asymmetry in the fragment mass as observed at below barrier energies. Nevertheless, theoretical calculations that incorporate MCF also predict significant amount of asymmetric fission in this system due to shell effects [13]. This underscores the necessity of considering the effects of MCF for a comprehensive understanding of fission in the actinide region.

With this motivation, we conducted measurements of the mass distribution, $< \nu_{pre} >$, and the correlation between fragment mass and ν_{pre} ($Mass - \nu_{pre}$) in the fission of a lighter actinide nucleus, ^{227}Pa. This nucleus was formed through the complete fusion reaction of ^{19}F+^{208}Pb within the excitation energy range of $\approx$ 30 to 60 MeV. The interplay of various modes in fission observables and their changes with E^* can be deduced from the $Mass - \nu_{pre}$ correlation. Furthermore, since the excitation energy at the fission (E_{sp}) can be more accurately estimated by knowing the pre-saddle neutron multiplicity, measurements of $Mass - \nu_{pre}$ can provide valuable insights into the attenuation of shell effects in terms of E_{sp}.

Typically, prompt neutron multiplicity is extracted by analyzing the neutron energy spectra measured at various angles relative to the neutron sources. A major challenge in such investigations lies in efficiently detecting fast neutrons due to their nature of interactions within a medium. To detect fast neutrons in the energy range of interest, $\approx$ 100 keV to 10 MeV, a hydrogenous medium

is commonly employed, wherein fast neutrons undergo elastic scattering with protons. It is important to note that scattering-based detection techniques do not provide the full energy of the interacting neutron. The Time of flight (TOF) technique is one of the simplest and most widely used methods to determine the energy of fast neutrons. In this technique, the flight time of neutrons from the target to the detector is measured using a *START-STOP* detection system. The uncertainty in the measured energy, ΔE, depends on both the uncertainty in the path length (ΔL) and the intrinsic time resolution (ΔT) of the *START-STOP* setup. When employing large-volume neutron detectors to enhance efficiency, it is desirable to maintain a long flight path to minimize the contribution from $\frac{\Delta L}{L}$ to ΔE.

The measurement of fast neutrons with minimal energy uncertainty, finer angular steps, and high detection efficiency points to the necessity to develop a multi-detector array comprising organic based detectors with large flight path. Moreover, precise data on neutron emission in coincidence with other experimental observables can give a deeper insight into the physical aspects of compound nuclear evolution [25, 38, 39]. When a fused system undergoes binary fission, the emitted particles carry valuable sources of information about the dynamics of the process. Neutrons, being charge-less, do not experience any Coulomb force. Consequently, the emission probabilities are orders of magnitude larger than those of light-charged particles like protons and alpha particles. Neutron studies are therefore among the most sensitive and effective ways to probe nuclear reaction dynamics. Neutron multiplicity measurements provide important data regarding nuclear temperature, viscosity of nuclear matter, signatures of quasi-fission processes, and more. With these motivations, a large array of neutron detectors, of type BC501A, has been developed and installed in one of the beam lines of IUAC accelerator facility. Extensive Monte Carlo calculations have been conducted to ensure the optimal utilization of this detector setup. Key parameters characterizing the facility, including the scintillation response of BC501A,

intrinsic efficiency, cross-talk probability, and loss of neutron flux due to scattering, were simulated and compared with measurements using the FLUKA Monte Carlo code [40, 41].

1.7 Outline of the thesis

The present thesis encompasses two distinct domains in the field of nuclear research : nuclear instrumentation, and heavy ion induced fission to study the impact of neutron emission in the fission of actinide nuclei. The initial two chapters are dedicated for a detailed description of nuclear instrumentation, the art and science about making scientific instruments. Subsequent chapters detail the experimental techniques employed for measuring various observables, conducting data analysis, and presenting the salient results obtained. A comprehensive discussion is also included to interpret the results, taking into account theoretical considerations. The following paragraphs highlight a formal description of the thesis organization.

Chapter 2 of the thesis is dedicated to the developmental aspects of the National Array of Neutron Detectors facility. The mechanical structure of the array and scattering chamber facility, salient features of the neutron detectors, design and development of fission detectors, analog signal processing electronics for fission and neutron detectors and the data acquisition system are described in great detail. Important results of the performance evaluation such as $n - \gamma$ discrimination, time resolution, cross-talk probability, secondary radiation suppression, etc. are given based on the offline tests and commissioning tests by in-beam experiments.

FLUKA based Monte Carlo calculations to estimate some of the important features of the detectors and array are discussed in **Chapter 3**. A novel technique to determine the intrinsic efficiency of the BC501A detector and its comparison with the FLUKA calculation are described. The light output response of BC501A detectors for mono-energetic neutrons and γ-rays was investigated

through FLUKA calculation and measurements. Large-scale FLUKA calculations to estimate the loss of neutrons due to scattering, accurate determination of array efficiency, etc. are also incorporated in this chapter.

Experimental aspects of mass distribution and neutron multiplicity (ν_{pre}) measurements are detailed in **Chapter 4**. A description of the Pelletron accelerator facility at Inter-University Accelerator Centre, facilities used fission fragments and neutrons detection, analog signal processing electronics, and data acquisition system are provided in this chapter.

Chapter 5 describes the data analysis methods adopted for deriving the important experimental observables. The details of various methods applied to extract the mass and kinetic energy distribution of fission fragments, average neutron multiplicity, and the correlation of fragment mass with pre-scission neutrons are provided in this chapter.

The results of different measurements such as fragment mass and kinetic energy distribution, ν_{pre}, and $Mass - \nu_{pre}$ are presented in **Chapter 6**. A semi-empirical code, GEF is used for the interpretation of the experimental distribution and their correlations. In-depth discussion on the role of various fission modes in the experimental observables and their changes with excitation energies is also included in this chapter.

A summary of the work done, conclusion, and a future outlook of this investigation are presented in **Chapter 7**.

Bibliography

[1] O. Hahn and F. Stassmann, Naturwissenschaften **27**, 11 (1939).

[2] G. Gamow, Nature **122**, 805 (1928), https://doi.org/10.1038/122805b0.

[3] J. M. Pearson, Physics Today **68**, 40 (2015), https://doi.org/10.1063/PT.3.2817.

[4] L. Meitner and O. Frisch, Nature **143**, 239 (1939), https://doi.org/10.1038/143239a0.

[5] L. Meitner and O. Frisch, Nature **143**, 471 (1939), https://doi.org/10.1038/143471a0.

[6] O. Frisch, Nature **143**, 276 (1939), https://doi.org/10.1038/143276a0.

[7] N. Bohr and J. A. Wheeler, Phys. Rev. **56**, 426 (1939), https://link.aps.org/doi/10.1103/PhysRev.56.426.

[8] G. Gamow, Proceedings of the Royal Society of London Series A **126**, 632 (1930), 10.1098/rspa.1930.0032.

[9] A. Bohr and B. R. Mottelson, Nuclear structure Vol. I(Benjamin Press, New York, 1969) .

[10] V. Strutinsky, Physics Letters B **47**, 121 (1973), https://doi.org/10.1016/0370-2693(73)90585-6.

[11] V. Weisskopf, Phys. Rev. **52**, 295 (1937), https://link.aps.org/doi/10.1103/PhysRev.52.295.

[12] V. Strutinsky, Nuclear Physics A **95**, 420 (1967), https://doi.org/10.1016/0375-9474(67)90510-6.

[13] K.-H. Schmidt, B. Jurado, C. Amouroux, and C. Schmitt, Nuclear Data Sheets **131**, 107 (2016), special Issue on Nuclear Reaction Data, https://doi.org/10.1016/j.nds.2015.12.009.

[14] A. V. Ignatyuk, G. N. Smirenkin, and A. S. Tishin, Yad. Fiz. **21**, 485 (1975), https://www.osti.gov/biblio/4175339.

[15] P. C. Rout, D. R. Chakrabarty, V. M. Datar, S. Kumar, E. T. Mirgule, A. Mitra, V. Nanal, S. P. Behera, and V. Singh, Phys. Rev. Lett. **110**, 062501 (2013), https://link.aps.org/doi/10.1103/PhysRevLett.110.062501.

[16] S. Cohen, F. Plasil, and W. Swiatecki, Annals of Physics **82**, 557 (1974), https://doi.org/10.1016/0003-4916(74)90126-2.

[17] S. Cohen and W. Swiatecki, Annals of Physics **19**, 67 (1962), https://doi.org/10.1016/0003-4916(62)90234-8.

[18] S. Cohen and W. Swiatecki, Annals of Physics **22**, 406 (1963).

[19] F. Plasil, Pramana **33**, 145 (1989), https://www.ias.ac.in/article/fulltext/pram/033/01/0145-0159.

[20] M. Beckerman and M. Blann, Phys. Rev. C **17**, 1615 (1978), https://link.aps.org/doi/10.1103/PhysRevC.17.1615.

[21] F. Plasil, R. L. Ferguson, R. L. Hahn, F. E. Obenshain, F. Pleasonton, and G. R. Young, Phys. Rev. Lett. **45**, 333 (1980), https://link.aps.org/doi/10.1103/PhysRevLett.45.333.

[22] M. G. Mustafa, P. A. Baisden, and H. Chandra, Phys. Rev. C **25**, 2524 (1982), https://link.aps.org/doi/10.1103/PhysRevC.25.2524.

[23] A. J. Sierk, Phys. Rev. C **33**, 2039 (1986), https://link.aps.org/doi/10.1103/PhysRevC.33.2039.

[24] F. Plasil, T. C. Awes, B. Cheynis, D. Drain, R. L. Ferguson, F. E. Obenshain, A. J. Sierk, S. G. Steadman, and G. R. Young, Phys. Rev. C **29**, 1145 (1984), https://link.aps.org/doi/10.1103/PhysRevC.29.1145.

[25] D. Hinde, R. Charity, G. Foote, J. Leigh, J. Newton, S. Ogaza, and A. Chattejee, Nuclear Physics A **452**, 550 (1986), https://doi.org/10.1016/0375-9474(86)90214-9.

[26] W. Ye, F. Wu, and H. Yang, Physics Letters B **647**, 118 (2007), https://doi.org/10.1016/j.physletb.2007.01.065.

[27] A. V. Karpov, P. N. Nadtochy, D. V. Vanin, and G. D. Adeev, Phys. Rev. C **63**, 054610 (2001), https://link.aps.org/doi/10.1103/PhysRevC.63.054610.

[28] G. Chaudhuri and S. Pal, Phys. Rev. C **65**, 054612 (2002), https://link.aps.org/doi/10.1103/PhysRevC.65.054612.

[29] J. Sadhukhan and S. Pal, Phys. Rev. C **84**, 044610 (2011), https://link.aps.org/doi/10.1103/PhysRevC.84.044610.

[30] P. Nadtochy, E. Vardaci, A. Di Nitto, A. Brondi, G. La Rana, R. Moro, M. Cinausero, G. Prete, N. Gelli, and F. Lucarelli, Physics Letters B **685**, 258 (2010), https://doi.org/10.1016/j.physletb.2010.01.069.

[31] K.-H. Schmidt and B. Jurado, Reports on Progress in Physics **81**, 106301 (2018), https://dx.doi.org/10.1088/1361-6633/aacfa7.

[32] S. Tanaka, Y. Aritomo, Y. Miyamoto, K. Hirose, and K. Nishio, Phys. Rev. C **100**, 064605 (2019), https://link.aps.org/doi/10.1103/PhysRevC.100.064605.

[33] K. Hirose, K. Nishio, S. Tanaka, R. Léguillon, H. Makii, I. Nishinaka, R. Orlandi, K. Tsukada, J. Smallcombe, M. J. Vermeulen, S. Chiba, Y. Aritomo, T. Ohtsuki, K. Nakano, S. Araki, Y. Watanabe, R. Tatsuzawa, N. Takaki,

N. Tamura, S. Goto, I. Tsekhanovich, and A. N. Andreyev, Phys. Rev. Lett. **119**, 222501 (2017), https://link.aps.org/doi/10.1103/PhysRevLett.119.222501.

[34] R. Léguillon, K. Nishio, K. Hirose, H. Makii, I. Nishinaka, R. Orlandi, K. Tsukada, J. Smallcombe, S. Chiba, Y. Aritomo, T. Ohtsuki, R. Tatsuzawa, N. Takaki, N. Tamura, S. Goto, I. Tsekhanovich, C. Petrache, and A. Andreyev, Physics Letters B **761**, 125 (2016), https://doi.org/10.1016/j.physletb.2016.08.010.

[35] M. J. Vermeulen, K. Nishio, K. Hirose, K. R. Kean, H. Makii, R. Orlandi, K. Tsukada, I. Tsekhanovich, A. N. Andreyev, S. Ishizaki, M. Okubayashi, S. Tanaka, and Y. Aritomo, Phys. Rev. C **102**, 054610 (2020), https://link.aps.org/doi/10.1103/PhysRevC.102.054610.

[36] A. C. Berriman, D. J. Hinde, D. Y. Jeung, M. Dasgupta, H. Haba, T. Tanaka, K. Banerjee, T. Banerjee, L. T. Bezzina, J. Buete, K. J. Cook, S. Parker-Steele, C. Sengupta, C. Simenel, E. C. Simpson, M. A. Stoyer, B. M. A. Swinton-Bland, and E. Williams, Phys. Rev. C **105**, 064614 (2022), https://link.aps.org/doi/10.1103/PhysRevC.105.064614.

[37] K. Banerjee, T. K. Ghosh, S. Bhattacharya, C. Bhattacharya, S. Kundu, T. K. Rana, G. Mukherjee, J. K. Meena, J. Sadhukhan, S. Pal, P. Bhattacharya, K. S. Golda, P. Sugathan, and R. P. Singh, Phys. Rev. C **83**, 024605 (2011), https://link.aps.org/doi/10.1103/PhysRevC.83.024605.

[38] D. Hilscher and H. Rossner, Ann. Phys. Fr. **17**, 471 (1992), https://doi.org/10.1051/anphys:01992001706047100.

[39] D. J. Hinde, D. Hilscher, H. Rossner, B. Gebauer, M. Lehmann, and M. Wilpert, Phys. Rev. C **45**, 1229 (1992), https://link.aps.org/doi/10.1103/PhysRevC.45.1229.

[40] T. T. Böhlen, F. Cerutti, M. P. W. Chin, A. Fasso‘, A. Ferrari, P. G. Ortega, A. Mairani, P. R. Sala, G. Smirnov, and V. Vlachoudis, Nucl. Data Sheets **120**, 211 (2014).

[41] A. Ferrari, P. R. Sala, A. Fasso‘, and J. Ranft, CERN-2005-10(2005), INFN/TC_05/11, SLAC – R – 773 (2005).

Chapter 2

Development of a multi-neutron detector facility and its performance evaluation

2.1 Importance of neutron measurements

The study of heavy ion collision experiments at energies around the Coulomb barrier throws light on the mechanisms of a variety of nuclear processes like deep in-elastic collision, fusion, equilibrated fission, non-compound fission, etc. These investigations provide deeper insight into the viscosity of nuclear matter, the time scale of fusion-fission, the importance of shell effects to understand the reaction mechanism, etc. Experimentally, nuclear fission and related phenomena have been studied using large area fragment detectors. The detection system provides sensitive information such as the mass distribution of the fragments, the angular distribution, and the correlation between fragment mass and emission angles [1].

Precise data on neutron emission in coincidence with other experimental observables can give a deeper insight into the physical aspects of compound nuclear evolution [2–5]. When a fused system evolves to binary fission, light particles are emitted that are valuable sources of information on the dynamics of the

process. Neutrons, being chargeless, do not experience any Coulomb forces. Because of this, the emission probabilities are orders of magnitude larger than those of light-charged particles like protons, alpha particles, etc. Neutron studies are therefore among the most sensitive and effective ways to probe nuclear reaction dynamics. Neutron multiplicity, the number of neutrons emitted per fission, measurements can provide important data regarding nuclear temperature, nuclear dissipation, quasi-fission processes, etc. To determine the neutron multiplicity, precise knowledge of the angular distribution and kinetic energy of neutrons is essential. Recent findings from the DeMON array point to a novel method for fusion-fission dynamics research [6]. The array has been utilized to find the multiplicity distribution rather than only measuring the average neutron multiplicity. With the help of backtracking algorithm, a two-dimensional correlation between pre-scission and post-scission multiplicities has been extracted from the multiplicity distribution.

To sum up, a multi-neutron detector array that can measure neutron kinetic energy with good resolution, angular distribution with smaller angular steps, and higher fold efficiency to find multiplicity distribution will be a potential tool in the investigation of various aspects of heavy ion collisions around the Coulomb barrier energies. The following sections describe the developmental aspects and characterization of the neutron detector array at IUAC.

2.2 Multi-neutron detector facility at IUAC

The National Array of Neutron Detectors (NAND) is a multi-neutron detector facility that accommodates various sub-systems for the study of heavy ion induced fission and related phenomena. The facility consists of a fixed radius hemi-spherical dome structure to mount organic liquid scintillators for fast neutron detection. To mount the liquid cells, a mechanical structure has been built using metal tubes linked to form a geodesic dome around the target. The dome is made of 20 mm diameter and 4 mm thick mild steel tubes linked together,

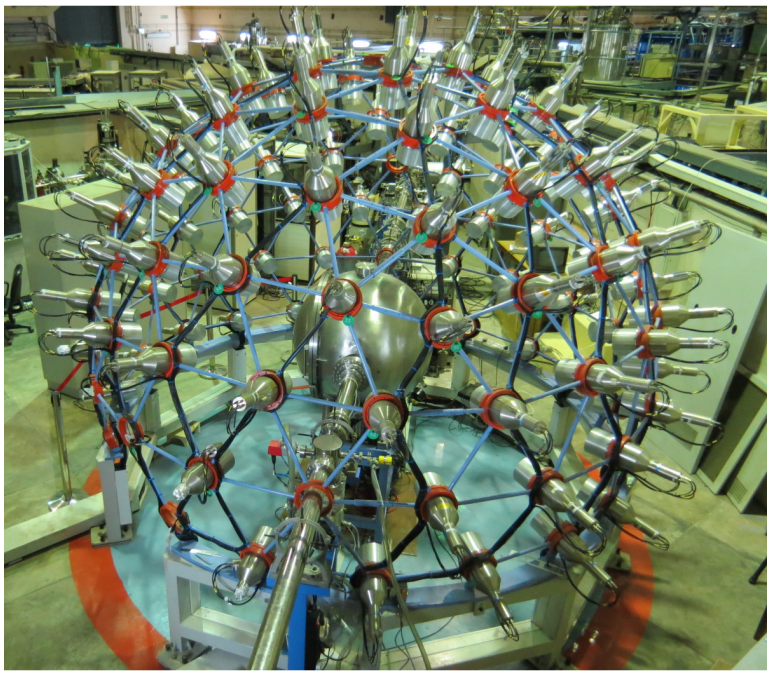

Figure 2.1: A photograph of the National Array of Neutron Detectors facility.

minimizing the amount of material surrounding the detectors. The liquid cells, along with photo-multiplier tubes and bases, are fixed to the dome structure by means of circular hubs made of rings connected to the vertices of the dome. The dome structure is truncated in the lower hemisphere with a ground clearance of 90 cm from the floor. The structure has eight independent horizontal rings. These horizontal planes are separated by an inter-planar angle of 15° with respect to the centre. The neutron detectors are mounted with an inter-cell separation of ≈ 55 cm on different horizontal rings. A flight path of 175 cm between detectors and the target was chosen to achieve an acceptable level of cross-talk while maintaining reasonable solid angle coverage. The solid angle subtended by an individual neutron cell is ≈ 4 mSr and the whole array covers ≈ 3.3 % of 4π.

At the centre of the dome structure, a 50 cm radius spherical vacuum chamber is mounted on the beam line to house the targets and charged particle detectors. The chamber, constructed from 4 mm thick stainless steel, contains a sector plate and four manually rotatable arms for placing charged particle detectors. The angular and radial positions can be adjusted within 1° and 1 mm accuracy.

A circular ring fixed at the beam exit port inside the chamber is used to mount silicon detectors at a distance of 42 cm from the target and at an angle of $\approx 12^{\circ}$ w.r.t. the beam direction. These detectors are used for beam monitoring and normalization purposes. A target ladder mounted vertically at the centre of the chamber can hold five independent targets that can be rotated and moved up or down using a linear and rotary magnetic manipulator. For a typical application of heavy-ion fission study, the chamber usually houses a pair of multi-wire proportional counters to detect the fission fragments. The chamber and the beam lines are evacuated by a set of turbo-molecular pumps to a typical operating pressure of $2{\times}10^{-6}$ mbar. The whole assembly of the neutron array and the reaction chamber are installed in beam hall-II of IUAC [7].

For the ease of tuning heavy beams from Linear Accelerator (LINAC)[8], a cylindrical diagnostic chamber is installed ≈ 285 cm upstream from the reaction chamber. It contains fully and partially depleted silicon surface barrier detectors mounted at an angle of 20° with respect to the beam for timing and energy measurements. The beam scattered from 200 μg/cm^2 thick gold foil is detected using these silicon detectors, which are utilized for optimizing the tuning of the LINAC beam. A picture of the NAND detector array installed in the beam hall is shown in Figure 2.1. In the following sections, various sub-systems of the NAND facility are described.

2.3 Nuclear radiation detectors

2.3.1 Neutron detectors : BC501A

Organic liquid scintillators have been extensively used for fast neutron detection due to their excellent timing characteristics, high counting efficiency, and particle dependent pulse shape. Inside the detector volume, the interaction of neutrons and γ rays produces recoil-charged particles that cause excitation or ionization of the scintillation medium. The excited molecules de-excite by emitting light

with a fast (few ns) and slow decay component (few hundred ns) [9, 10]. The relative intensity of fast and slow decay components, and hence the shape of the resultant pulse, depends on the type of particles causing excitation [11]. A pictorial representation of light pulse from an organic liquid scintillator is shown in the Figure 2.2. Though the scintillation pulses show nearly the same rise time for neutron and γ-ray interactions, the neutron pulses exhibit a large decay time compared to the other signal. This feature is utilized to discriminate between the neutrons and γ-rays emitted from heavy ion collision experiments.

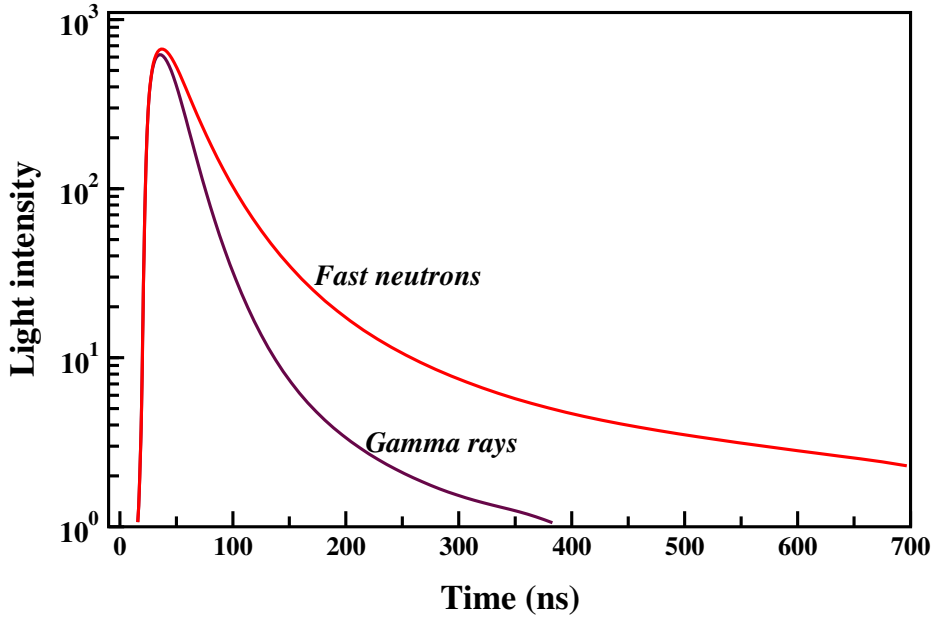

Figure 2.2: Pictorial representation of scintillation pulses from an organic liquid scintillator [10].

The NAND facility consists of 100 liquid scintillators. Each detector contains organic liquid scintillator BC501A (Bicron-MAB BC501AL) in a cylindrical cell, 12.7 cm in diameter and 12.7 cm long, coupled to 5" diameter photo-multiplier tube (PMT, Hamamatsu R4144). The PMT has 8 dynodes and a cylindrical μ-metal to shield the tube from stray magnetic fields. A voltage divider base with an in-built pre-amplifier is attached to the PMT to feed the high voltage bias and readout of the signal. The detectors are positioned to cover wide ranges of polar and azimuth angles at a fixed distance of 175 cm from the target.

2.3.2 Fission fragment detectors : MWPC

Fragment mass distribution is derived from the simultaneous measurement of fragment velocities, which is described in detail in Chapter 5. The detector system chosen for such investigations should provide clear separation between fragments and other charged particle fluxes. Gas based detector systems are one of the easiest choices, as they are cost effective and easy to construct in different sizes and shapes. Two large area (20×10 cm^2) multi-wire proportional counters (MWPC) have been developed in order to detect the complementary fission fragments and to facilitate the following measurements of their mass and mass-angle correlation [12, 13]. These detectors provide information on the two-dimensional position (X and Y), and timing of interacting particles, which are used for the kinematic reconstruction of a nuclear fission event.

2.3.3 Design and development of MWPC detectors

Figure 2.3 schematically shows the structure of MWPC. The core of MWPC is designed in three electrode geometry. The central electrode is developed from 2 μm thick Mylar (polyethylene teraphthalate) coated with aluminium on both sides. The foil was stretched without wrinkles on a 2 mm thick printed circuit board (PCB) from which the time signal was extracted. Two position frames were mounted on either side of the central electrode, with an inter-electrode separation of 3.2 mm. The X position frame was fabricated using gold-plated tungsten wires of thickness 20 μm soldered on a 3.2 mm thick PCB. It consists of 160 wires, in which two adjacent wires are grouped together and connected to a tapped delay line for position information. The Y plane consists of gold-plated copper strips printed on a PCB frame whose width and separation are $\approx$1 mm and 0.25 mm respectively. As in the case of the X frame, two adjacent strips were grouped and connected to a tapped delay line for extracting the Y-position.

The delay line method was used to get the position information. The grouped wires or strips were connected to a multi-tapped delay chip. The time difference

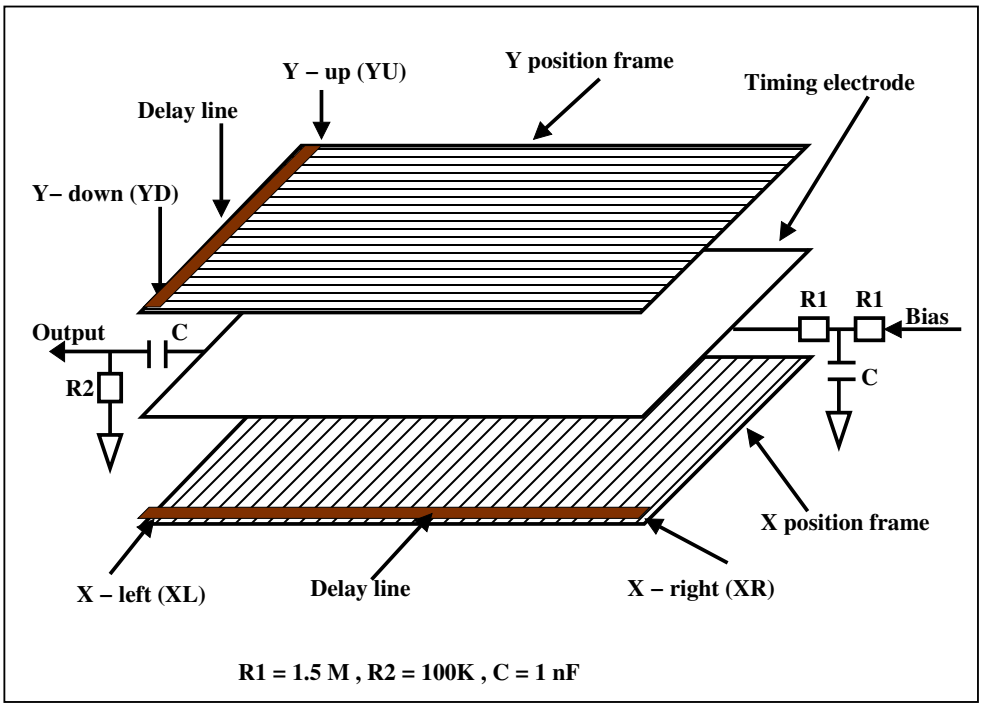

Figure 2.3: A schematic of the electrode configuration of MWPC detectors.

between the signals at two ends of the position frame was used to determine the position of the interaction. Commercially known passive delay chips supplied by *Rhombus Industries Inc.*, model *TZB 12-5*, were used in these detectors. Model *TZB 12-5* chips offer a 2 ns tap-to-tap delay and characteristic impedance of 50 Ω. Eight of these chips were utilized in the X frame and four in the Y frame. Each chip contains ten taps. This results in an end-to-end delay of 160 ns in the X frame and 80 ns in the Y frame. Both ends of delay lines in X and Y frames were kept at ground potential through 100K resistors. The performance of the delay lines in both X and Y electrodes was tested using a pulsar signal. Every tap on the delay chip was connected to a pulsar signal, and the time delay in the signal at the other end was recorded. Figure 2.4 shows the test result of X-position electrode. 80 distinct peaks have been observed that correspond to 160 ns end-to-end delay in the X frame. All 24 chips were tested to verify their functionality before being assembled to form the detectors.

The timing information was extracted from the central foil-based electrode,

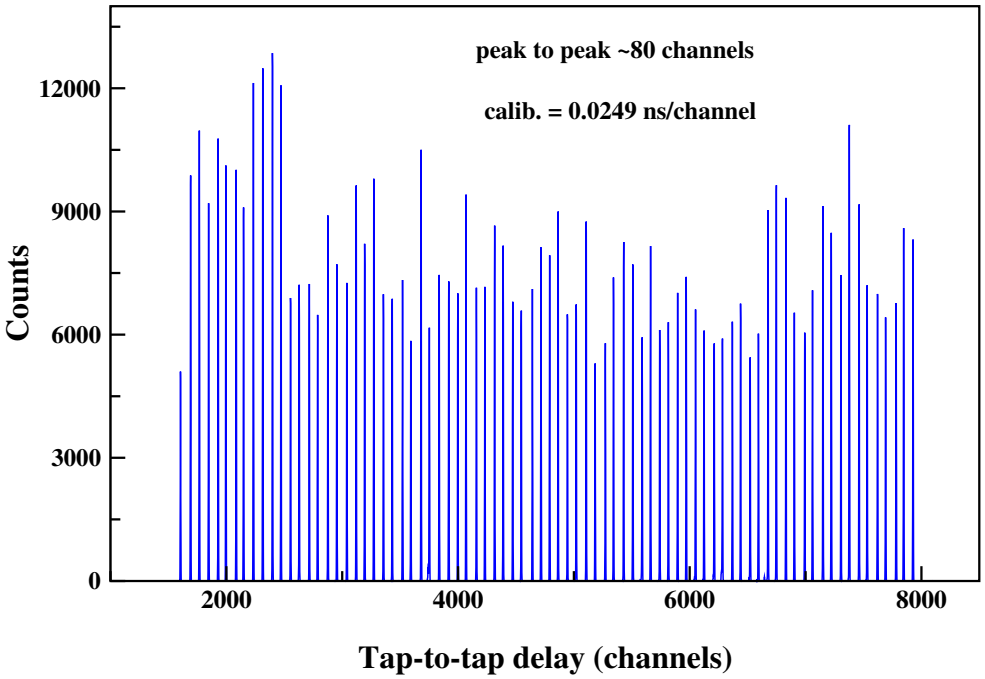

Figure 2.4: Test results of *Rhombus delay chips* used for finding the position information in X and Y direction. Each peak corresponds to a pulsed signal received at the delay tap. Tap-to-tap delay is expected to be $\approx$ 2 ns. Eighty peaks have been observed in X electrode where the end-to-end delay is expected to be $\approx$ 160 ns.

where avalanche multiplication takes place. The timing electrode was biased to a negative high voltage through a high resistor ($\approx$ 1.5 MΩ). A 1 nF capacitor was used to ground the ripples in the dc bias supply. After avalanche multiplication, the movement of electrons away from the electrode or positive ions towards it induces positive charges. To process the induced signals, an inverting fast preamplifier was mounted near the detector inside the vacuum chamber. The X and Y electrodes were assembled in a mutually perpendicular configuration on either side of the central electrode. The entire electrode assembly is mounted inside a rectangular aluminium box, and it was isolated from the target chamber with the help of a thin window foil developed from a plane Mylar of thickness $\approx$1 μm. Figure 2.5 shows a photograph of an MWPC detector after assembling the position and timing electrodes.

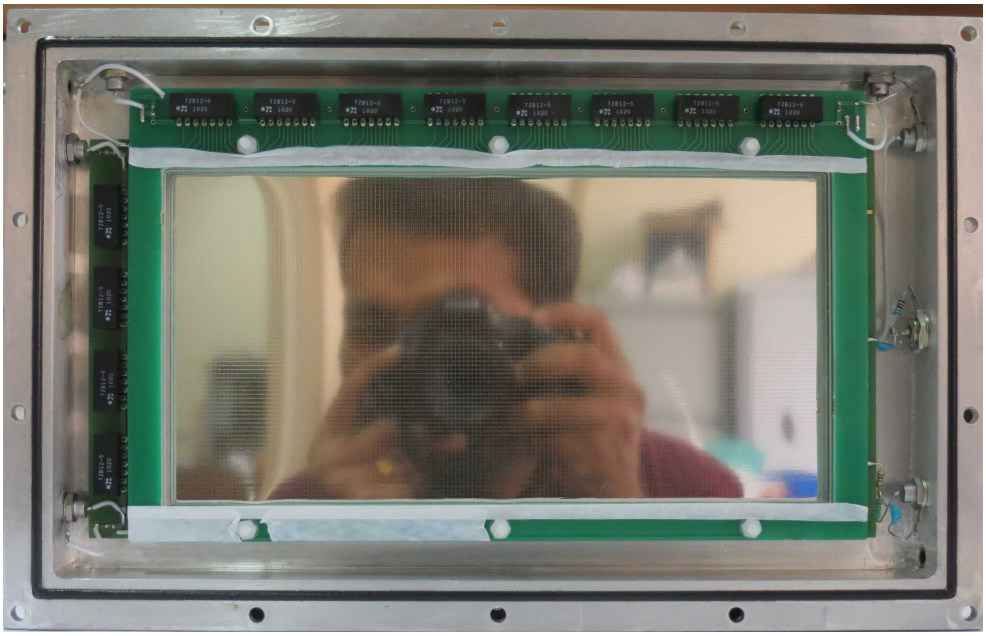

Figure 2.5: Photograph of an MWPC detector after assembling the electrodes. Mutually orthogonal position electrodes (X & Y), connected with delay chips, can be observed. Aluminised Mylar foil was developed in mirror finish to avoid any non-uniformity of electric field.

2.4 Electronics

2.4.1 Pulse shape discrimination (PSD) module

BC501A detector is one of the best fast neutron detectors available due to its good timing and pulse shape discrimination properties. The digital charge comparison technique and the zero-cross over time (Z/C) method are the most widely used electronic methods for particle identification, which make use of pulse shape discrimination [14–16]. Though the charge comparison method appears to be the most simple and straightforward technique for $n-\gamma$ discrimination [15], Wolski *et al.* compared the performances of charge comparison and the Z/C technique and found the Z/C technique superior to charge comparison for a wide dynamic range of neutron energies [14]. A discrimination approach with a wide dynamic range for neutron energies is desired because the heavy-ion reaction creates neutrons with energy typically ranging from a few 100 KeV to $\approx$ 20 MeV. Therefore, we have adopted the electronic Z/C technique for discriminating the neutrons and

gamma rays interacting in the BC501A detector.

A custom-built PSD module based on the Z/C method is used for $n-\gamma$ separation. Ref. [17] provides a summary of the key features of this electronics module. It is a single width NIM module with two independent channels that can accept signals from two neutron detectors. The module has integrated electronics for pulse shaping, amplification,constant fraction discrimination (CFD), Z/C detection, and time to amplitude converter (TAC). Each channel accepts the anode and dynode signals of PMT as inputs and provides processed outputs for total light-output, prompt and delayed timing CFDs and TAC for pulse shape discrimination. Fifty such modules have been fabricated and installed in the facility. The $n-\gamma$ discrimination and its figure of merit (FOM) using this module are described in the later sections.

2.4.2 Fast-timing pre-amplifiers

The position and timing signals from the MWPC were amplified by custom built fast timing pre-amplifiers [18]. The pre-amplifier circuit is based on the design given by Stelzer [19] and fabricated using high frequency bipolar junction transistors. The design utilizes three/four inverting stages realized by common emitter amplifier (BFR92) with an emitter follower at the output stage (BFT92). The number of inverting stages is decided by the polarity of charge induced at the respective electrode. These separate stages are cascaded to achieve the desired gain factor of 100. The internal rise time of the pre-amplifier signal is $\approx$ 2 ns with an input impedance of 50 Ω. Since the power requirement is low ($\approx$ 200 mW/ unit), the pre-amplifiers are compatible for in-vacuum operations. Five such units (four positions and one timing pre-amplifiers) were assembled in an aluminum box and mounted next to each MWPC.

2.4.3 High voltage supplies for PMTs of BC501A

To obtain the necessary gain for the anode signal, all neutron detectors are typically operated at high voltages up to -2000V. Each detector has a base with a suitable voltage divider network attached to it that is used to apply voltages to the photo-multiplier tubes. A custom-built charge-sensitive pre-amplifier circuit for the dynode signal is also included in the base. The detectors are biased independently using a multi-channel high voltage supply. Both commercially available multi-channel high voltage supplies as well as custom-made supplies were used to bias 100 detectors. Compact crate-less programmable power supplies were built using array of low voltage to high voltage DC-DC converter chips generating -2000V. The chip is mounted on a control board with an embedded server. The control board contains a *TCP/IP* stack implemented using a microprocessor (ATMEGA 168/328), an *SPI* driven Ethernet controller (ENCJ60) and a 12-bit digital to analog converter (AD7541). Each board is identified with a unique *MAC* and *IP* address and is part of a local area network. To communicate with the power supply unit, *LabVIEW* based graphic user interface (GUI) has been developed, which enables the *read and write* operations. A total of 24 units are assembled in a single $2U$ size box (19 inch rack mount) and 3 such boxes are fabricated, tested, and installed in the array. The remaining detectors are biased by a commercial programmable multi-channel high voltage system (*Wiener- MPOD*).

2.5 Data acquisition system

The acquisition system used to collect data from NAND array is a *VME* based analog data acquisition system employing modern high-density analog to digital converters (ADC) and time to digital converters (TDC) from CAEN [20]. The acquisition trigger, generated from radiation detectors, is inhibited by the $BUSY$ signal from all VME modules in the data acquisition. $BUSY$ blocking was

applied to the acquisition trigger via NIM electronics. The *trigger* would be released only when (i) VME modules are not *BUSY* and (ii) signal from any of the fission detectors is present in coincidence with the RF of the beam pulse.

For experiments involving full detectors in the array, there are ≈ 320 parameters to be read. A total of seven ADC (v785) and four TDC (v775) are used for acquiring data from neutron and other charged particle detectors. A single crate data acquisition system is implemented using a commercial controller (*v2718*). A VME version of multi-parameter acquisition software LAMPS [21], compatible with ROOT data format, has been used for online data acquisition. The data acquisition dead time was found to be ≈ 20 % for 352 parameters when the event rate was ≈ 5000. Recently, a VME crate controller that facilitates both trigger generation and BUSY blocking has been developed indigenously [22]. The list-mode data is recorded in ROOT format using a data acquisition software *NiasMARS* in conjunction with the crate controller [23].

2.6 Performance evaluation of BC501A detectors

The characteristics of the neutron detectors and associated electronics are optimized for the best performance, with a prime focus on neutron detection from low-energy heavy-ion induced fusion-fission reactions. Also, a large γ-ray background is often expected from these reactions, and efficient $n-\gamma$ discrimination is crucial for TOF. In order to yield the best timing performance, the detectors are operated with PMT voltage biased to yield anode signal strengths of typical amplitudes ≈450 - 500 mV for 662 KeV γ-rays from ^{137}Cs radioactive source. Generally, the value of bias voltage changes from detector to detector because of the differences in the light yield and the gain of the photo-multiplier tubes. The bias voltage applied here varies from -1400V to -1800V for the hundred neutron detectors in the array. For each detector, the detection threshold energy was set sufficiently low ≈0.5 MeV below which the $n-\gamma$ discrimination becomes poor. The following subsections discuss the performance characteristics of BC501A for

energy linearity, $n - \gamma$ discrimination, and time resolution.

2.6.1 Energy linearity

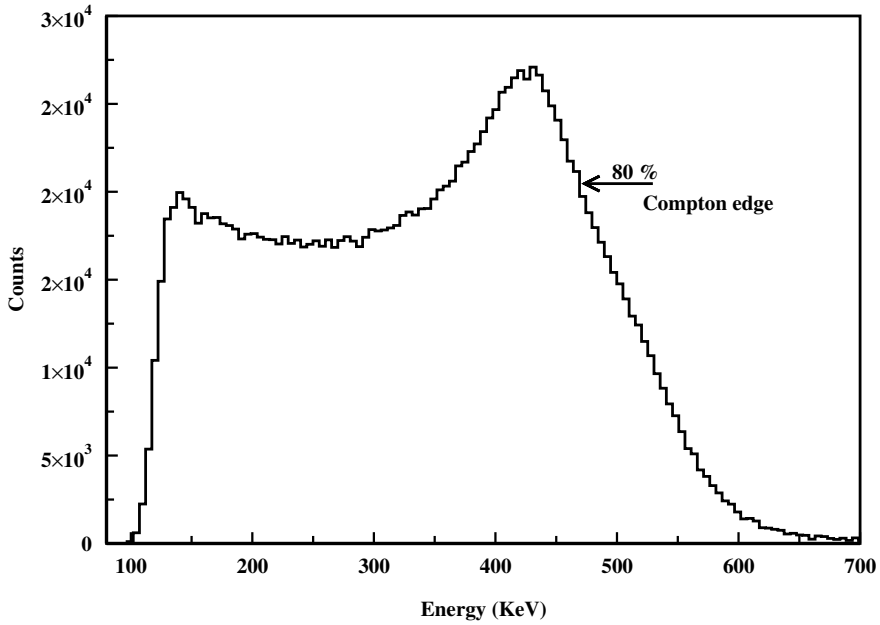

Figure 2.6: Light output spectrum of monoenergetic γ-rays from ^{137}Cs. The spectrum is used for energy calibration based on the Compton edge which is marked in the figure.

Gamma ray interaction in the detector medium is mainly via Compton scattering, giving recoil electrons with a continuum of energy depending upon the angle of Compton scattering. Due to the finite resolution in light output (ΔL) to a given energy loss in the detector cell, and due to multiple scattering in the detector volume caused by the larger size of the detector, the light output spectrum from the neutron detector does not show a sharp discontinuity, a characteristic of the Compton edge. Rather, the peak diminishes slowly with energy. For large volume detectors, Naqvi *et al.* have shown that the position of the Compton edge is lower than the half height of the Compton maxima [24]. For energy calibration, we have considered the Compton edge, which corresponds to 80 % of the maximum height. Figure 2.6 displays a typical light output spectrum from the interaction of mono energetic γ-rays from ^{137}Cs source. The arrow indicates

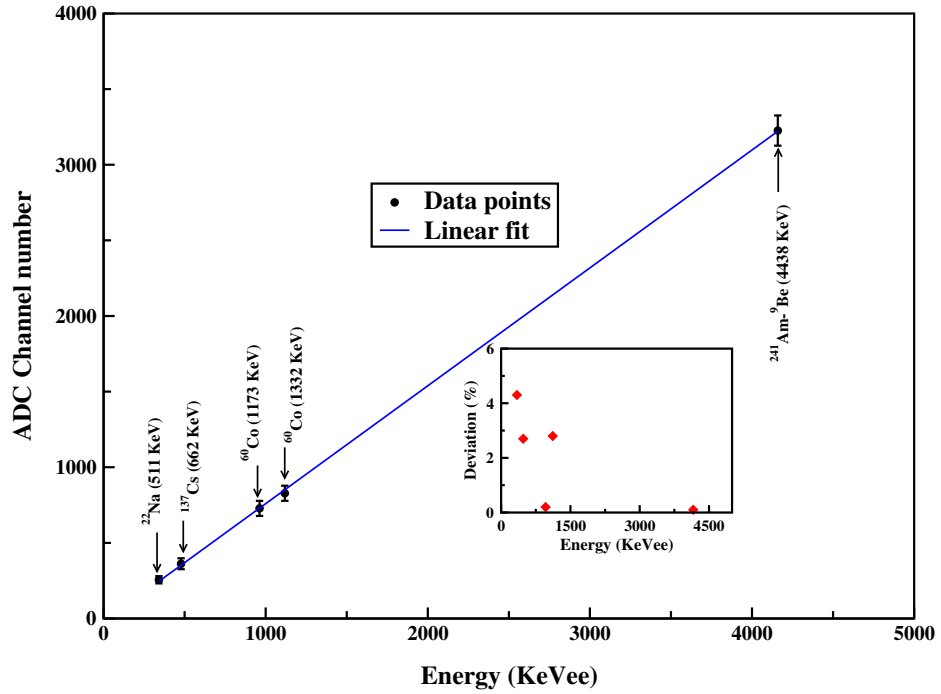

Figure 2.7: The response linearity of BC501A detectors for recoil electron energy ranging from ≈ 0.3 MeV to 4.15 MeV. The vertical error bars indicate the uncertainty in marking the Compton edge for γ-rays from different radioactive sources. The inset shows the percentage deviation of data from the fit.

the Compton edge for 662 KeV energy γ-ray.

In order to verify the linearity of the pulse heights, the Compton edge positions for several γ-rays from radioactive sources were determined. Sources like ^{137}Cs and ^{22}Na were used for calibrating the light output spectrum and with a given calibration, the light output spectra were recorded for higher energy γ rays from ^{60}Co and ^{241}Am-^{9}Be sources. In Figure 2.7 the pulse heights from a single detector for recoil electron energies ranging from 341 keVee to 4.15 MeVee is shown. A linear fit to the data points was applied. The vertical error bars correspond to the statistical uncertainty in marking the Compton edge. The fit shows good linearity for the response of BC501A detectors over the energy range considered in the present work.

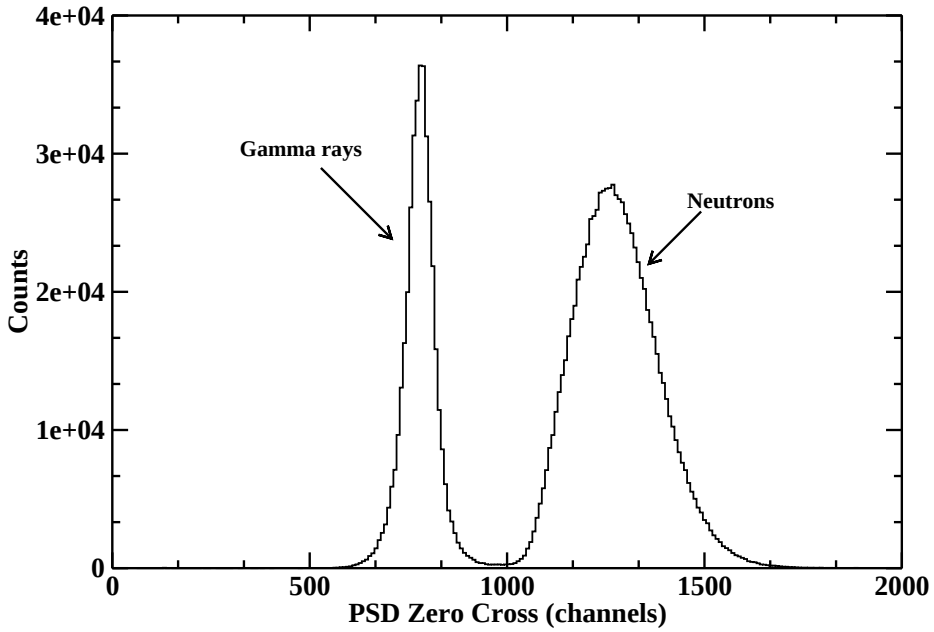

Figure 2.8: The histogram showing $n-\gamma$ discrimination based on Z/C technique at 120 KeVee threshold from a BC501A detector. The X axis represent the Z/C timing of the pulse produced by neutrons and γ-rays inside the detector.

2.6.2 n - γ discrimination

The standard technique for $n-\gamma$ discrimination using the Z/C method relies on the shape of the light output pulse for different radiations interacting inside the detector. The Z/C time of the pulse varies accordingly, and this technique is used for $n-\gamma$ discrimination employing the home made PSD module. The performance of the module was tested for different threshold settings, and FOM determined [17]. The quality of the n-γ discrimination is usually represented by FOM, which is defined as,

$$FOM = \frac{n_p - \gamma_p}{n_{FWHM} + \gamma_{FWHM}} \tag{2.1}$$

where n_p, n_{FWHM}, and γ_p, γ_{FWHM} are the centroid and Full Width at Half Maximum (FWHM) of the neutron peak and γ peak respectively. A histogram showing n-γ separation obtained at 120 keVee threshold using ^{241}Am-^{9}Be source is displayed in Figure 2.8. A clear separation between peaks corresponding to $\gamma-$rays and neutrons can be noticed in the figure. The FOM $\approx$1.6 shows excellent

quality of $n-\gamma$ discrimination for light outputs with low detection threshold as low as ≈120 keVee. The FOM was found to be improving further with increase in threshold. For online experiments, the separation of neutron events can further be enhanced by simultaneous measurements of particle TOF and PSD, plotted on a two dimensional histogram.

2.6.3 Timing response

Fast-timing response of neutron detectors are crucial, as they are used in time of flight measurement for deriving the energy spectrum of fast neutrons produced in nuclear reactions. In order to estimate the time response of a liquid cell, a TOF was setup in coincidence with another fast detector. The effective time resolution will have contributions from both detectors, according to the formula,

$$\sigma_{ab} = \sqrt{\sigma_a^2 + \sigma_b^2} \tag{2.2}$$

where σ_a and σ_b are time resolutions of individual detectors.

The time resolution of a single liquid cell was derived by replacing the coincidence detector with another BC501A. The $\gamma-\gamma$ correlation peak from a radioactive source ^{22}Na has been used to find the intrinsic time spread of BC501A. Using the pulse processing electronics described, the best FWHM attained for the correlation peak was 1.34 ns, which implies a single detector resolution of ≈ 950 ps. Also, to account for signal deterioration caused by long BNC cables (around 30 m) used for signal transport from detectors to electronics in the data room, coincidence TOF measurement was repeated by including such long cables. In this case, amplitude attenuation has been compensated by increasing bias voltage. The time resolution of a single cell in the latter case was found to be ≈1 ns. The FWHM of γ peak is desired as small as possible since it is the reference peak used for converting the TOF spectrum into absolute time (T_{abs})

in ns using the relation,

$$T_{abs}(ns) = (n_{ch} - \gamma_{peak})\ C(ns/ch) + T_{\gamma}(ns) \tag{2.3}$$

where C is the calibration constant and T_{γ} is the TOF of γ-rays in ns. γ_{peak} and n_{ch} are the centroid of γ peak and neutron TOF (in channel numbers) respectively. The uncertainty in kinetic energy derived from TOF will have contributions from both time resolution (ΔT) and length (ΔL) of neutron cell. It is estimated that the energy resolution is better than 0.5 MeV up to 7 MeV of neutron energy.

2.7 Performance evaluation of MWPC detectors

The performance characteristics of MWPC were tested offline using a ^{252}Cf source of strength $\approx$1 μCi. The source was mounted at a distance of 25 cm to ensure uniform illumination of the MWPC. By maintaining the chamber vacuum at $\approx$ 5×10^{-6} mbar, a constant flow of iso-butane gas at 3-4 mbar pressure has been regulated inside the detector volume. The bias voltage for MWPC was optimized between 420V - 450V, which provides sufficient amplitude to the anode signal, well above the CFD threshold ($\approx$25 mV).

Figure 2.9 displays a block diagram of the electronics utilized in the MWPC offline test. Indigenous fast timing pre-amplifiers were used to amplify the MWPC's position and timing signals. The anode signal at the pre-amplifier output was given to a CFD, model *Phillips Scientific 715*, for time pick-off. A Gate and Delay Generator (GDG) was used to delay the CFD pulse, which was then employed as the master strobe for the Time to Digital Converter (TDC). All four position signals of MWPC at pre-amplifier output were further amplified by a Variable Gain Amplifier (VGA), model *Phillips Scientific 777*. The output of VGA was processed through a CFD and delayed properly using a GDG in order to coincide the signals within the TDC range of 400 ns.

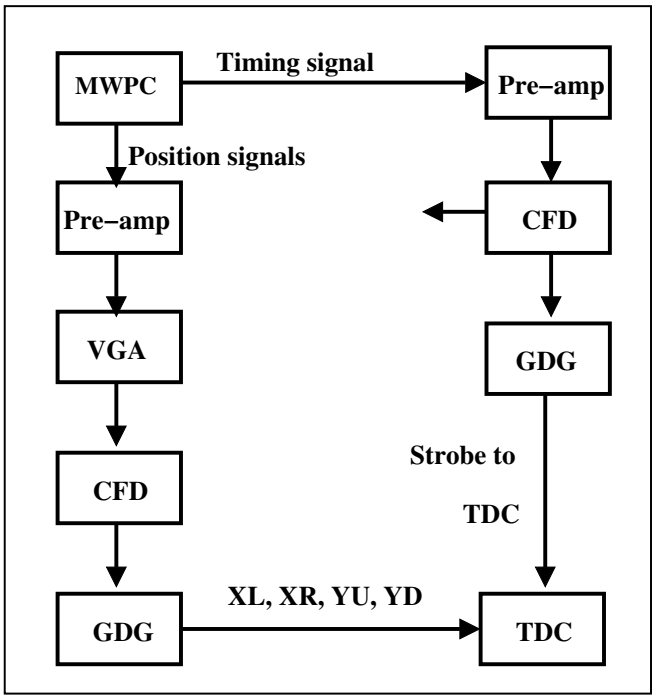

Figure 2.9: A block diagram of signal processing electronics used for the offline examination of MWPC detectors.

2.7.1 Two-dimensional position information

Figure 2.10 shows the time difference spectra recorded, w.r.t. the anode signal, from the two ends of position electrodes X and Y, which are labelled as X_L, X_R, Y_U and Y_D. The overall spread in the spectra can be matched with the end-to-end delay of each position electrode, knowing the TDC calibration (≈0.1 ns/ch). The spread is ≈ 1600 channels in X and 800 channels in Y, which bears a close resemblance to the end-to-end delay of 160 ns and 80 ns in X and Y frames, respectively. The difference between adjacent peaks in the spectra corresponds to the tap-to-tap delay of 2 ns. There are 80 such peaks in the X position spectrum and 40 in the Y position spectrum, respectively. Though wires are soldered with 1.2 mm separation, two wires are grouped together and given a delay tap in the position electrodes. Consequently, the position resolution in this configuration is ≈ 2.4 mm in both the X and Y directions.

The position information in X and Y was derived using the relations, $X = X_L - X_R$ and $Y = Y_U - Y_D$, considering the centre of MWPC as the

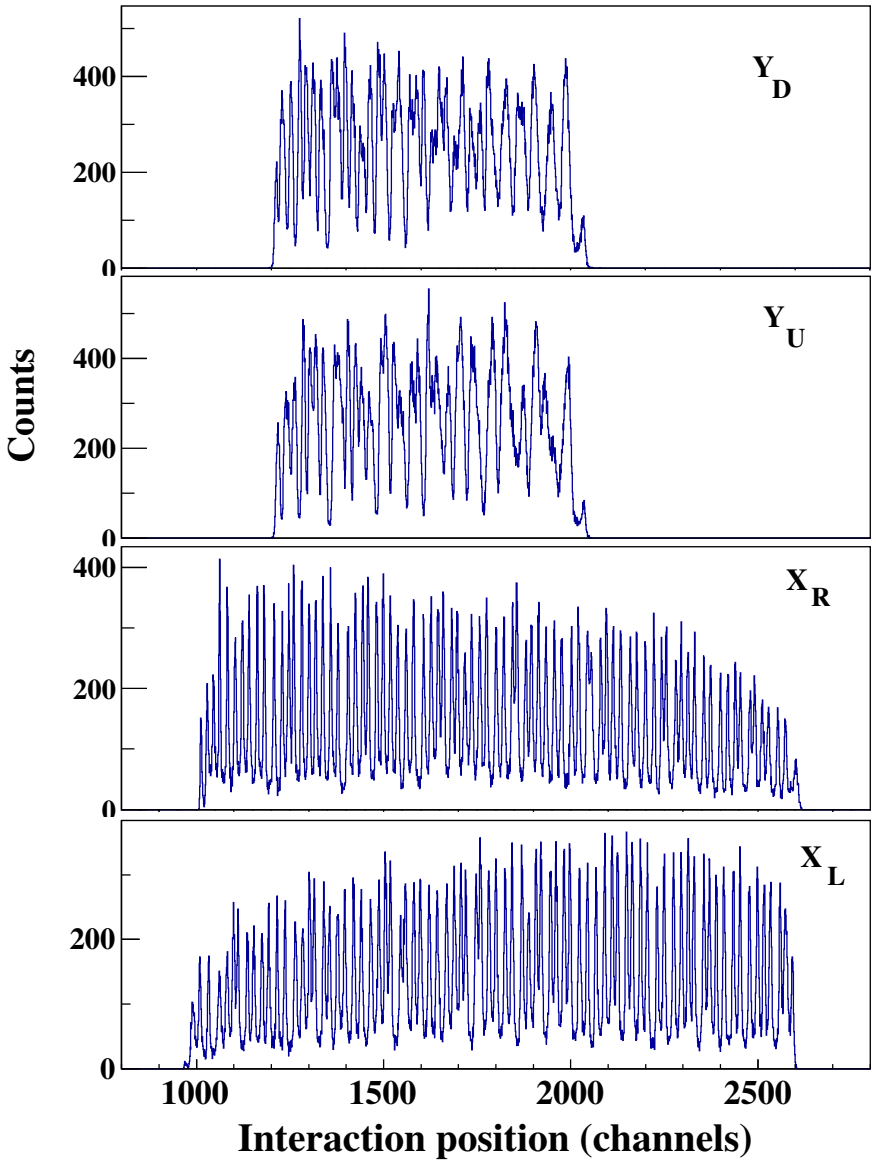

Figure 2.10: Raw position signals extracted from the ends of X and Y position electrodes. The spectra obtained from the ends of a position electrode are expected to be mirror images to each other.

origin (0,0). Following appropriate position calibration, these spectra can be used to determine the precise path length of complementary fragments. The two-dimensional position spectra obtained by plotting Y v/s X for both MWPC detectors are shown in Figures 2.11 (a), (b). Excellent uniformity in position response in the entire range of X and Y can be noticed for both detectors.

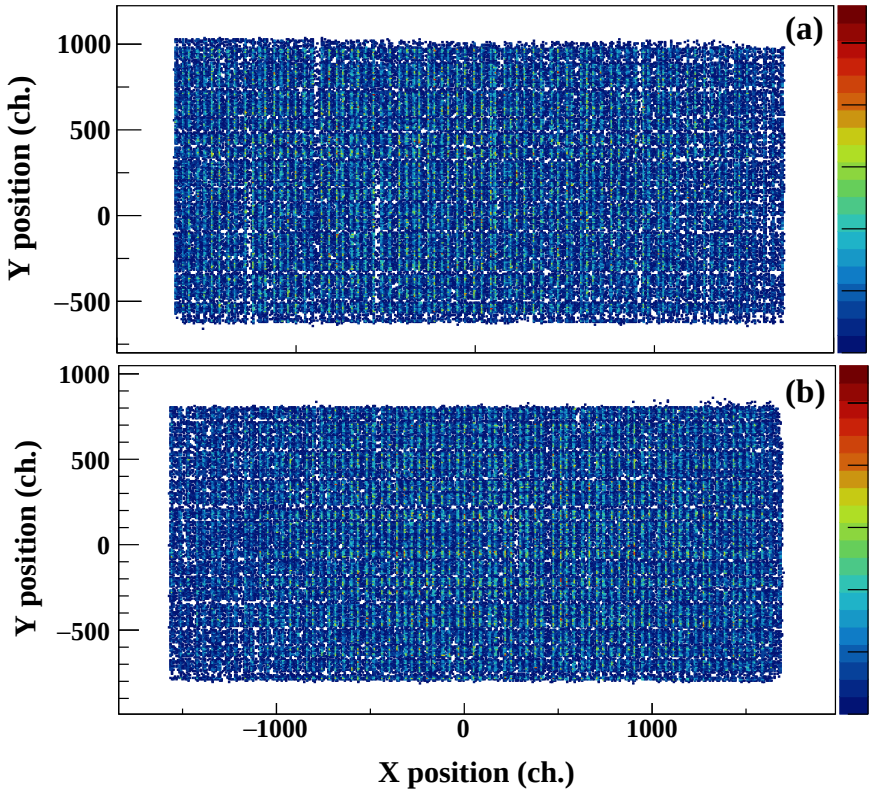

Figure 2.11: Interaction positions derived from the raw position signals. Panels (a) and (b) show the two-dimensional plot of Y versus X for the two MWPC detectors, highlighting the uniformity in position spectra.

2.7.2 Linearity

Position linearity is another important parameter that characterises the performance of the detector. Since the interaction position is extracted by the delay line technique, the linearity in the position spectra can be linked directly with the performance of the delay lines. According to the technical data sheets of *Rhombus Industries Inc.*, model *TZB 12-5* delay chips, the tap-to-tap delay is precisely 2.0 ns with a resolution of 500 ps. Hence, the difference between two adjacent peaks is expected to be $\approx$ 20 channels. Figure 2.12 shows the X position spectrum, enlarged to a small region to view the adjacent peaks. A linearity fit was applied between the measured channel difference and the expected time delay, which is 2.0 ns. The mean of the peaks is found to be linear over the whole range of position spectra. The measured slope was 0.0985 ns/channel, which is

near the 0.1 ns/channel predicted by the TDC calibration.

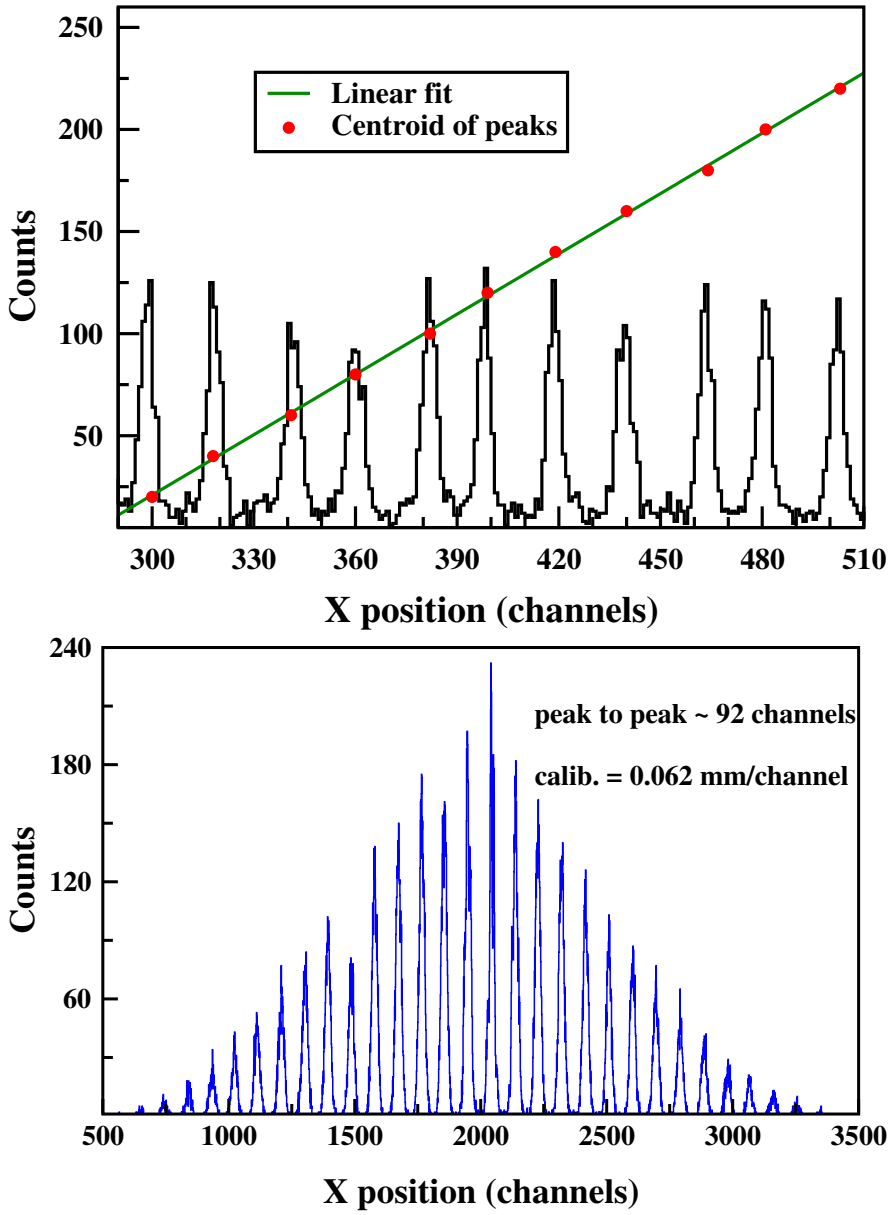

Figure 2.12: Position response linearity of an MWPC detector. (top) Enlarged view of X position spectrum. Red circles denote the centroid of each peak. A linear fit to these points are also shown. (bottom) Masked position spectrum showing discrete peaks corresponding to hole position on the detector mask (see text for details).

The mask test is a complementary method to confirm the position linearity of MWPC detectors. In the mask test, the active area of the MWPC detector is covered with a rectangular sheet of 2 mm thickness. Discrete thru-holes are made on the sheet at a uniform separation of $\approx$ 5 mm and diameter of $\approx$ 1.0

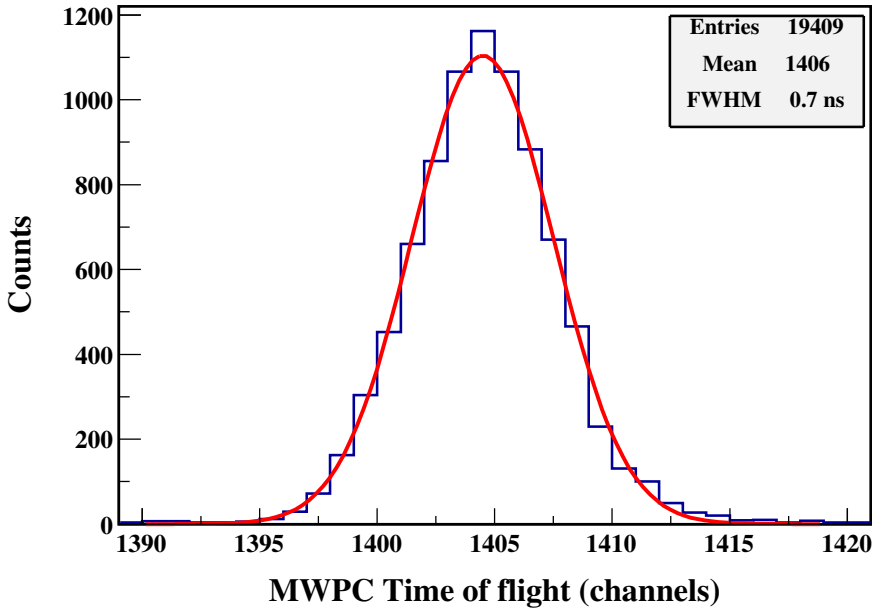

Figure 2.13: Time of flight spectrum of elastically scattered ^{48}Ti beam detected using MWPC. RF of the beam pulse was used as *START* to the time of flight measurement.

mm. As a result, the charged particles emitted by the radiation source that passes through the holes alone will generate detector signals. The thickness of the sheet is sufficient to stop other charged particles. Therefore, the masked position spectrum is expected to show well-defined peaks at 5 mm separation uniformly. The position spectrum obtained from the mask test is shown in Figure 2.12. As anticipated, the spectrum shows uniformly distributed peaks with a peak to peak separation of $\approx$ 5 mm. The intensity distribution is related to the position of the radiation source. The results from both of these measurements affirm the position response linearity of MWPC detectors.

2.7.3 Timing response

The fast-timing response of MWPC detectors has been measured online by detecting ^{48}Ti pulsed beam scattered from thin ^{197}Au targets. A time of flight was set-up with MWPC detectors as *STOP* detectors, where *START* was generated

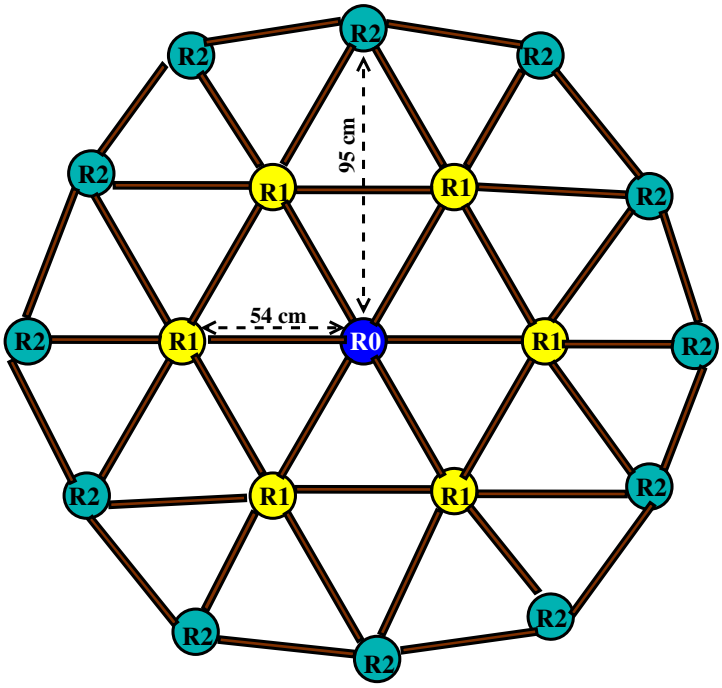

Figure 2.14: Schematic representation of a segment of NAND detectors used for cross-talk measurement. Reference detector R0 and 18 neighbouring detectors in two rings R1 and R2 are shown in the setup [25].

from the RF of the beam pulse. Figure 2.13 displays a typical time of flight spectrum of the scattered beam obtained in this measurement. To estimate the best value of time resolution, a 4 mm $\times$ 4 mm position gate was applied to the TOF spectrum, which reduced the angular uncertainty. The FWHM of the peak was observed to be $\approx$ 700 ps. The time spread of the beam pulse has been measured separately, and it was found to be $\approx$ 480ps. Using the formula 2.2, the intrinsic time resolution of MWPC is determined to be $\approx$ 500 ps.

2.8 Measurement of cross-talk probability

Large arrays of neutron detectors face problems of cross-talk, which can distort the neutron measurements, especially the neutron-neutron correlation measurements [25–28]. Cross-talk occurs when the same neutron interacts, scatters, and deposits energy (above the detection threshold) in two or more neighbouring neutron detectors in the array. Though the interaction of neutrons with organic

scintillators takes place through various channels, n-p scattering is considered the major channel responsible for cross-talk [29]. Studies have indicated that cross-talk probability depends on various factors such as incident neutron energy, detection efficiency, separation between detectors in the array, etc.[26, 30]. To obtain a quantitative estimate of the cross-talk effect in the NAND array, we have performed an offline measurement using neutrons from the ^{241}Am-^{9}Be (Am-Be) source.

The test was performed on a segment of NAND consisting of 19 nearest detectors arranged in the configuration shown in Figure 2.14. It consists of a reference detector R0 and neighbouring six detectors in ring R1 and twelve detectors in ring R2, whose radial distances from the reference detector are $\approx$ 54 cm and $\approx$ 95 cm, respectively. An ^{241}Am-^{9}Be radio-active source was kept at the centre of the spherical chamber of NAND, and a NaI(Tl) gamma ray detector was mounted close to it. The Am-Be source decays by emitting one neutron followed by a high energy (4.4 MeV) gamma ray with a branching ratio $\approx$ 89 % [31]. A hardware coincidence was setup between NaI(Tl) and the reference neutron detector signals to identify the decay event and serve as the master trigger for data acquisition. TOF and PSD data were recorded from all BC501A detectors. Since only one neutron per event is emitted by the source, all neutron-neutron coincidence events observed in detectors in the rings are assumed to be due to cross-talk. The neutron-neutron coincident events in each detector were analyzed by applying software conditions to neuron events in the reference detector, and cross-talk probability was estimated accordingly.

Cross talk probability between a pair of detector is defined as,

$$P_{ab} = N_{ab}/N_a \tag{2.4}$$

where N_a is the number of neutrons recorded in detector a and N_{ab} is the number of neutrons scattered from detector a to b and registered in both a and b.

The average number of cross-talk events observed between reference detec-

tor and any of the neighboring detectors of rings R1 and R2 are given in Table 2.1. The cross-talk probability for detectors in the near vicinity was found to be

Table 2.1: Cross talk probability between two detectors as a function of distance.

Ring	Distance(cm)	Neutron Events in R0	Cross talk events	P_{ab}
R1	54	592397	270	$4.6\pm0.28 \times 10^{-4}$
R2	95	592397	78	$1.3\pm0.15 \times 10^{-4}$

4.6×10^{-4}. To estimate the experimental cross-talk probability in a typical heavy ion reaction where the neutron multiplicity is more than one, it is important to know the measured neutron multiplicity of the reaction. Recent measurement of neutron multiplicity in fission of ^{256}Rf at $\approx$ 58 MeV excitation energy showed total neutron multiplicity $\approx$ 8.3 in which the multiplicity per fragment was reported to be $\approx$ 3.0 [5]. Neutron multiplicity per fragment is important as these neutrons are kinematically focused along the fragment direction, which increases the probability of cross-talk. Considering a typical reaction with an average of three neutrons emitted per fragment, the maximum cross-talk probability P_{ab} for this system can be estimated as $\approx 1.4\pm0.8\times10^{-3}$. This value is in close agreement with the experimental cross-talk probability of $1.06\pm0.08\times10^{-3}$ reported for the large detector array DEMON [30].

2.9 Beam dump radiation shield

Typical heavy ion fusion fission reactions experiments in NAND use targets of a few hundred μg/cm^2 thick foils, which offer minimal energy loss to the particles. The non-interacted and scattered beam particles are dumped on a beam catcher, which is a tantalum sheet placed at the end of the beam pipe $\approx$ 4 m downstream from the target. The interaction of these energetic heavy ions with beam dump may result in secondary background radiations including fast neutrons, which

should be suppressed for unambiguous measurement of neutrons. This is achieved by designing a suitable radiation shield surrounding the beam dump, whose dimension and material composition were optimized by Monte Carlo study using FLUKA [32, 33].

Paraffin wax is one of the easily available shielding materials enriched with hydrogen. We selected paraffin wax as the shielding material, which slows down the fast neutrons through multiple collisions. As the fast neutrons get thermalized in the medium, there is a high probability of thermal neutron capture by hydrogen, emitting 2.225 MeV γ-rays. This can be minimized by adding boron to the shielding medium, which leads to ^{10}B(n, ^{4}He)^{7}Li reaction giving only 0.478 MeV γ-rays and also reduces the probability of thermal neutron capture by hydrogen. From simulation, the optimized composition of the shielding material was found to be 70 % (mass fraction) of paraffin wax mixed with 30 % of boric acid, which gives 5 % of boron. The shielding geometry has a rectangular shape consisting of borated paraffin blocks. The overall dimensions of the shielding blocks are 100 (l)×80 (h)×80 (w) cm^3 and their total weight ≈ 500 kg. An outer layer of a 7 cm thick lead wall is incorporated to attenuate the secondary γ-rays produced at the beam dump.

The effectiveness of borated paraffin in neutron shielding was tested offline using a ^{252}Cf source. It was performed by setting up a TOF between a BaF_2 and BC501A detectors. The source was kept very close to BaF_2 and BC501A was mounted ≈100 cm away. The TOF of neutrons emitted by ^{252}Cf was recorded with this setup, in which the acquisition trigger was generated from BaF_2. The measurement of TOF along with the pulse shape analysis using the PSD technique helped to separate the flux of neutrons from γ rays detected in the BC501A detector. The measurement was carried out with and without borated paraffin blocks in between the detectors. Figure 2.15 shows the background suppressed TOF spectrum obtained with and without paraffin shielding blocks. A clear suppression of neutrons can be observed when borated paraffin is introduced into

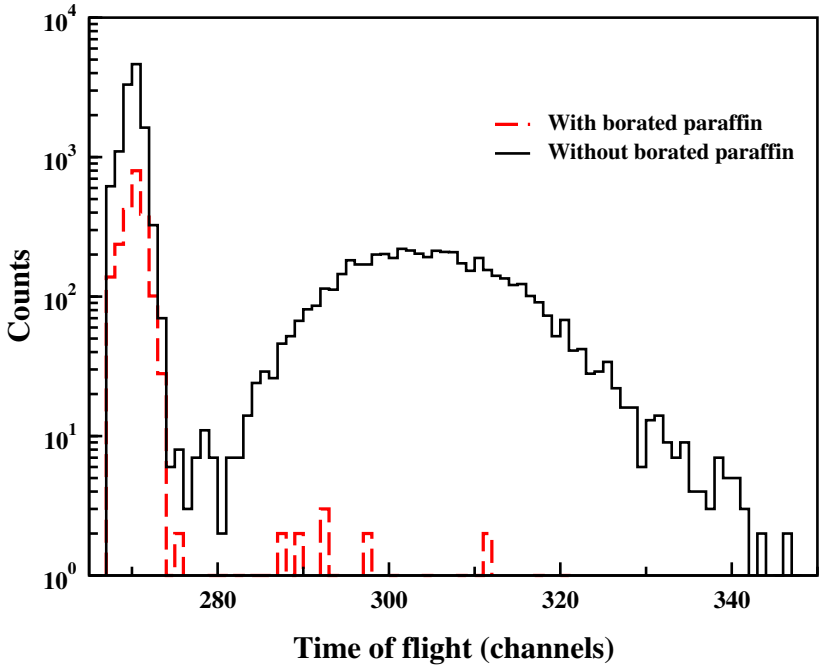

Figure 2.15: TOF spectra of neutrons and γ-rays from ^{252}Cf. Solid black spectrum represents TOF distribution without paraffin block between source and detector, and dotted red line shows the TOF spectrum with paraffin blocks to suppress neutrons.

the flight path. The performance of borated paraffin in neutron shielding was further estimated using the FLUKA calculation. In the simulation, a 2 mm thick tantalum (beam catcher) was bombarded with a 25 MeV proton beam. The neutrons produced in this reaction have an average energy of $\approx$ 1.8 MeV and are distributed to higher energies above 15 MeV. When a shielding block of borated paraffin was applied to this neutron flux, the suppression (number of neutrons escaped/ number of neutron incidents) achieved was $\approx 10^{-4}$.

2.10 In-beam measurements

On-line measurement was carried out to demonstrate the performances of detector systems and the array as a whole. A pulsed beam of ^{19}F at 110 MeV laboratory energy ($\approx$18 % above fusion barrier) was incident on a ^{208}Pb target of thickness 700 μg/cm^2. Two MWPC detectors were mounted at fission folding angle to detect fragments. The fast neutrons emitted in coincidence with fission

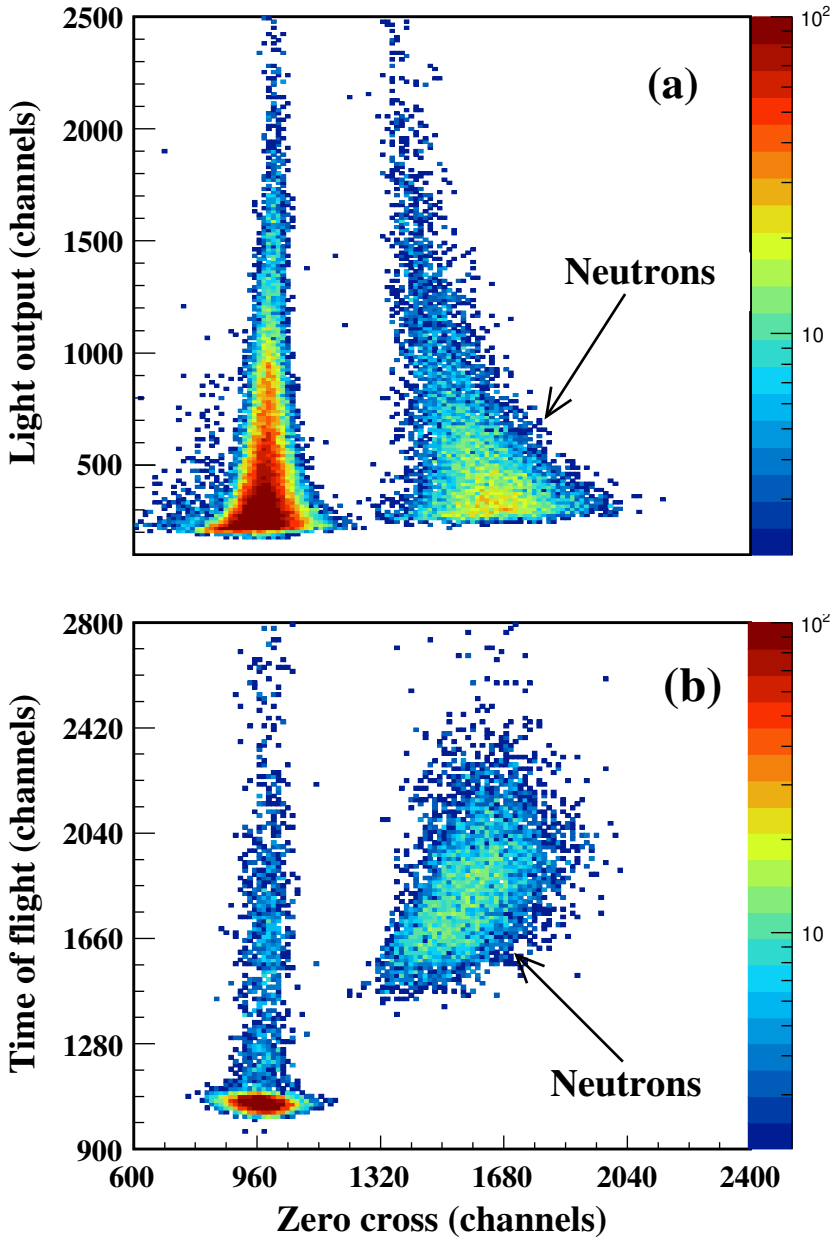

Figure 2.16: Two dimensional histograms showing n-γ discrimination using (a) Z/C time vs. light output and (b) Z/C time vs. TOF for the reaction ^{19}F+^{208}Pb.

were detected using BC501A detectors. The list-mode data were collected using the *VME*-based data acquisition system.

The determination of the energy spectra of neutrons from recorded TOF is extremely important as it provides information regarding nuclear temperature,

neutron multiplicity, etc. Therefore, a clear discrimination of neutron events from other radiation backgrounds, irrespective of neutron energy, is highly desired. For high energy neutrons, the time of flight difference would not be sufficient to get a clear separation between neutrons and γ-rays. But by recording TOF and zero-cross time together, one can achieve n-γ discrimination. Two-dimensional histograms representing Z/C time plotted as a function of light output as well as TOF obtained from this reaction are displayed in Figure 2.16. The figure shows distinct and well-separated bands of neutron and γ events. A software gate cut around the neutron events in Z/C time v/s TOF can be used for further analysis of neutron data.

The performance of the array is further demonstrated by comparing the results of mass-gated neutron multiplicity measured in the super-heavy mass region [5, 34]. Neutron multiplicities associated with symmetric and asymmetric mass division of ^{258}Rf have been measured [34]for the reaction ^{50}Ti beam bombarded on ^{208}Pb target at 294 MeV incident energy. A similar reaction using ^{48}Ti beam bombarded on ^{208}Pb target at 275 MeV incident energy has been performed in NAND array recently [5]. An advantage of a large detector array is that a large amount of data is available at various angles, which helps to extract multiplicities with lower uncertainties. The mass gated pre-scission neutron multiplicity (M_{pre}), post-scission neutron multiplicity (M_{post}) and transient time delay (τ_{delay}) in the fission of CN from two measurements are summarized in Table 2.2

Table 2.2: Comparison of neutron multiplicity measurements in super heavy mass region with a reference reaction [34]. Ref. [5] shows IUAC measurements.

System	E_{lab} (MeV)	Asymmetric cut		Symmetric cut		τ_{delay} (zs)
		M_{pre}	M_{post}	M_{pre}	M_{post}	
^{50}Ti+^{208}Pb	294	1.9 ± 0.8	6.3±0.6	2.2±0.8	6.8±0.4	≈45
^{48}Ti+^{208}Pb	275	1.66±0.07	5.32±0.05	2.23±0.07	6.02±0.07	≈67

The marginal increase in multiplicity and decrease in the time scale of ^{50}Ti+^{208}Pb reaction may be attributed to the excess excitation energy of the compound nucleus. It must be noted that there is a remarkable difference in

error bars between these two measurements. For instance, in Ref. [34], the pre-scission neutron multiplicities associated with symmetric and asymmetric mass split were reported with a large error bar (More than 35 %), whereas the NAND measurements showed results with better than 5 % uncertainty. Moreover, the NAND measurements have been performed with 0.3 pnA beam current, with comparatively lower statistics, but with more number of detectors. The consistency in the correlation of experimental observables and similar interpretation of underlying physics processes in these two independent measurements demonstrate the relevance of the NAND array for high-precision measurements in heavy and super-heavy mass regions.

After the commissioning of the neutron detector array facility, many research experiments have been performed successfully. Mass-gated neutron multiplicities measured in heavy and super-heavy mass regions establishing the presence of quasi-fission have been the highlight of some of these recent experiments [4, 5, 35–37]. With the availability of high energy heavier beams from LINAC, the present facility will open up new possibilities to perform a variety of experiments in the heavy mass region, especially studies on neutron multiplicity distributions, neutron correlation studies, multi-chance fission, etc.

2.11 Summary Conclusion

The characteristics and performance of the newly commissioned detector array, consisting of 100 neutron detectors, have been presented. The design features of the detector array, the design and development of a pair of large area multi-wire proportional counters, pulse processing electronics for fission and neutron detectors, the high voltage power system of PMTs, and the VME-based data acquisition system are described. The solid angle subtended by the array is $\approx$ 3.3 % of 4π and the energy resolution shown by the individual detector is better than 0.5 MeV up to 7 MeV neutron energy. The performance evaluation of BC501A detectors shows appreciable linearity of the light output, excellent n-γ

discrimination, and time resolution.

Pulse shape discrimination in BC501A with custom-made electronic modules exhibits good performance (FOM ≈1.6) even at considerably low threshold of 120 keVee. Multi-wire proportional counters used for fission fragment detection yielded good position linearity, position resolution (≈ 2.5 mm) and time resolution (≈ 500 ps). The cross-talk probability between neighbouring detectors of the NAND array was measured using an ^{241}Am-^{9}Be source. For typical nuclear reaction studies, where neutron emission per fragment is less than 5, the average cross-talk probability is estimated to be ≈ 1.4×10^{-3}. A beam dump designed and simulated using FLUKA, and fabricated using borated paraffin blocks with lead covering showed excellent suppression of secondary neutrons and γ-rays. The upcoming chapter will discuss about FLUKA calculations, as well as comparisons between these calculations and measurements, significant to the NAND facility.

In conclusion, the in-beam performance of the detectors is excellent, and the array is being used for mass-gated neutron multiplicity measurements in heavy and near super-heavy element nuclei. The overall features make this facility suitable for a range of nuclear reaction studies, especially fission studies around Coulomb barrier energies.

Bibliography

[1] R. du Rietz, E. Williams, D. J. Hinde, M. Dasgupta, M. Evers, C. J. Lin, D. H. Luong, C. Simenel, and A. Wakhle, Phys. Rev. C **88**, 054618 (2013), https://link.aps.org/doi/10.1103/PhysRevC.88.054618.

[2] D. Hilscher and H. Rossner, Ann. Phys. Fr. **17**, 471 (1992), https://doi.org/10.1051/anphys:01992001706047100.

[3] D. J. Hinde, D. Hilscher, H. Rossner, B. Gebauer, M. Lehmann, and M. Wilpert, Phys. Rev. C **45**, 1229 (1992), https://link.aps.org/doi/10.1103/PhysRevC.45.1229.

[4] N. Kumar, S. Verma, S. Mohsina, J. Sadhukhan, K. Rojeeta Devi, A. Banerjee, N. Saneesh, M. Kumar, R. Mahajan, M. Thakur, G. Kaur, A. Rani, Neelam, A. Yadav, Kavita, R. Kumar, Unnati, S. Mandal, S. Kumar, B. Behera, K. Golda, A. Jhingan, and P. Sugathan, Physics Letters B **814**, 136062 (2021), https://doi.org/10.1016/j.physletb.2021.136062.

[5] M. Thakur, B. R. Behera, R. Mahajan, G. Kaur, P. Sharma, K. Kapoor, K. Rani, P. Sugathan, A. Jhingan, N. Saneesh, R. Dubey, A. Yadav, A. Chatterjee, M. B. Chatterjee, N. Kumar, S. Mandal, S. K. Duggi, A. Saxena, S. Kailas, and S. Pal, Phys. Rev. C **98**, 014606 (2018), DOI: 10.1103/PhysRevC.98.014606.

[6] L. Donadille, E. Liatard, B. Benoit, F. Hanappe, L. Stuttgè, G. Rudolf, E. Kozulin, Y. Lazarev, P. Désesquelles, L. Litnevsky, B. Bilwes, J.-F. Bruandet, G. Costa, O. Dorvaux, F. Farget, J. Fayot, G. Guillaume, A. Huck, I. Itkis, M. Itkis, S. Jokic, N. Kondratiev, F.-R. Lecolley, J.-F. Lecolley, Y. Oganessian, G. Perrin, D. Santos, F. Schussler, S. Tomasevic, J.-B. Viano, and B. Vignon, Nuclear Physics A **656**, 259 (1999), https://doi.org/10.1016/S0375-9474(99)00306-1.

[7] G. K. Mehta and A. P. Patro, Nuclear Instruments and Methods in Physics Research Section A: Accelerators, Spectrometers, Detectors and Associated Equipment **268**, 334 (1988), https://doi.org/10.1016/0168-9002(88)90530-X.

[8] S. Ghosh, R. Mehta, G. K. Chowdhury, A. Rai, P. Patra, B. K. Sahu, A. Pandey, D. S. Mathuria, J. Chacko, A. Chowdhury, S. Kar, S. Babu, M. Kumar, S. S. K. Sonti, K. K. Mistry, J. Zacharias, P. N. Prakash, T. S. Datta, A. Mandal, D. Kanjilal, and A. Roy, Phys. Rev. ST Accel. Beams **12**, 040101 (2009), 10.1103/PhysRevSTAB.12.040101.

[9] J. B. Birks, *Theory and practice of scintillation counting* (Pergamon Press, Oxford 1964).

[10] G. F. Knoll, *Radiation Detection and Measurement* (John Wiley, New York 2010).

[11] D. L. Smith, R. G. Polk, and T. G. Miller, Nucl. Instr. and Meth. **64**, 157 (1968), 10.1016/0029-554X(68)90189-4.

[12] A. Jhingan, P. Sugathan, K. S. Golda, R. P. Singh, T. Varughese, H. Singh, B. R. Behera, and S. K. Mandal, Review of Scientific Instruments **80**, 123502 (2009), 10.1063/1.3263911.

[13] A. Jhingan, N. Saneesh, M. Kumar, R. Mahajan, M. Thakur, G. Kaur, K. Kapoor, N. Kumar, M. Shareef, R. Dubey, S. Appannababu, E. Prasad, H. Singh, K. S. Golda, R. Ahuja, B. R. Behera, and P. Sugathan, Review of Scientific Instruments **92**, 033309 (2021), https://doi.org/10.1063/5.0029603.

[14] D. Wolski, M. Moszynski, T. Ludziejewski, A. Johnson, W. Klamra, and Ö. Skeppstedt, Nucl. Instr. and Meth. in Physics Research A **360**, 584 (1995), 10.1016/0168-9002(95)00037-2.

[15] M. Moszynski, G. Bizard, G. Costa, D. Durand, Y. E. Masri, G. Guillaume, F. Hanappe, B. Heusch, A. Huck, J. Peter, C. . Ring, and B. Tamain, Nucl. Instr. and Meth. in Physics Research A **317**, 262 (1992), 10.1016/0168-9002(92)90617-D.

[16] A. Jhingan, H. Singh, R. P. Singh, K. S. Golda, P. Sugathan, S. Mandal, and R. K. Bhowmik, Nucl. Instr. and Meth. in Physics Research A **585**, 165 (2008), 10.1016/j.nima.2007.11.013.

[17] S. Venkataramanan, A. Gupta, K. S. Golda, H. Singh, R. Kumar, R. P. Singh, and R. K. Bhowmik, Nuclear Instruments and Methods in Physics Research Section A: Accelerators, Spectrometers, Detectors and Associated Equipment **596**, 248 (2008), https://doi.org/10.1016/j.nima.2008.07.156.

[18] A. Jhingan, Pramana **85**, 483 (2015), 10.1007/s12043-015-1067-8.

[19] H. Stelzer, Nucl. Instr. and Meth. **133**, 409 (1976), 10.1016/0029-554X(76)90423-7.

[20] CAEN Modular Puse Processing Electronics, https://www.caen.it.

[21] A. Chatterjee, K. Ramachandran, and A. Kumar, Linux Advanced Multi-Parameter System (2002), http://www.tifr.res.in/pell/lamps.html.

[22] M. Jain, E. T. Subramaniam, and S. Chatterjee, Review of Scientific Instruments **94**, 013304 (2023), https://doi.org/10.1063/5.0107168.

[23] Nxt gen. Instrumentation and Acquisition Systems, http://www.iuac.res.in/NIAS.

[24] A. A. Naqvi, H. Al-Juwair, and K. Gul, Nucl. Instr. and Meth. in Physics Research A **306**, 267 (1991), 10.1016/0168-9002(91)90331-J.

[25] N. Saneesh, K. Golda, A. Jhingan, S. Venkataramanan, T. Varughese, M. Kumar, M. Thakur, R. Mahajan, B. Behera, P. Sugathan, A. Chatterjee, and M. Chatterjee, Nuclear Instruments and Methods in Physics Research Section A: Accelerators, Spectrometers, Detectors and Associated Equipment **986**, 164754 (2021), https://doi.org/10.1016/j.nima.2020.164754.

[26] N. Colonna, L. Celano, G. D'Erasmo, E. Fiore, L. Fiore, V. Paticchio, G. Tagliente, G. Antuofermo, G. Iacobelli, M. Sacchetti, P. Vasta, and A. Pantaleo, Nuclear Instruments and Methods in Physics Research Section A: Accelerators, Spectrometers, Detectors and Associated Equipment **381**, 472 (1996), https://doi.org/10.1016/S0168-9002(96)00675-4.

[27] J. Valiente-Dobo'n, G. Jaworski, A. Goasduff, F. Egea, V. Modamio, T. Huyuk, A. Triossi, M. Jastrzab, P. Soderstrom, A. Di Nitto, G. de Angelis, G. de France, N. Erduran, A. Gadea, M. Moszynski, J. Nyberg, M. Palacz, R. Wadsworth, R. Aliaga, C. Aufranc, M. Bezard, G. Baulieu, E. Bissiato, A. Boujrad, I. Burrows, S. Carturan, P. Cocconi, G. Colucci, D. Conventi, M. Cordwell, S. Coudert, J. Deltoro, L. Ducroux, T. Dupasquier, S. Erturk, X. Fabian, V. Gonzalez, A. Grant, K. Hadynska-Klek, A. Illana, M. Jurado-Gomez, M. Kogimtzis, I. Lazarus, L. Legeard, J. Ljungvall, G. Pasqualato, R. Perez-Vidal, A. Raggio, D. Ralet, N. Redon, F. Saillant, B. Saygi, E. Sanchis, M. Scarcioffolo, M. Siciliano, D. Testov, O. Stezowski, M. Tripon, and I. Zanon, Nuclear Instruments and Methods in Physics Research Section A: Accelerators, Spectrometers, Detectors and Associated Equipment **927**, 81 (2019), https://doi.org/10.1016/j.nima.2019.02.021.

[28] D. Sarantites, W. Reviol, C. Chiara, R. Charity, L. Sobotka, M. Devlin, M. Furlotti, O. Pechenaya, J. Elson, P. Hausladen, S. Fischer, D. Balamuth, and R. Clark, Nuclear Instruments and Methods in Physics Research Section

A: Accelerators, Spectrometers, Detectors and Associated Equipment **530**, 473 (2004), https://doi.org/10.1016/j.nima.2004.04.243.

[29] J. Wang, A. Galonsky, J. J. Kruse, P. D. Zecher, F. Deák, A. Horváth, A. Kiss, Z. Seres, K. Ieki, and Y. Iwata, Nuclear Instruments and Methods in Physics Research Section A: Accelerators, Spectrometers, Detectors and Associated Equipment **397**, 380 (1997), https://doi.org/10.1016/S0168-9002(97)00806-1.

[30] I. Tilquin, Y. E. Masri, M. Parlog, P. Collon, M. Hadri, T. Keutgen, J. Lehmann, P. Leleux, P. Lipnik, A. Ninane, F. Hanappe, G. Bizard, D. Durand, P. Mosrin, J. Péter, R. Régimbart, and B. Tamain, Nuclear Instruments and Methods in Physics Research Section A: Accelerators, Spectrometers, Detectors and Associated Equipment **365**, 446 (1995), https://doi.org/10.1016/0168-9002(95)00425-4.

[31] I. Murata, I. Tsuda, R. Nakamura, S. Nakayama, M. Matsumoto, and H. Miyamaru, Progress in Nuclear Science and Technology **4**, 345 (2014), https://doi.org/10.15669/PNST.4.345.

[32] T. T. Böhlen, F. Cerutti, M. P. W. Chin, A. Fasso‘, A. Ferrari, P. G. Ortega, A. Mairani, P. R. Sala, G. Smirnov, and V. Vlachoudis, Nucl. Data Sheets **120**, 211 (2014).

[33] A. Ferrari, P. R. Sala, A. Fasso‘, and J. Ranft, CERN-2005-10(2005), INFN/TC_05/11, SLAC − R − 773 (2005).

[34] S. Appannababu, M. Cinausero, T. Marchi, F. Gramegna, G. Prete, J. Bermudez, D. Fabris, G. Collazuol, A. Saxena, B. K. Nayak, S. Kailas, M. Bruno, L. Morelli, N. Gelli, S. Piantelli, G. Pasquali, S. Barlini, S. Valdré, E. Vardaci, L. Sajo-Bohus, M. Degerlier, A. Jhingan, B. R. Behera, and V. L. Kravchuk, Phys. Rev. C **94**, 044618 (2016), 10.1103/PhysRevC.94.044618.

[35] R. Mahajan, B. R. Behera, M. Thakur, G. Kaur, P. Sharma, K. Kapoor, A. Kumar, P. Sugathan, A. Jhingan, A. Chatterjee, N. Saneesh, A. Yadav, R. Dubey, N. Kumar, H. Singh, A. Saxena, and S. Pal, Phys. Rev. C **98**, 034601 (2018), 10.1103/PhysRevC.98.034601.

[36] M. Shareef, E. Prasad, A. Jhingan, N. Saneesh, K. S. Golda, A. M. Vinodkumar, M. Kumar, A. Shamlath, P. V. Laveen, A. C. Visakh, M. M. Hosamani, S. K. Duggi, P. S. Devi, G. N. Jyothi, A. Tejaswi, P. N. Patil, J. Sadhukhan, P. Sugathan, A. Chatterjee, and S. Pal, Phys. Rev. C **99**, 024618 (2019), 10.1103/PhysRevC.99.024618.

[37] N. K. Rai, A. Gandhi, A. Kumar, N. Saneesh, M. Kumar, G. Kaur, A. Parihari, D. Arora, K. S. Golda, A. Jhingan, P. Sugathan, T. K. Ghosh, J. Sadhukhan, B. K. Nayak, N. K. Deb, S. Biswas, and A. Chakraborty, Phys. Rev. C **100**, 014614 (2019), 10.1103/PhysRevC.100.014614.

Chapter 3

Measurements and Monte Carlo calculations of various detector features

Large-volume liquid scintillator cells are widely used in neutron time of flight (TOF) measurements for nuclear physics experiments [1–3]. Fast neutrons detected in an array of cells kept at a large distance from the target allow high-resolution TOF measurements covering a wide range of neutron energies. Accurate estimation of neutron emission flux is of central importance in these measurements involving energy and the angular distribution of neutrons. Unlike charged particles, the interaction of neutrons in the medium of the detector is rare, and therefore observed neutron counts require a correction for detection efficiency to determine the number of emitted neutrons. Due to their intrinsic properties like fast response time, high detection efficiency, and excellent neutron-gamma ($n-\gamma$) discrimination at relatively low energy thresholds, organic liquid scintillator detectors have found wide spread use in fast neutron spectroscopy applications [4].

Neutrons with kinetic energy ranging from a few hundred keV to tens of MeV are usually emitted in typical fusion-fission reactions. It is important to

apply an energy-dependent efficiency correction to determine the total number of neutrons emitted from the collision experiments. Another important aspect to be considered in the estimation of neutron emission flux is the scattering of neutrons by various materials in the flight path. Scattering causes loss of flux in the emission direction and, in addition, generates neutron background for other nearby detectors in the array. The cross-section for neutron scattering depends critically on the characteristics of materials, such as composition, density, and thickness. Monte Carlo simulations can be utilized to incorporate these factors to estimate the percentage loss of flux and neutron background due to scattering from various materials.

In order to determine the overall detection efficiency, the loss of flux due to neutron scattering, etc. of the NAND facility, we have performed a Monte Carlo simulation and validated the results with measurements. The performance characteristics of the NAND array are described extensively in Chapter 2. In this chapter, we discuss in detail the simulation study and the experimental technique used for measuring the response function and detection efficiency of the array. Monte Carlo simulation has been performed using a well-known multi-particle transport code, FLUKA [5, 6]. The results are validated with measurements using neutrons emitted from a ^{252}Cf source. In section 3.1, we present the experimental method used for neutron time of flight measurement and determination of intrinsic efficiency of 5" $\times$ 5" BC501A. In the subsequent sections, FLUKA simulations of scintillation response and detection efficiency are discussed. Section 3.5 describes the role of neutron scattering from target chamber material on neutron flux measurements. The estimation of neutron emission flux from measured neutron counts is described in Section 3.6

3.1 Experimental method for efficiency measurement

There are various methods reported in the literature for measuring fast neutron flux using scintillators [7]. Among them, the associated particle method is considered to be the most accurate technique, in which charged particle(s) emitted along with neutrons are detected in coincidence. Then, a one-to-one correspondence between the charged particle and neutron can be utilized to calculate the number of neutrons emitted per event. For BC501A detectors, we have adopted this method to measure the intrinsic efficiency, which is the ratio of the number of neutrons detected to the number of neutrons incident in the detector volume. For the measurements, spontaneous fission of ^{252}Cf is considered as the reference reaction. Though it is difficult to make one-to-one correspondence between fission and neutron counts due to the statistical nature of neutron emission, the average number of neutrons emitted per fission of ^{252}Cf is accurately known [8]. Therefore, by precise measurement of fission fragments in a fission counter and associated neutrons in BC501A detectors, the detection efficiency can be estimated.

To determine detection efficiency as a function of incident neutron energy (E_n), it is important to take into account the probability distribution of neutron emission $f(E_n)$ in the laboratory frame. Knowing the shape of the distribution function in the rest frame of fission fragments [9, 10], the energy distribution in the laboratory frame can be generated using Monte Carlo codes. The mass and velocity of moving fragments can influence the kinematics of neutron emission, and simulations should take these kinematic effects into account to generate a proper energy distribution. The energy-dependent efficiency can then be obtained from a direct comparison between the measured energy spectrum and the kinematically calculated energy distribution $f(E_n)$.

Most of the fission reactions under study yield neutrons in the energy range

below 20 MeV and FLUKA simulation results are well validated in this energy region [11, 12]. The simulation takes into account both the kinematics of neutron emission from ^{252}Cf source and the response function of liquid scintillators to fast neutrons. In general, the detector response to fast neutrons depends significantly on various factors such as neutron energy, light output resolution, detection threshold, etc. All these factors can be incorporated into Monte Carlo calculations to obtain the light output for a given radiation. The estimation of detector efficiency using FLUKA simulation involves two parts: kinematic simulation to estimate the number of particles reaching the detector volume, known as the reference spectrum, and the simulation of detector response to incident radiation. The kinematic calculation takes care of the emission spectrum of the neutron beam and the solid angle subtended by the detector system. Section 3.2 discusses the calculations involved in defining the reference spectrum of neutrons emitted by ^{252}Cf. And the intrinsic properties of the detection medium are addressed in the simulation of the response function discussed in Section 3.4.

3.2 Neutron energy spectrum of ^{252}Cf

The efficiency measurement using ^{252}Cf source is a model-dependent technique where the neutron emission spectrum is modelled based on experimental observables [13, 14]. The neutron evaporation from an excited fission fragment is considered a cascade process. Le Couteur and Lang expressed the cascade evaporation spectrum of neutrons from an excited system with the formula [10],

$$f(E_n)\, dE_n = \ const.\ E_n^{\lambda}\ exp(-E_n/T_{eff})\ dE_n \tag{3.1}$$

The formula 3.1 is simplified by approximating $\lambda = 0.5$. This yields the Maxwellian distribution [15, 16] (in the centre of mass frame), where the normalization constant is obtained by setting the integral of the probability distribution

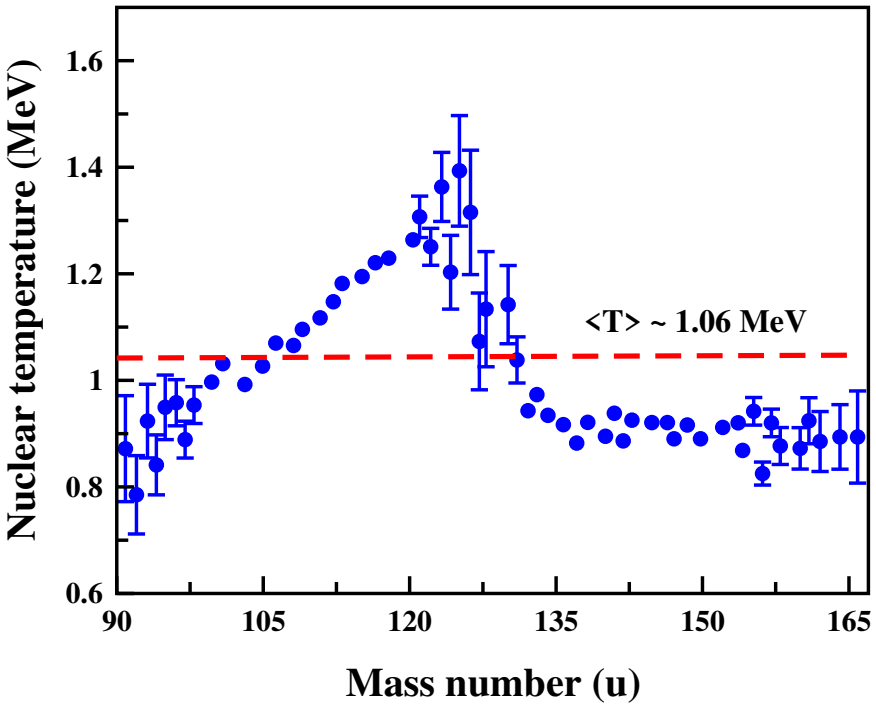

Figure 3.1: The distribution of nuclear temperature as function of fragment mass, reported in [14]. The red dashed line represents the average of this distribution.

function to unity ($\int_0^\infty f(E_n)dE_n = 1$),

$$f(E_n)\ dE_n = \frac{2}{\sqrt{\pi}\ T^{3/2}}\sqrt{E_n}\ exp(-E_n/T_{eff})\ dE_n \tag{3.2}$$

The temperature distribution of fission fragments from ^{252}Cf has been experimentally determined by various groups [13, 14]. Figure 3.1 displays the nuclear temperature as a function of fragment mass reported in Ref. [14]. The average of this distribution is found to be $\approx$ 1.06 MeV as shown by the dashed line in the figure. Using experimentally determined average nuclear temperature, the probability distribution of neutron energies in the rest frame of fragments can be estimated by using Equation 3.2. To determine the efficiency of BC501A as a function of energy, Equation 3.2 has to be converted into the laboratory frame.

A vector diagram showing particle emission from a moving source at an arbitrary angle relative to fission direction is given in Figure 5.8. Solid lines represent the neutron emission in which the fragment is detected in the same hemisphere

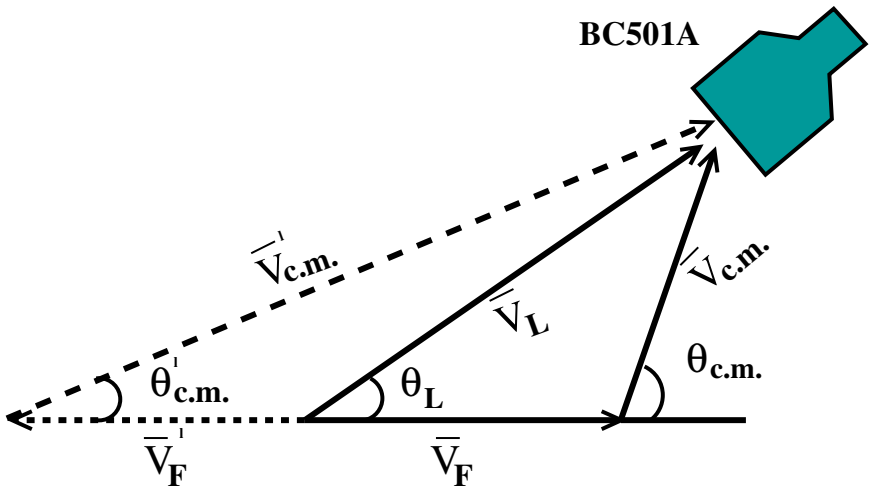

Figure 3.2: Vector diagram showing the emission of neutrons from an accelerated fragment and the interdependence of velocity vectors in c.m. and laboratory frame. The solid line indicates the emission of neutrons from the fragment in the same hemisphere, whereas the dotted line represents neutron emission from the complementary fragment. The label for fragment velocity is $\vec{V}_F$, for neutron velocity in c.m. and laboratory frame are $\vec{V}_{c.m.}$ and $\vec{V}_L$ respectively. The corresponding parameters of the complementary fragment are labelled with prime symbol.

as the neutron detector, whereas the dotted lines represent the complementary fragment. Since neutron emission from fully accelerated fragments is kinematically focused along the fission direction, only high energy neutrons from the complementary fragment are expected to reach the detector. As the emission probability falls exponentially with energy, the contribution from complementary fragments can be neglected. The transformation from the centre of mass to the laboratory frame has been made using the following equations,

$$V_L^2 \;=\; V_{c.m.}^2 \;+\; V_F^2 \;+\; 2\; V_{c.m.}\; V_F\; cos(\theta_{c.m.}) \tag{3.3}$$

$$\theta_L \;=\; tan^{-1}\Big(\; \frac{sin(\theta_{c.m.})}{V_F/V_{c.m.} + cos(\theta_{c.m.})}\Big) \tag{3.4}$$

where V_F is the velocity of fragments, $V_{c.m.}$ and V_L are velocities of neutrons in c.m. frame and laboratory frame respectively. $\theta_{c.m.}$ is the emission angle in c.m. frame and θ_L is the laboratory angle. Rewriting Equation 3.3 in terms of energy

we have,

$$E_L = E_{c.m.} + Es/As + 2\sqrt{\frac{E_{c.m.}\ E_S}{A_S}}\ cos(\theta_{c.m.}) \tag{3.5}$$

where $E_{c.m.}$ is the energy of the neutron in the rest frame and E_S/A_S indicates the kinetic energy per nucleon of the neutron source. Since ^{252}Cf undergoes fission through various modes [17], in a given number of fission events, the value of E_S/A_S varies widely [18]. The average kinetic energy per nucleon for lighter and heavier fragments is 0.963 MeV/u and 0.554 MeV/u respectively [18]. These average values are considered for the transformation of neutron energies to the laboratory frame from the c.m. frame. The characteristics of the neutron source in the FLUKA input file were defined according to the Equations 3.2, 5.30 and 3.5, and the resulting energy distribution, $f(E_n)$, has been used as the reference spectrum for efficiency determination.

3.3 Experiment description

3.3.1 The detectors

The detection system consists of a gas detector for fission fragment detection and organic liquid scintillators of the NAND array for fast neutrons. The NAND array uses commercial BC501A liquid scintillators encapsulated in 5" × 5" cylindrical cell. The cell is optically coupled to a 5" diameter photomultiplier tube (PMT) of the type Hamamatsu R4144 enclosed in a μ-metal shield.

A large area (8" × 4") Parallel Plate Avalanche Counter (PPAC) was used for detecting fission fragments from ^{252}Cf. The gas detector was built using two parallel electrodes, consisting of one anode wire frame and a cathode foil frame. The anode frame is made of 20 μm thick gold-plated tungsten wires stretched and soldered on to a 3.2 mm thick printed circuit board at $\approx$ 1 mm wire spacing. Stretched aluminised Mylar foil (polyethylene teraphthalate) was used as the cathode frame. One-side open ^{252}Cf source was fixed on the cathode foil at its

centre, which enables the detection of fission fragments emitted in $\approx 2\pi$ steradian. The electrodes were assembled with 6 mm inter-electrode separation and enclosed in a rectangular aluminium chamber. A steady flow of low-pressure isobutane gas has been maintained in the chamber to act as the detection medium. Henceforth, we will use the term *Cf-chamber* to refer to the gas detector encapsulated with a ^{252}Cf source.

3.3.2 Experimental setup

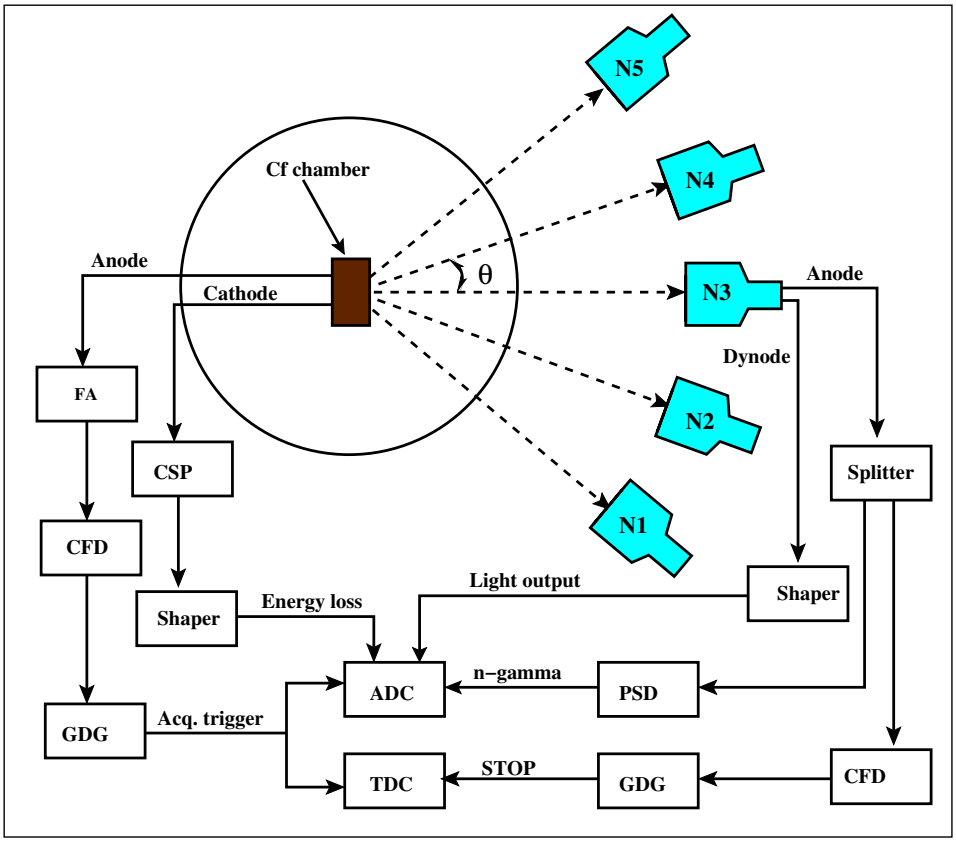

Figure 3.3: Schematic of the experimental setup and electronics for signal processing and data collection.

A schematic of the experimental setup and signal processing circuit is shown in Figure 3.3. The Cf-chamber was placed at the centre of the NAND spherical target chamber, and a set of five structurally identical BC501A detectors, selected from a segment of the NAND array were used for fast neutron detection.

The energy-dependent efficiencies were determined for these detectors (N1-N5) mounted at 18° angular separation, as shown in Figure 3.3. The setup helps to measure and compare the energy-dependent efficiency of multiple detectors simultaneously.

The Cf-chamber was operated with isobutane gas. Detection of isotropic emission of fission fragments is important for estimating the efficiency using ^{252}Cf source. Depending on the gas pressure, the mean free path and consequently the energy loss of fragments (ΔE) vary inside the detector volume. The path length is minimal for fragments emitted perpendicular to the plane of electrodes ($\theta = 0°$) as compared to other directions. Therefore, at lower gas pressures, the path length dependency could alter isotropic detection of fragments when ΔE drops below the detection threshold. The effects can be identified by using multiple neutron detectors mounted at various angles w.r.t. the perpendicular plane of the fission detector, as shown in Figure 3.3. In the present setup, the path length is minimum for fragments emitted along the direction of neutron detector N3. When the Cf-chamber was operated with gas pressure $\approx$ 2 mbar (pressure sufficiently low to minimize triggering by alpha particles from ^{252}Cf), count rate difference of $\approx$ 10-13 % was observed between detectors N1(or N5) and N3. By increasing the operating gas pressure to $\approx$7 mbar, the count rate difference among detectors dropped to less than 5 %. A deep ionization chamber for fission counting may help to avoid path-dependent trigger problems. But for TOF applications, the time resolution would be poor as compared to avalanche counters.

3.3.3 Signal processing and data collection

As shown in Figure 3.3, the signal processing electronics consist of a coincidence circuit for detecting neutrons in correlation with fission events. The set up measures neutron TOF with reference to fission fragments detected in Cf-chamber. Two signals were derived from the Cf-chamber: a fast timing signal from the

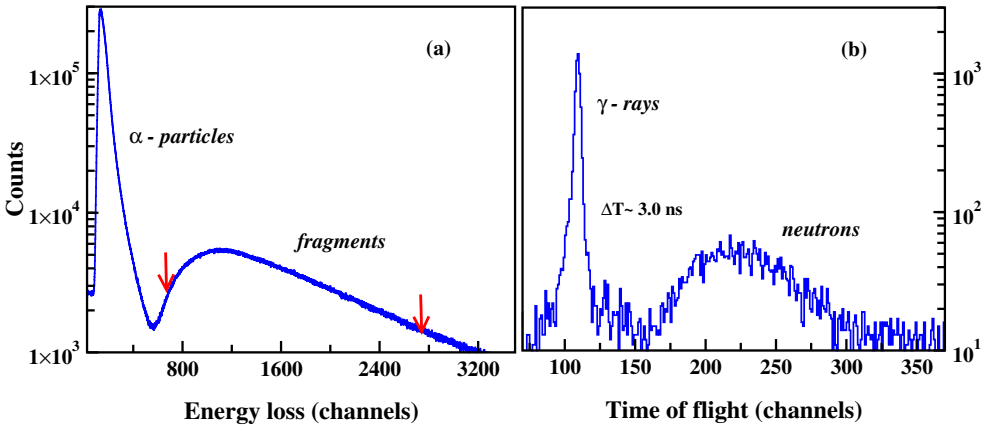

Figure 3.4: Histograms representing various parameters measured in the experiment. (a) Charged particle energy loss (ΔE) histogram from the Cf-chamber. The region between the arrows indicates energy deposited by fission fragments. (b) The histogram showing time of flight of neutrons and γ-rays from ^{252}Cf.

anode and the energy loss ΔE signal from the cathode. The anode signal fed to a fast amplifier (FA) was further processed through a CFD for time pick-off. The CFD output stretched to ≈4 μs using a GDG served as the master trigger of the VME-based data acquisition system. The ΔE signal after pre-amplification through a charge-sensitive pre-amplifier (CSP) was further amplified and shaped by a uni-polar shaping amplifier. The signals from each neutron detector was processed using custom-built electronics containing pulse shape discrimination (PSD) and TOF circuits integrated into a dual channel NIM electronic module [19].

VME ADC (*v785*) was used for acquiring the energy loss signal (ΔE), $n-\gamma$ discrimination signal, and light output signal. TDC (*v775*) was used to record TOF events triggered between fission and each neutron detector. A total of 25 million fission events were recorded using Cf-chamber, of which ≈ 1.5×10^4 events resulted in fission neutron coincidences. The light output spectrum, which is used for setting the energy threshold, was calibrated using known energy γ-rays from standard radioactive sources. Offline analysis of data was performed using ROOT software [20].

The resulting spectra are displayed in Figure3.4(a-b). The light output spectra of BC501A were calibrated in units of keVee (keV electron equivalent) using

known energy γ-rays from radioactive sources such as ^{137}Cs, ^{22}Na, and ^{60}Co. Based on these calibrations, the detection threshold was set to ≈100 keVee. Figure 3.4(a) shows the histogram of energy loss of charged particles in the Cf-chamber. The narrow peak observed in the low-energy part of the spectrum corresponds to alpha particle interactions. This is followed by a broad peak originating from the energy loss of fission fragments. The gain of the spectroscopy amplifier was optimized to have both low and high energy fragments recorded within the range of the ADC. The energy above the alpha peak (energy loss values falling within the range marked by arrows) was used to apply ^{252}Cf fission coincidence condition in analysing the neutron TOF data. The corresponding $n - \gamma$ TOF spectrum is shown in Figure 3.4(b). Unlike in beam experiments, here we have no beam pulse and have to make use of the Cf-chamber as *START*, and that too operated at a low bias voltage to avoid the sputtering of radioactive source material. As a result, the γ-peak is broadened with FWHM ≈ 3 ns. Nevertheless, there is clear separation of neutrons from γ-rays.

From the measured energy spectrum, the intrinsic efficiency ($\eta_{intri.}$) of BC501A detectors has been estimated as,

$$\eta_{intri.}(\%) = \frac{dN_{det.}/dE_n}{dN_{ref.}/dE_n}\ 100 \tag{3.6}$$

where $dN_{det.}$ is the number of neutron detected in a given energy bin dE_n and $dN_{ref.}$ is the neutron counts expected in dE_n according to the reference spectrum. The detection threshold was kept at ≈ 0.5 MeV. The efficiency curve obtained for one of the BC501A detectors, for the energy range ≈ 0.5-10 MeV neutron energy, is shown in the Figure 3.5.

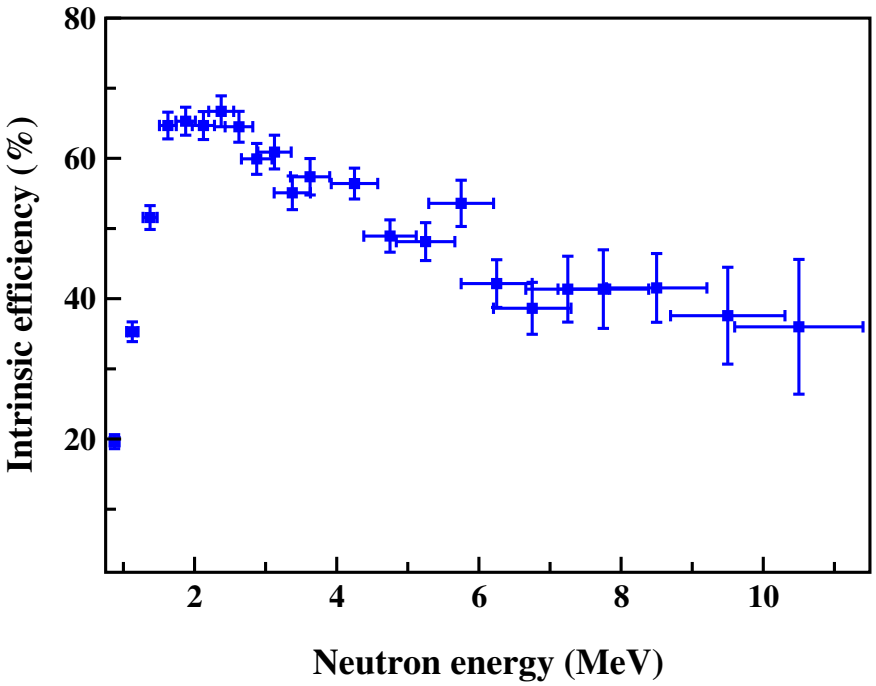

Figure 3.5: Measured intrinsic efficiency, in percentage, of a 5" × 5" BC501A detector as a function of neutron energy.

3.4 FLUKA simulation of BC501A characteristics

The response function and detection efficiency of BC501A for monoenergetic neutrons and γ-rays have been simulated using FLUKA, a well-established Monte Carlo code for simulating particle interaction and transport in scintillator media. FLUKA is used along with an advanced graphical interface, Flair [21], making it a versatile tool for simulation of particle interactions in different materials and detector geometries. GEANT4 [22] models are also commonly applied in detector simulation. However, we preferred FLUKA from the point of view of flexibility, ease of use, and visualization of output files. For low energy ($<$ 20 MeV) neutron interactions, FLUKA uses cross-section data based on the recent evaluations from ENDF/B, JEF, JENDL, etc. [5, 6].

The interaction of fast neutrons with hydrogenous material results in the creation of recoil protons. The mechanism of energy loss and resultant scintil-

lation yield is a characteristic of the detection medium, which is represented by a response function, $R(L, E)$. To obtain the light output spectrum $N(L)$ corresponding to neutron interaction, the recoil proton spectrum has to be folded with the response function of the detector as,

$$N(L) = \int R(L, E)\ N(E)dE \tag{3.7}$$

where $N(E)dE$ is the differential number of recoil protons produced within the energy interval dE around E, $R(L, E)dE$ is the differential probability that a recoil of energy within dE around E leads to a scintillation pulse of amplitude L. The particle-dependent response of organic liquid scintillators and their origin are described in section 3.4.3. The response function for a fixed energy deposition is assumed to be a Gaussian distribution with zero mean value, and FWHM equal to light output resolution (ΔL) [11, 23]. The simulated light output L was randomized using the Gaussian smearing function to account for detector resolution, and a realistic Monte Carlo spectrum can be obtained. The detector resolution ΔL for a given L can be written in parametric form as [23, 24],

$$\frac{\Delta L}{L} = \left(\alpha^2 \ + \ \frac{\beta^2}{L} + \ \frac{\gamma^2}{L^2}\right)^{1/2} \tag{3.8}$$

The resolution parameter β is in general related to light production and attenuation in the scintillator; α is associated with transmission of light from the scintillator to the photocathode; and γ to PMT noise [23]. Since the parameters are highly dependent on the fabrication details, even detectors with similar size and composition may have different α, β and γ values.

3.4.1 Validation of FLUKA simulation

For optimal use of FLUKA simulation in low energy neutron interactions, it is important to have its performance validated in the desired energy range [12]. Arneodo *et al.* have measured the recoil proton response in liquid scintillator

BC501A exposed to monochromatic neutron beams below 20 MeV [23], termed PTB measurements. The intrinsic efficiency of these BC501A detectors has been reported for different neutron energies up to 19 MeV. To benchmark the Monte Carlo code FLUKA for simulating the response function of organic liquid scintillators, these efficiency values were used as the reference data.

To reproduce the PTB data using FLUKA simulation, the matching detector setup has been defined in FLUKA according to the geometrical and material characteristics as reported in [23]. The position and divergence of the beam were defined such that the neutron beam illuminates the longitudinal section to create recoil protons in the scintillator volume, whose depth is equal to the diameter of the cylindrical cell. The simulated light yield N(E) was folded with the detector response function R(L, E) to obtain the experimental light output spectrum N(L). The values of α, β and γ were taken from [23]. The neutron detection efficiency was then estimated from the ratio of the number of recoil protons produced above threshold energy (E_P^{th}) to the number of incident neutrons of energy E_n.

The results of the FLUKA simulation along with PTB data for different neutron energies are summarized in Table 6.1. Six energy points spanning from ≈0.5 MeV to 19 MeV neutron beams have been covered in this calculation. Broadly, the FLUKA simulation reproduces the measured efficiency data very consistently throughout the measured energy range. At detection thresholds (E_P^{th}) near neutron energies (E_n), FLUKA calculations show deviation from measurements ≈15 %. This may be due to uncertainties associated with the experimental threshold settings. The errors in the efficiency measurements of PTB data are followed by the errors in sensitivity reported [23]. After verifying the validity of the simulation, we have applied the model to determine the response function and efficiency of NAND detectors.

Table 3.1: FLUKA calculation of neutron detection efficiencies for 6" × 2" organic scintillator at different energy thresholds. The simulation results are compared with measurements reported in [23].

E_n (MeV)	E_P^{th} (MeV)	Intrinsic efficiency (%)	
		PTB meas. [23]	FLUKA calc.
0.56	0.25	19.9 ± 1.8	26.6
1.2	0.25	36.5 ± 3.0	35.6
2.5	1.40	12.4 ± 1.0	14.1
5.0	1.40	23.1 ± 2.1	22.4
14.8	2.0	11.4 ± 0.9	12.3
19.0	2.0	11.0 ± 1.2	10.6

3.4.2 Estimation of α, β and γ values for NAND detector

The resolution parameters α, β and γ for 5" × 5" BC501A detectors in the NAND array were obtained by comparing the simulated spectrum with measured light output data using monoenergetic γ-rays. The light output was measured using radioactive ^{22}Na source, which emits pair-annihilation γ-rays in the decay process. The Compton energy spectrum corresponding to γ-interaction in the liquid scintillator was collected in coincidence with another detector mounted at 180° with respect to the first detector. The coincidence data was collected in order to minimize the background interactions in the neutron detector. Using known calibration and energy thresholds, the measured light output spectrum was compared with the FLUKA simulated spectrum.

The geometry and material characteristics of the detector were incorporated in the FLUKA calculation. Monoenergetic (511 keV) γ-ray beam was fired to illuminate the full cross-sectional area of the detector. Event-by-event scoring of energy deposited by γ-rays via Compton scattering was written to the output file and analysed. The total number of Compton electrons produced in the detector volume was set to match the integral counts in the experimental Compton spectrum. Figure 3.6 shows the comparison between the measured (points with error bars) and simulated (dashed curve) light output spectrum corresponding

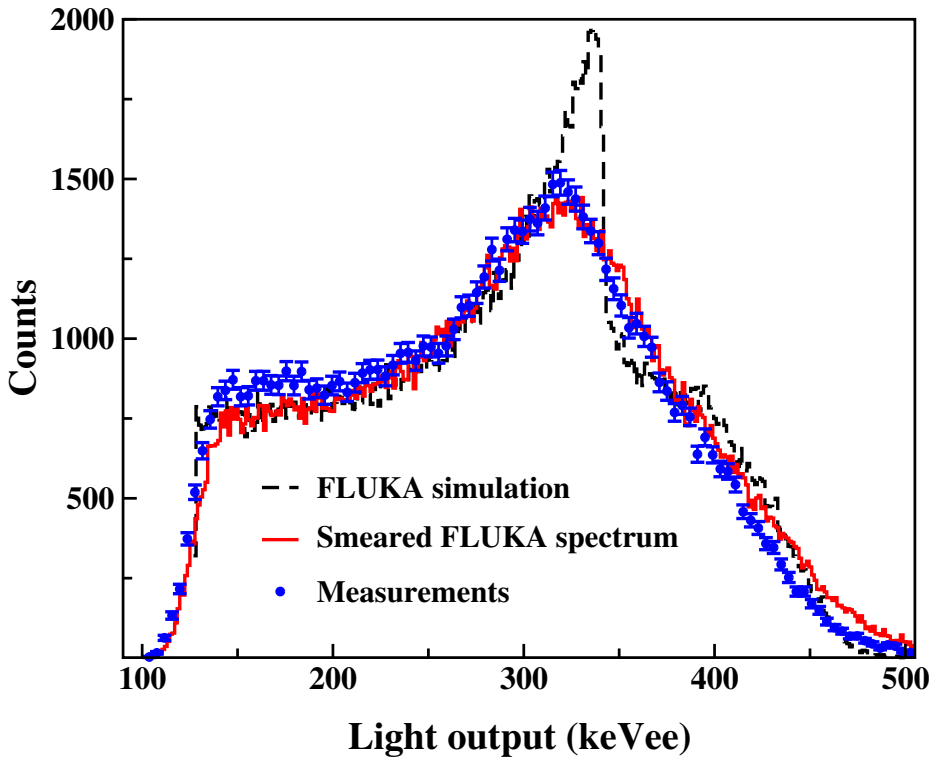

Figure 3.6: Pulse height distribution for 511 keV γ-rays measured (data points) and simulated (dashed curve) for a 5" $\times$ 5" BC501A organic scintillator detector. Solid curve corresponds to simulated spectrum after folding with detector resolution. The simulated spectrum is normalized to the area of experimental distribution.

to the interaction of 511 keV γ-rays in BC501A. The peak in the simulated spectrum indicates the Compton edge. The stark discrepancy between the spectra suggests that the simulated data needs to be smeared with random Gaussian noise that accounts for the resolution of the detector. The chi-square minimization procedure was applied to determine the values of light-dependent resolution parameters, as defined in Equation 3.8.

The best values of resolution parameters α, β, and γ that reproduce the experimental spectrum were obtained by minimizing χ^2, defined as

$$\chi^2 = \sum_i \frac{[N^{meas.}(L_i) - N^{MC}(L_i)]^2}{\sigma^2_{meas.}(L_i)} \tag{3.9}$$

where $N^{meas.}(L_i)$ is the light output corresponding to the i^{th} channel of the experimental spectrum, $N^{MC}(L_i)$ is the corresponding Monte Carlo spectrum

smeared with resolution parameters, and $\sigma^2_{meas.}(L_i)$ is the statistical error in the measurement. The minimization method yields values of $\alpha \approx 13 \pm 2.0\%$, $\beta \approx 9 \pm 1.5\%$ and relatively small value of $\gamma \approx 3 \pm 0.4\%$, the parameter corresponding to PMT noise. As shown in Figure 3.6 the shape of the simulated spectrum (solid line) after Gaussian smearing using these parameters agrees well with the measured spectrum.

3.4.3 Simulation of recoil proton response

The response of an organic liquid scintillator to charged particles can be expressed by the relation between the scintillation energy emitted per unit path length, $\frac{dL}{dx}$ and specific energy loss, $\frac{dE}{dx}$. In organic scintillators, a high ionization density due to specific energy loss along the track of the particle leads to quenching, a non-radiative decay of excited molecules [25]. As ionization density varies with particle type, the effect of quenching will be reflected as particle-dependent light output. Chau has formulated a relation, which is the modified form of Birks equation to express $\frac{dL}{dx}$ in terms of $\frac{dE}{dx}$ incorporating quenching [25–27]

$$\frac{dL}{dx} = \frac{S(\frac{dE}{dx})}{\left[1 + \ kB(\frac{dE}{dx}) + \ c(\frac{dE}{dx})^2\right]} \tag{3.10}$$

where S is the scintillation efficiency of the medium, the product kB and c are adjustable parameters to fit the experimental data.

The equation can be rewritten in the form $\frac{dL}{dE}$ which represents the fluorescent light emitted when a charged particle loses dE amount of energy in the detector volume as [28],

$$\frac{dL}{dE} = \frac{S}{\left[1 + \ kB(\frac{dE}{dx}) + \ c(\frac{dE}{dx})^2\right]} \tag{3.11}$$

For fast electron interactions, the specific energy loss is relatively low, and Equation 3.11 can be approximated to S ($\frac{dL}{dE} \approx$S); a linear dependence between light output and particle energy. To obtain the fluorescent light generated by energetic protons produced by fast neutron interaction, energy-dependent quench-

ing has to be incorporated in the simulation.

In the FLUKA simulation, energy-dependent quenching has been included to find the scintillation light produced by recoil protons. The geometrical details such as detector size, source to detector distance (175 cm) and physical characteristics of the detector, like material compositions, stoichiometry, and density were incorporated in the input of FLUKA. The properties of neutron beam with characteristics similar to those of a neutron source ^{252}Cf, were described in the user subroutine, 'source'. The beam emission was defined to be isotropic in the c.m. frame with Maxwellian energy distribution in the range 0-12 MeV defined according to Equation 3.2. The transformation Equations 5.30 and 3.5 were used to obtain the energy and angular distribution of fission neutrons in the laboratory frame. The total number of fission events was matched to the experimental value. The randomness in fission direction, neutron emission angle, and the probability distribution of neutron emission energy were also accounted for in the simulation. The fast neutron interaction was identified by recoil proton production in the active volume of the detector. The energy deposited by recoil protons and the energy of corresponding neutrons were scored event by event.

The parametric fit results reported by Craun and Smith [28] have been applied in Equation 3.11 for quenching. The light output thus obtained was expressed as electron equivalent energy in the units of keVee or MeVee. These equivalent energy spectra are further Gaussian smeared with resolution parameters (α, β and γ) to obtain realistic Monte Carlo spectra. Figure 3.7 displays the light output distribution generated by recoil protons for monoenergetic neutron interactions. In Figure 3.7(a), spectra corresponding to neutron beams of energies 3, 6, 8 and 10 MeV spanning the dynamic range of interest are shown. Figure 3.7(b) shows FLUKA simulated light output distribution compared with measured data for a quasi-monoenergetic neutron of 4±0.2 MeV. The simulation reproduces the measured data very well.

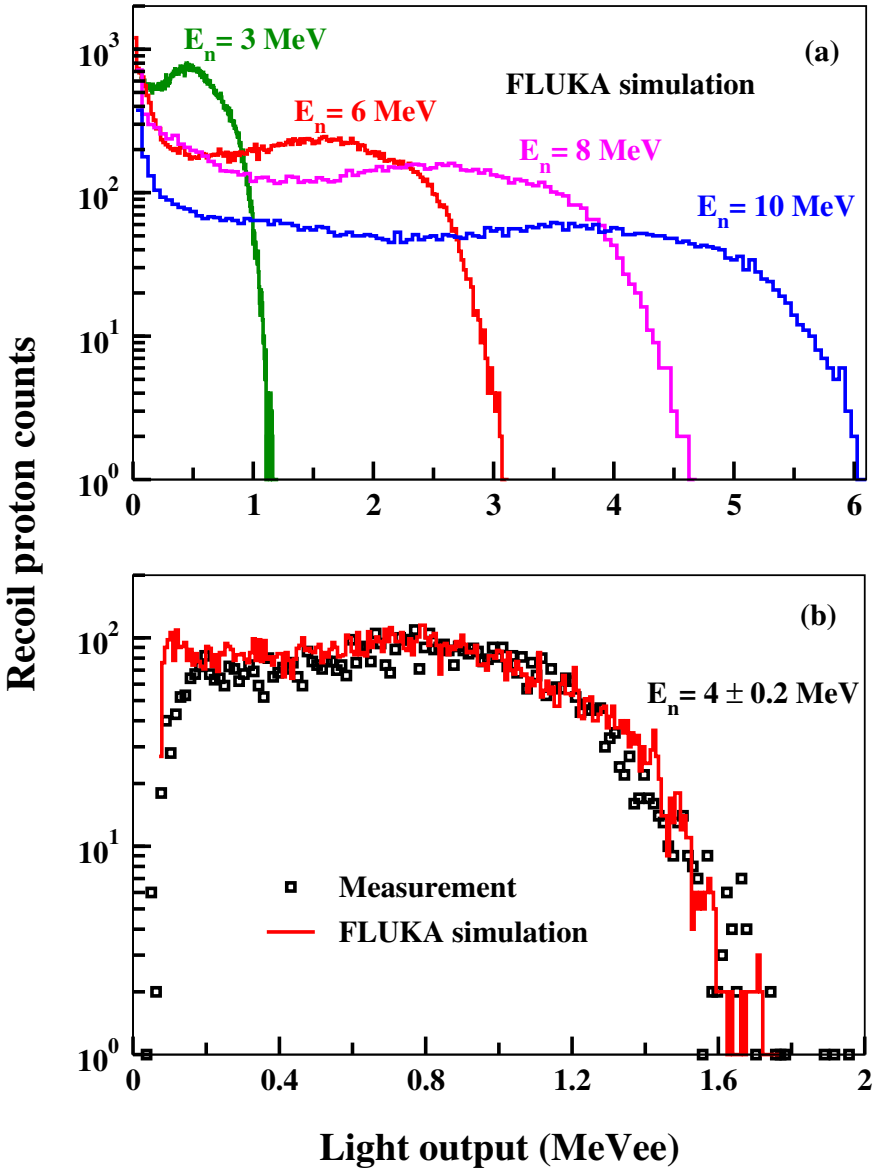

Figure 3.7: (a) simulated light output distribution corresponding to interactions of neutrons of energies 3, 6, 8 and 10 MeV incident on 5" × 5" BC501A. (b) comparison of the measured light output with FLUKA simulation results for quasi-monoenergetic neutrons of $E_n = 4.0 \pm 0.2$ MeV.

3.4.4 Intrinsic efficiency of 5" × 5" BC501A detectors

The intrinsic efficiency of a single BC501A cell was determined from the number of recoil protons that result in scintillation light output above the detection threshold, E_P^{th}. In the measurement, the energy threshold for neutron detection was set to be ≈0.5 MeV [29, 30]. The light output corresponding to neutron

interactions in the energy range ≈0.5 MeV - 10 MeV has been simulated using FLUKA, including energy-dependent quenching effects. From simulated data, the intrinsic efficiency as a function of neutron energy was estimated using the equation,

$$\frac{d\eta}{dE_n} = \Big(\frac{1}{F_N\ M_n\ \frac{d\Omega}{4\pi}}\Big)\Big(\frac{1}{f(E_n)}\ (\frac{dN_P}{dE_n})(E_n)\Big) \tag{3.12}$$

where F_N is the number of fissions, M_n is the average neutron multiplicity from ^{252}Cf fission, $d\Omega$ is the solid angle subtended by a single neutron detector, $(\frac{dN_P}{dE_n})(E_n)$ is the number of recoil protons produced above threshold energy by neutrons with energy between E_n and dE_n, and $f(E_n)$ is the probability distribution of neutrons from ^{252}Cf in the laboratory frame evaluated using Equations 3.2 and 3.5.

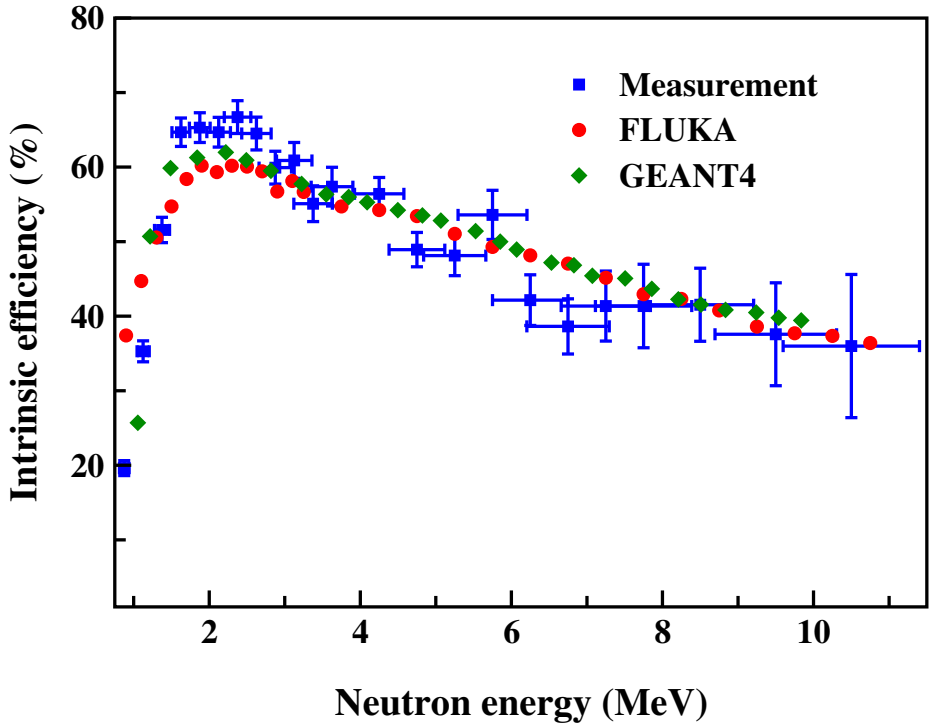

Figure 3.8: The intrinsic efficiency of 5" × 5" organic scintillator, BC501A as function of incident neutron energy. The experimental results are shown with error bars. Circle (red) and diamond (green) symbols represent FLUKA and GEANT4 simulation results [31] respectively.

Figure 3.8 shows intrinsic efficiency for a 5" × 5" BC501A liquid scintillator obtained from FLUKA simulation and measurements. The measured data points

are shown with statistical errors. The error in E_n indicates the uncertainty that emerged from the position of interaction in the liquid cell and the intrinsic time resolution of the detector. For comparison, the efficiency curve for a similar detector obtained from the GEANT4 [22] simulation at 0.5 MeV threshold [31] is also displayed in the figure. The FLUKA simulation reproduces measured efficiency data reasonably well in the dynamic range of interest and is in good agreement with the results of the GEANT4 simulation.

3.5 Scattering of neutrons by materials

In large detector arrays, one dominant factor that limits accurate estimation of neutron flux from a given reaction is the scattering of neutrons by various materials on their flight path. In the design phase of the NAND facility, careful consideration was given to minimizing the amount of scattering material. Nevertheless, physical structures such as the vacuum chamber wall, detector coverings, etc. are inevitable. These materials remain as sources of neutron interaction, causing neutron attenuation and scattering. NAND uses a spherical vacuum chamber made of 4 mm thick stainless steel (SS) wall as reaction chamber. Neutron interactions with the chamber wall can be a major source of attenuation and background in the detectors. In order to evaluate the effect of neutron scattering, FLUKA simulation has been performed to calculate the loss of direct neutron flux in a single cell and the subsequent generation of neutron background in neighbouring detectors. For comparison, simulations were carried out for two commonly used vacuum chamber materials, aluminium (Al) and stainless steel (SS) in the form of 4 mm thick sheets placed in the neutron beam path at 50 cm away from the source position.

The geometry defined in the simulation consists of three organic liquid scintillators placed at 175 cm distance from the source position and at 18° angular separation from each other, as displayed in Figure 3.3. A beam of neutrons with energy distribution defined according to Equation 3.2 and beam divergence

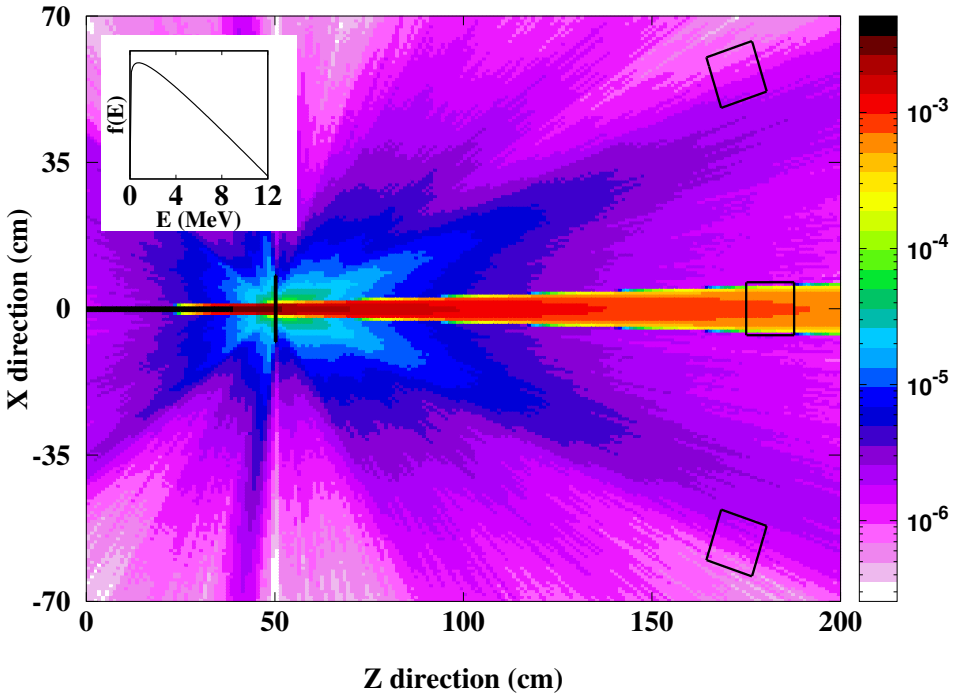

Figure 3.9: Spatial distribution of normalized neutron fluence (neutrons/ cm^2/primary weight) after scattering from 4 mm thick sample material (marked by vertical line) placed 50 cm away from source position. The three rectangular boxes represent neutron detector regions. The inset shows the energy distribution of incident neutrons as defined by Equation 3.2.

just sufficient to illuminate the cross-sectional area of the central detector was directed at the sample materials (Al or SS). Figure 3.9 shows the spatial distribution of normalized neutron fluence (neutrons/ cm^2/primary weight) obtained after interactions from the sample material placed 50 cm away from the source position. The energy distribution of the incident neutron is shown in the inset. The three rectangular boxes shown represent neutron detector regions. The detector structures are mounted at angles 0° and 18° w.r.t. beam direction with angular acceptance of $\approx \pm 2.0°$. The scattered beam into these regions was recorded.

The percentage of neutron flux incident directly (ϕ_{direct}) in the cross-sectional area of the neutron detector at 0° for the two materials (4 mm thick) is given in Table 3.2. The background flux ($\phi_{scattered}$) due to scattered neutrons in the

Table 3.2: Percentage of incident neutron flux (direct and scattered) on neighbouring detectors after interactions from 4mm thick material placed in neutron beam path. Two materials, Al and SS, are compared in the FLUKA calculation. The background due to neutron scattering from vacuum chamber material is lower than measured cross-talks events in the array [32].

Scattering material	ϕ_{direct} at 0° (%)	$\phi_{scattered}$ at 18° (%)	Cross-talk probability (%)
Aluminium	91.7	5.6×10^{-3}	$4.6\pm0.28\times10^{-2}$[32]
Stainless steel	88.1	3.8×10^{-2}	

detector mounted at 18° is also given. It is noticed that the loss of flux due to scattering ($\approx$ 8 %) and the associated neutron background are minimal for aluminium material as compared to stainless steel. The measured cross-talk probability, which is the probability to detect the same neutron in two or more neighbouring detectors after scattering [33], is given in the last column of Table 3.2. In the present configuration of neutron detectors in NAND array, the cross-talk probability between a pair of nearest detectors is found to be comparable to $\phi_{scattered}$ caused by the chamber wall made of stainless steel. It indicates that the choice of material for the chamber does not make a significant difference in terms of neutron background, as it is lower than the distortion caused by cross-talk in the array. Considering the mechanical aspects and ease of fabricating large-volume spherical chambers intended for high vacuum operations, stainless steel was chosen for the NAND target chamber.

3.6 Estimation of neutron emission flux

With accurate knowledge of the intrinsic efficiency of detectors, the flux loss due to scattering, and the solid angle subtended by the detectors (geometrical efficiency), the emission flux can be determined from the measured neutron counts. The efficiency curve derived from Equation 3.12, integrated over neutron energy range, yields the overall efficiency of a single detector. For ^{252}Cf source kept at

the centre of the NAND array,

$$\eta_{integral} = \Big(\frac{1}{F_N\ M_n\ \frac{d\Omega}{4\pi}}\Big) \int_{E_P^{th}}^{E_n^{max}} \frac{1}{f(E_n)}\ (\frac{dN_P}{dE_n})(E_n)\ dE_n \tag{3.13}$$

where E_n^{max} is the maximum neutron energy. One can define absolute efficiency of full detector array by incorporating the integral efficiency ($\eta_{integral}$), geometrical efficiency and scattering loss as,

$$\eta_{abs.} = (\phi_{incident})\ (\eta_{integral})\ (\frac{d\Omega}{4\pi})\ N_{BC501A} \tag{3.14}$$

where N_{BC501A} is the total number of BC501A detectors comprising the array.

The $\eta_{abs.}$ is an important parameter for multi-detector arrays aiming to study neutron multiplicity distribution Clarke, JINR. From the efficiency measurement performed for five neutron detectors, the average integral efficiency was found to be $\approx$ 48 % at $\approx$ 0.5 MeV threshold. Considering scattering from spherical vacuum chamber made of 4 mm thick stainless steel, the FLUKA simulation yields $\approx$ 12 % loss in neutron flux due to scattering. Taking into account all these contributions in Equation 3.14, the absolute efficiency of NAND array with 100 detectors is found to be $\approx$ 1.40 %. Slight deviations from this value can be expected according to the shape of the neutron evaporation spectrum (a function of nuclear temperature) and the resultant integral efficiency. In reaction studies where neutron distribution is important, the neutron flux emitted by the source can be obtained by normalizing measured neutron counts with the absolute efficiency of the array.

3.7 Summary and conclusions

We have investigated the light output response and intrinsic efficiency of the BC501A liquid scintillator of the NAND array using monoenergetic γ-ray sources and fast neutrons from ^{252}Cf fission source. Monte Carlo computation using

FLUKA reproduced the measured light output of the detector for γ-rays and neutrons after smearing the simulated data with detector resolution. The resolution parameters α, β, and γ have been derived for 5" $\times$ 5" BC501A detector with values of 0.13$\pm$0.020, 0.09$\pm$0.015, and 0.03$\pm$0.004 respectively.

The energy-dependent efficiency was calculated and compared with measured data at $\approx$0.5 MeV energy threshold. In the measurement, the fragments and coincident neutrons from the spontaneous fission of ^{252}Cf source were detected by using a 2π detector and BC501A respectively. The kinematics of neutron emission and particle-dependent quenching effects were incorporated in the FLUKA simulation. It was found that the FLUKA results are in good agreement with the measurement. It reproduces the measured efficiency curve reasonably well across the studied energy range. Also, good consistency has been observed between FLUKA and GEANT4 results.

Based on the calculation presented in this work, we conclude that the estimated neutron flux loss due to scattering from the NAND target chamber wall is $\approx$12 %. The background due to scattering is not found to be significant as compared to the cross-talk between the nearest pair of detectors in the array. Taking into account all these factors, the neutron detection efficiency of the full array is $\approx$1.40 % at 0.5 MeV threshold energy. After fine-tuning and evaluating its performance, the NAND array has been employed for heavy ion induced fission research. The following chapter describes the experimental aspects of fast neutron measurements in coincidence with fission.

Bibliography

[1] J. Valiente-Dobo'n, G. Jaworski, A. Goasduff, F. Egea, V. Modamio, T. Huyuk, A. Triossi, M. Jastrzab, P. Soderstrom, A. Di Nitto, G. de Angelis, G. de France, N. Erduran, A. Gadea, M. Moszynski, J. Nyberg, M. Palacz, R. Wadsworth, R. Aliaga, C. Aufranc, M. Bezard, G. Baulieu, E. Bissiato, A. Boujrad, I. Burrows, S. Carturan, P. Cocconi, G. Colucci, D. Conventi, M. Cordwell, S. Coudert, J. Deltoro, L. Ducroux, T. Dupasquier, S. Erturk, X. Fabian, V. Gonzalez, A. Grant, K. Hadynska-Klek, A. Illana, M. Jurado-Gomez, M. Kogimtzis, I. Lazarus, L. Legeard, J. Ljungvall, G. Pasqualato, R. Perez-Vidal, A. Raggio, D. Ralet, N. Redon, F. Saillant, B. Saygi, E. Sanchis, M. Scarcioffolo, M. Siciliano, D. Testov, O. Stezowski, M. Tripon, and I. Zanon, Nuclear Instruments and Methods in Physics Research Section A: Accelerators, Spectrometers, Detectors and Associated Equipment **927**, 81 (2019), `https://doi.org/10.1016/j.nima.2019.02.021`.

[2] A. Reiter, J.-O. Adler, I. Akkurt, J. Annand, F. Fasolo, K. Fissum, K. Hansen, L. Isaksson, M. Karlsson, M. Lundin, J. McGeorge, B. Nilsson, G. Rosner, B. Schroder, and A. Zanini, Nuclear Instruments and Methods in Physics Research Section A: Accelerators, Spectrometers, Detectors and Associated Equipment **565**, 753 (2006), `https://doi.org/10.1016/j.nima.2006.06.048`.

[3] I. Tilquin, Y. E. Masri, M. Parlog, P. Collon, M. Hadri, T. Keutgen, J. Lehmann, P. Leleux, P. Lipnik, A. Ninane, F. Hanappe, G. Bizard, D. Durand, P. Mosrin, J. Péter, R. Régimbart, and B. Tamain, Nuclear Instruments and Methods in Physics Research Section A: Accelerators, Spectrometers, Detectors and Associated Equipment **365**, 446 (1995), `https://doi.org/10.1016/0168-9002(95)00425-4`.

[4] M. Moszyński, G. Costa, G. Guillaume, B. Heusch, A. Huck, and

S. Mouatassim, Nuclear Instruments and Methods in Physics Research Section A: Accelerators, Spectrometers, Detectors and Associated Equipment **350**, 226 (1994).

[5] T. T. Böhlen, F. Cerutti, M. P. W. Chin, A. Fasso', A. Ferrari, P. G. Ortega, A. Mairani, P. R. Sala, G. Smirnov, and V. Vlachoudis, Nucl. Data Sheets **120**, 211 (2014).

[6] A. Ferrari, P. R. Sala, A. Fasso', and J. Ranft, CERN-2005-10(2005), INFN/TC_05/11, SLAC − R − 773 (2005).

[7] H. H. Barschall, L. Rosen, R. F. Taschek, and J. H. Williams, Rev. Mod. Phys. **24**, 1 (1952), 10.1103/RevModPhys.24.1.

[8] S. Croft, A. Favalli, and R. D. McElroy Jr., Nuclear Instruments and Methods in Physics Research Section A: Accelerators, Spectrometers, Detectors and Associated Equipment **954**, 161605 (2020), symposium on Radiation Measurements and Applications XVII, https://doi.org/10.1016/j.nima.2018.11.064.

[9] V. Weisskopf, Phys. Rev. **52**, 295 (1937), https://link.aps.org/doi/10.1103/PhysRev.52.295.

[10] K. Le Couteur and D. Lang, Nuclear Physics **13**, 32 (1959), https://doi.org/10.1016/0029-5582(59)90136-1.

[11] A. Borio di Tigliole, A. Cesana, R. Dolfini, A. Ferrari, G. Raselli, P. Sala, and M. Terrani, Nuclear Instruments and Methods in Physics Research Section A: Accelerators, Spectrometers, Detectors and Associated Equipment **469**, 347 (2001), https://doi.org/10.1016/S0168-9002(01)00777-X.

[12] G. Battistoni, S. Muraro, P. R. Sala, F. Cerutti, A. Ferrari, S. Roesler, A. Fasso, and J. Ranft, AIP Conf. Proc. **896**, 31 (2007), 10.1063/1.2720455.

[13] C. Budtz-Jorgensen and H.-H. Knitter, Nuclear Physics A **490**, 307 (1988), https://doi.org/10.1016/0375-9474(88)90508-8.

[14] A. Göök, F.-J. Hambsch, and M. Vidali, Phys. Rev. C **90**, 064611 (2014), https://link.aps.org/doi/10.1103/PhysRevC.90.064611.

[15] D. G. Madland and J. R. Nix, Nuclear Science and Engineering **81**, 213 (1982), https://doi.org/10.13182/NSE82-5.

[16] K. Nishio, Y. Nakagome, H. Yamamoto, and I. Kimura, Nuclear Physics A **632**, 540 (1998), https://doi.org/10.1016/S0375-9474(98)00008-6.

[17] U. Brosa, S. Grossmann, and A. Muller, Physics Reports **197**, 167 (1990), https://doi.org/10.1016/0370-1573(90)90114-H.

[18] J. C. D. Milton and J. S. Fraser, Phys. Rev. **111**, 877 (1958), https://link.aps.org/doi/10.1103/PhysRev.111.877.

[19] S. Venkataramanan, A. Gupta, K. S. Golda, H. Singh, R. Kumar, R. P. Singh, and R. K. Bhowmik, Nuclear Instruments and Methods in Physics Research Section A: Accelerators, Spectrometers, Detectors and Associated Equipment **596**, 248 (2008), https://doi.org/10.1016/j.nima.2008.07.156.

[20] R. Brun and F. Rademakers, Nuclear Instruments and Methods in Physics Research Section A: Accelerators, Spectrometers, Detectors and Associated Equipment **389**, 81 (1997), new Computing Techniques in Physics Research V, https://doi.org/10.1016/S0168-9002(97)00048-X.

[21] Flair : An advanced graphical user interface for particle simulation programs, https://flair.web.cern.ch/flair/download.html.

[22] S. Agostinelli, J. Allison, K. Amako, J. Apostolakis, H. Araujo, P. Arce, M. Asai, D. Axen, S. Banerjee, G. Barrand, F. Behner, L. Bellagamba, J. Boudreau, L. Broglia, A. Brunengo, H. Burkhardt, S. Chauvie, J. Chuma,

R. Chytracek, G. Cooperman, G. Cosmo, P. Degtyarenko, A. Dell'Acqua, G. Depaola, D. Dietrich, R. Enami, A. Feliciello, C. Ferguson, H. Fesefeldt, G. Folger, F. Foppiano, A. Forti, S. Garelli, S. Giani, R. Giannitrapani, D. Gibin, J. Gomez Cadenas, I. Gonzalez, G. Gracia Abril, G. Greeniaus, W. Greiner, V. Grichine, A. Grossheim, S. Guatelli, P. Gumplinger, R. Hamatsu, K. Hashimoto, H. Hasui, A. Heikkinen, A. Howard, V. Ivanchenko, A. Johnson, F. Jones, J. Kallenbach, N. Kanaya, M. Kawabata, Y. Kawabata, M. Kawaguti, S. Kelner, P. Kent, A. Kimura, T. Kodama, R. Kokoulin, M. Kossov, H. Kurashige, E. Lamanna, T. LampÃľn, V. Lara, V. Lefebure, F. Lei, M. Liendl, W. Lockman, F. Longo, S. Magni, M. Maire, E. Medernach, K. Minamimoto, P. Mora de Freitas, Y. Morita, K. Murakami, M. Nagamatu, R. Nartallo, P. Nieminen, T. Nishimura, K. Ohtsubo, M. Okamura, S. O'Neale, Y. Oohata, K. Paech, J. Perl, A. Pfeiffer, M. Pia, F. Ranjard, A. Rybin, S. Sadilov, E. Di Salvo, G. Santin, T. Sasaki, N. Savvas, Y. Sawada, S. Scherer, S. Sei, V. Sirotenko, D. Smith, N. Starkov, H. Stoecker, J. Sulkimo, M. Takahata, S. Tanaka, E. Tcherniaev, E. Safai Tehrani, M. Tropeano, P. Truscott, H. Uno, L. Urban, P. Urban, M. Verderi, A. Walkden, W. Wander, H. Weber, J. Wellisch, T. Wenaus, D. Williams, D. Wright, T. Yamada, H. Yoshida, and D. Zschiesche, Nuclear Instruments and Methods in Physics Research Section A: Accelerators, Spectrometers, Detectors and Associated Equipment **506**, 250 (2003), `https://doi.org/10.1016/S0168-9002(03)01368-8`.

[23] F. Arneodo, P. Benetti, A. Bettini, A. di Tigliole, E. Calligarich, C. Carpanese, F. Casagrande, D. Cavalli, F. Cavanna, P. Cennini, S. Centro, A. Cesana, C. Chen, Y. Chen, D. Cline, O. Consorte, I. Mitri, R. Dolfini, A. Ferrari, A. Berzolari, K. He, X. Huang, Z. Li, F. Lu, J. Ma, G. Mannocchi, C. Matthey, F. Mauri, L. Mazzone, C. Montanari, R. NardÃš, S. Otwinowski, S. Parlati, D. Pascoli, A. Pepato, L. Periale, G. Mortari, A. Piazzoli, P. Picchi, F. Pietropaolo, A. Rappoldi, G. Raselli, S. Resconi,

J. Revol, M. Rossella, C. Rossi, C. Rubbia, P. Sala, D. Scannicchio, F. Sergiampietri, S. Suzuki, M. Terrani, P. Torre, S. Ventura, M. Verdecchia, C. Vignoli, G. Xu, Z. Xu, H. Wang, J. Woo, C. Zhang, Q. Zhang, and S. Zheng, Nuclear Instruments and Methods in Physics Research Section A: Accelerators, Spectrometers, Detectors and Associated Equipment **418**, 285 (1998), https://doi.org/10.1016/S0168-9002(98)00679-2.

[24] G. Dietze and H. Klein, Nuclear Instruments and Methods in Physics Research **193**, 549 (1982), https://doi.org/10.1016/0029-554X(82)90249-X.

[25] J. B. Birks, *Theory and practice of scintillation counting* (Pergamon Press, Oxford 1964).

[26] C. N. Chou, Phys. Rev. **87**, 904 (1952), https://link.aps.org/doi/10.1103/PhysRev.87.904.

[27] G. F. Knoll, *Radiation Detection and Measurement* (John Wiley, New York 2010).

[28] R. Craun and D. Smith, Nuclear Instruments and Methods **80**, 239 (1970), https://doi.org/10.1016/0029-554X(70)90768-8.

[29] T. Masterson, Nuclear Instruments and Methods **88**, 61 (1970), https://doi.org/10.1016/0029-554X(70)90859-1.

[30] R. Cecil, B. Anderson, and R. Madey, Nuclear Instruments and Methods **161**, 439 (1979), https://doi.org/10.1016/0029-554X(79)90417-8.

[31] K. Banerjee, T. Ghosh, S. Kundu, T. Rana, C. Bhattacharya, J. Meena, G. Mukherjee, P. Mali, D. Gupta, S. Mukhopadhyay, D. Pandit, S. Banerjee, S. Bhattacharya, T. Bandyopadhyay, and S. Chatterjee, Nuclear Instruments and Methods in Physics Research Section A: Accelerators, Spec-

trometers, Detectors and Associated Equipment **608**, 440 (2009), https://doi.org/10.1016/j.nima.2009.07.034.

[32] N. Saneesh, K. Golda, A. Jhingan, S. Venkataramanan, T. Varughese, M. Kumar, M. Thakur, R. Mahajan, B. Behera, P. Sugathan, A. Chatterjee, and M. Chatterjee, Nuclear Instruments and Methods in Physics Research Section A: Accelerators, Spectrometers, Detectors and Associated Equipment **986**, 164754 (2021), https://doi.org/10.1016/j.nima.2020.164754.

[33] J. Wang, A. Galonsky, J. J. Kruse, P. D. Zecher, F. Deák, A. Horváth, A. Kiss, Z. Seres, K. Ieki, and Y. Iwata, Nuclear Instruments and Methods in Physics Research Section A: Accelerators, Spectrometers, Detectors and Associated Equipment **397**, 380 (1997), https://doi.org/10.1016/S0168-9002(97)00806-1.

Chapter 4

Measurement of mass distribution and neutron multiplicity in ^{227}Pa : Experimental aspects

Experimentally, various aspects of nuclear fission are investigated by measuring different fission observables. Some of the important observables used for investigating the heavy ion-induced fission process are the mass distribution of fragments, kinetic energy, mass angle correlation, angular distribution, light-charged particle multiplicities, neutron multiplicity, etc. These probes have been intensively used in the past few decades to study the nature of fission under various circumstances, such as compound nuclei (CN) at higher and lower excitation energies, various entrance channels, target deformation, etc. And these studies elucidate largely our understanding of induced nuclear fission processes. Nevertheless, these studies also show the possibility of overlap in the experimental observables. Overlap of observables or similar experimental observation but of different physics origin makes the fission studies more challenging.

The broadening of mass width observed in the mass distribution of fragments may have its roots in shell effects, non-compound fission processes such as quasi-fission, etc. [1, 2]. Similarly, higher particle multiplicities are interpreted in

terms of the dissipative nature of fission evolution, early re-separation of the fused system before full equilibration, etc. [3–5]. Hence, measuring one or two quantities may be inadequate to conclude the nature of fission comprehensively. This brings up the necessity of measuring multiple fission observables and their correlation simultaneously. The validity of conclusions based on one observable can be examined in the case of other observables. In the theoretical analysis, the need for simultaneous reproducibility of various measured quantities and their correlations will restrict the model parameters, which can give better insight into the physics origin or interpretation of the experimental observables. The National Array of Neutron Detectors (NAND) is one such facility that enables us to measure multiple observables of the same fission events efficiently [6]. The design, development and performance evaluation of NAND facility is described extensively in the Chapter 2. In the present scientific investigation, the NAND facility is used to find the influence of multi-chance fission, a phenomenon in which fission is preceded by neutron emission, in determining the fission modes at low and intermediate excitation energies.

Mass distribution is one of the most sensitive and extensively used experimental probes that gives direct information about the complex rearrangement of compound nuclear mass. If the neutrons are mostly emitted before the saddle point in the evolution towards fission, the average value of multi-chance fission (MCF) can be calculated simply from the pre-scission neutron multiplicity (ν_{pre}). Furthermore, the correlation between fragment mass and ν_{pre}, known as mass-gated pre-scission neutron multiplicity, can be utilized as a sensitive probe to study the role of MCF in determining distinct fission modes. With this motivation, we have measured the mass distribution, average ν_{pre} and the $Mass - \nu_{pre}$ correlation for a light actinide nucleus ^{227}Pa formed in the complete fusion reaction of ^{19}F+^{208}Pb in the E* range $\approx$ 30 - 60 MeV.

The experiment was performed using the 15 UD Pelletron accelerator facility at the Inter University Accelerator Centre (IUAC), New Delhi [7]. Pulsed beam

of ^{19}F at laboratory energies of 90 MeV, 95 MeV, 100 MeV, 105 MeV and 120 MeV was bombarded on isotopically enriched nuclear targets of ^{208}Pb. The compound nuclei formed in the heavy ion-induced fusion with excitation energy in the range $\approx$ 30 - 60 MeV undergo binary fission. The fission fragments were detected by using two large-area sensitive fission detectors. The NAND facility was used for the measurement of fast neutrons emitted in coincidence with the heavy ion-induced fission process. This chapter is dedicated to discussing experimental aspects of heavy ion-induced fission and is organized as follows: The accelerator facility at IUAC is described in the following sections. This is followed by a detailed discussion about various sub-systems of the NAND facility, such as the scattering chamber, analogue-based signal processing, and data acquisition in the subsequent sections.

4.1 Pelletron Accelerator at IUAC

The 15 UD Pelletron Accelerator facility at IUAC is a tandem electrostatic accelerator capable of delivering essentially all stable beams with energies depending on the charge state of the ion and the terminal voltage [7–9]. A schematic of the Pelletron accelerator is shown in Figure 4.1.

The accelerator is installed in a 5.5 metre-diametre, 26.6 metre-high cylindrical vessel. A Multi-Cathode Source of Negative Ion by Cesium Sputtering (MC-SNICS) situated at the top, as shown in the Figure 4.1 is used for producing the required beam species. The extracted negative ion beam from the ion source is accelerated through General Purpose (GP) tubes to a few hundred kilo electron volts (keV) energies. The pre-accelerated beam is then injected into the vertically configured accelerator through a bending magnet. The magnetic rigidity of the bending magnet is selected such that only particles of a given m/q will follow the trajectory to the accelerator tank. Hence, injector magnet is also called mass selector. Due to the high positive potential, as high as 15 MV, built at the terminal, the negative ions experience a strong electrostatic force of

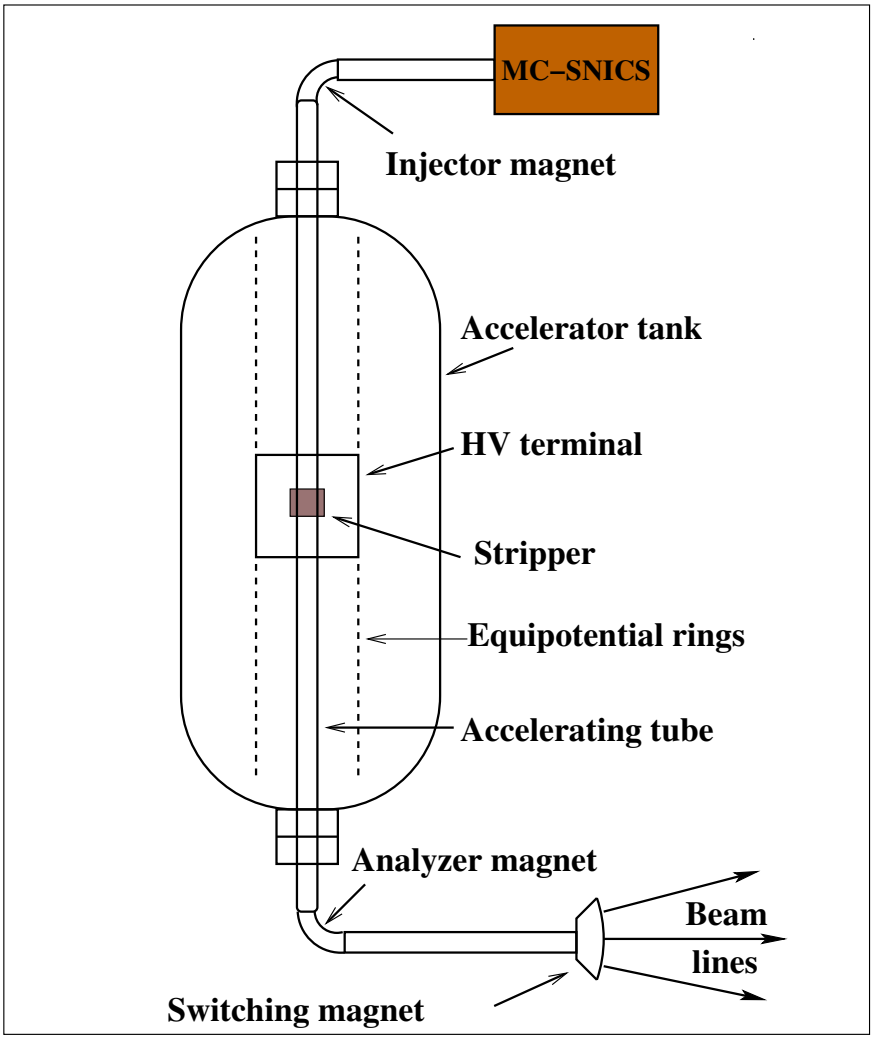

Figure 4.1: A schematic of the Pelletron accelerator facility at IUAC.

attraction and gain energy. On reaching the terminal, the beam passes through a stripper made of a small volume of gas or thin foil, which removes several electrons, thereby converting them into positive ions. These ions are accelerated further to ground potential at the tank bottom due to electrostatic repulsion. The total energy gain (E_{total}) from the dual acceleration is given by,

$$E_{total} = E_{ini} + (q+1)V_{term} \tag{4.1}$$

where q is the charge state of the ion, E_{ini} is the energy gained from the pre-acceleration and V_{term} is the terminal potential.

A second bending magnet, known as energy analyzer magnet, positioned at the bottom of the accelerator tank, is used for selecting the beam of required energy. Due to the statistical nature of electron stripping at the terminal, the beam species can have a distribution of charge states varying from $q = 1$ to Z, where Z is the atomic number. The energy of the ion beam is selected by adjusting the magnetic field of the analyzer magnet $B = 797.55 \times \sqrt{m\ E_{total}/\ q^2}$ where E_{total} is the energy in MeV, m is the mass in u, and B is given in Gauss. In addition to the dc (continuous) beam, the accelerator is capable of delivering pulsed beam with a repetition rate of 250 ns - 2μs with the help of a multi-harmonic buncher. In the present experiment, pulsed beam with a repetition rate of 250 ns in the laboratory energy range of 90 MeV to 120 MeV was used. After energy selection, a switcher magnet was used to switch the accelerated beam to the NAND facility installed in the beam hall-II of the IUAC.

4.2 Target details

For mass distribution measurements, the thickness of nuclear targets is desired to be a few hundreds of $\mu g/cm^2$ or less to minimize the energy loss of fragments inside the target material. Due to energy loss in a material medium, fragments travel at velocities lower than their emission velocities, which affects the mass spectrum derived from the velocities of complementary fragments. For the present study, ^{208}Pb targets of thickness $\approx$ 250 μg/cm^2 were prepared by thermal evaporation. Due to the difficulties in preparing self-supporting ^{208}Pb, it was deposited on carbon backing of thickness $\approx$ 20 μg/cm^2. The general principles of nuclear target fabrication and details of deposition facilities are given in the reference [10].

4.3 Measurement techniques

The principle followed in deriving the mass distribution of fission fragments is based on the conservation of linear momentum. In the energy range of $4 - 7$ MeV/u, where fission is binary in nature, momentum conservation yields,

$$M_1 V_1 = M_2 V_2 \tag{4.2}$$

$$\sqrt{2M_1 E_1} = \sqrt{2M_2 E_2} \tag{4.3}$$

where $M_{1,2}$, $V_{1,2}$ and $E_{1,2}$ denote the mass, velocity and energy of the respective fragments. Thus, the mass ratio ($M_R = \frac{M_2}{M_1+M_2}$) can be calculated directly from the velocities or energy of both fragments of a given fission event as,

$$M_R = \frac{V_1}{V_1 + V_2} = \frac{E_1}{E_1 + E_2} \tag{4.4}$$

In the present experiment, we have used a pair of large-area (20 cm $\times$ 10 cm) multi-wire proportional counters for fission fragment detection. These fast timing detectors provide an accurate time of flight (TOF) of complementary fragments in the laboratory frame [11]. From the TOF information, fragment velocities and the mass distribution can be derived according to equation 4.4

The method used for extracting neutron multiplicity, which is the number of neutrons emitted per fission, is based on a global fit to the experimental neutron energy spectra at different angles by minimizing the χ^2. In the evolution of a fully equilibrated compound nucleus towards fission, neutrons can be emitted at various stages, such as the transition from equilibrium configuration to saddle point (pre-saddle neutrons), the descent from saddle to scission (saddle-to-scission neutrons), scission to pre-acceleration of fragments (near-scission neutrons), and from fully accelerated fragments (post-scission neutrons). Though it is difficult to separate various neutron groups from measured neutron spectra experimentally, the kinematic correlation between fragments and neutrons can be investigated

to find the neutrons emitted prior to fission, known as pre-scission neutrons, and those emitted by fully accelerated fragments, known as post-scission neutrons. The term pre-scission neutrons includes pre-saddle neutrons, saddle-to-scission neutrons, and near-scission neutrons, as they pose similar kinematic correlations with the neutron sources. The number of neutrons detected in any given detector will have contributions from fast-moving fragments and slow-moving compound nuclei according to their relative angles w.r.t the neutron detector. This feature is exploited through numerical methods to find neutron multiplicities.

4.4 Experimental setup

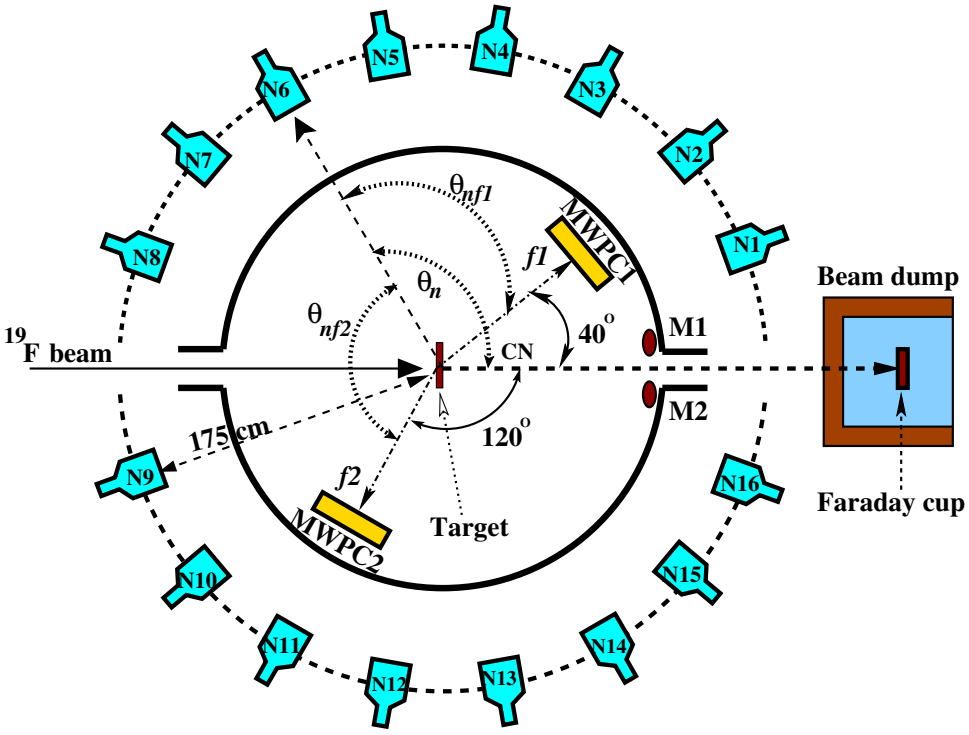

Figure 4.2: Schematic view of the experiment setup used for measuring neutron multiplicity in coincidence with fission. θ_n, θ_{nf1}, and θ_{nf2} represent relative angles between various neutron sources [compound nucleus (CN), fragments $f1$ and $f2$] and neutron detectors. Neutron detectors (N1 to N16 of NAND array) in the reaction plane alone are displayed (see text for details).

A schematic of the experimental setup used for measuring the mass distribution, average neutron multiplicity, and their correlations is shown in Figure 4.2.

High efficiency liquid cells from the NAND facility were used for detecting the fast neutron emitted in coincidence with fission at various angles [6, 12]. The design, development, characterization, and installation of these detector systems are explained in great detail in chapters 2 and 3.

4.4.1 Fission detectors : MWPC

One of the MWPC detectors was mounted left side to the beam direction in forward angle 40° at a distance of 27 cm from the target. To detect the complementary fragment, a second MWPC was mounted at folding angle of 160° w.r.t. the first detector. This corresponds to an angle of 120° for the second detector w.r.t beam direction. In order to improve the coincidence rate of complementary fragments, the back-angle detector was placed relatively close to the target at a distance of 23 cm. The gas detectors were operated with a continuous flow of isobutane gas (99.5 % purity) maintained at 4 mbar pressure. A bias voltage of -440 V was applied to the central timing electrode, keeping the position electrodes at ground potential.

Figure 4.3 shows the inside view of the scattering chamber. A schematic of the gas handling unit used for MWPC operation is also shown in Figure 4.3. During pumping and venting of the vacuum chamber, MWPC detectors were kept at the same pressure as the target chamber via a bypass valve to protect the entrance widow foil of MWPCs made of 0.9 μm mylar foil. After attaining the required vacuum in the target chamber, typically 5×10^{-6} mbar or better, the gas detectors were disconnected from the chamber by closing the bypass valve. This is followed by the circulation of isobutane gas at 4 mbar pressure, which is regulated by a needle valve in the gas input and a rotary pump at the gas exit line. An electro-pneumatic shut-off valve connected to the gas inlet is used to protect the MWPC detectors from vacuum accidents. In case of power failure, the immediate closure of the shut-off valve stops further flow of isobutane gas into the detector volume, thus preventing any damage to the window foil of the

MWPC.

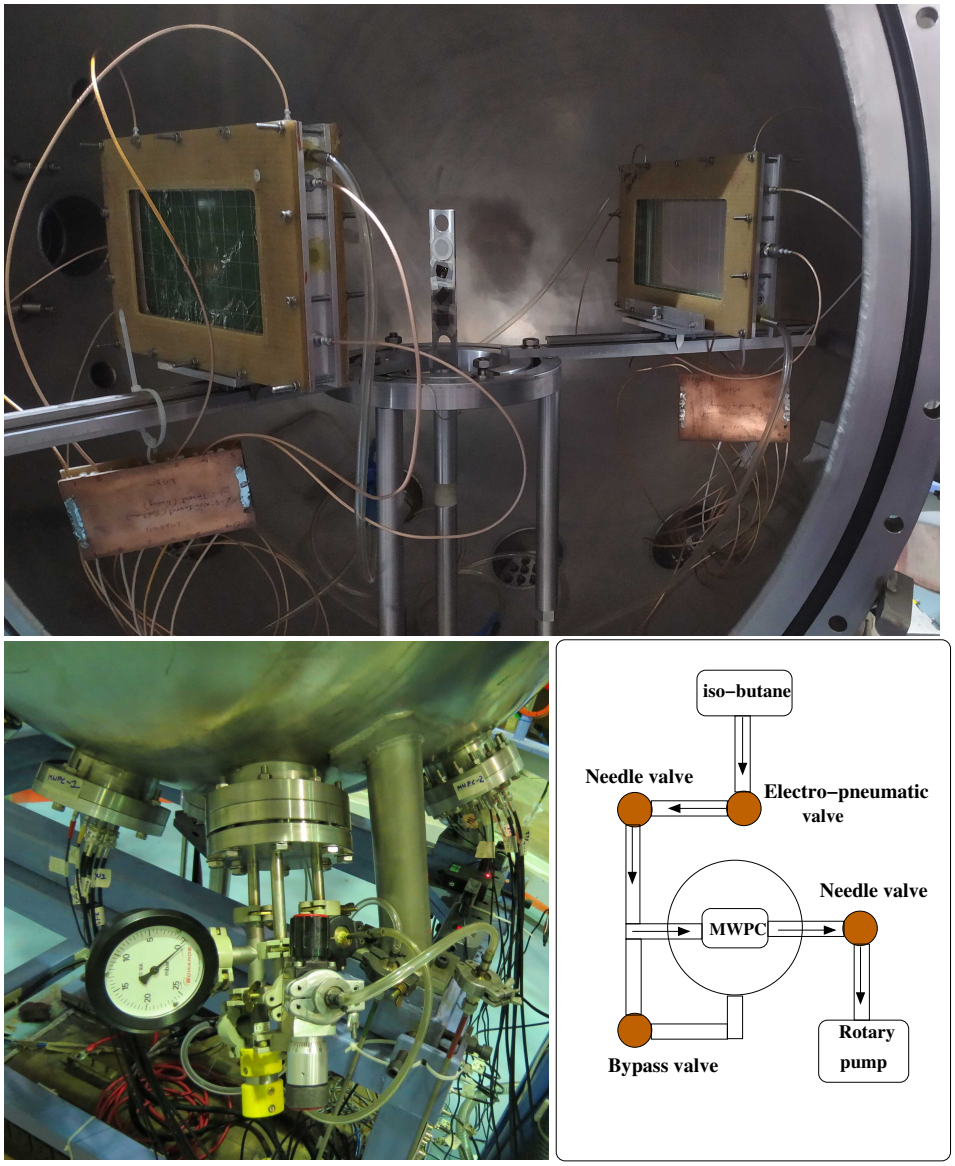

Figure 4.3: (top) Inside view of the scattering chamber, which accommodates the targets, detectors, and the preamplifiers. (bottom) A photograph, and schematic diagram of the gas handling unit used for circulating isobutane gas in the MWPC detectors.

4.4.2 Neutron detectors : BC501A

Fast neutrons emitted in the fission process were detected using BC501A detectors in coincidence with the fragments. Each BC501A detector consists of a 5 inch diameter and 5 inch depth (5" × 5") liquid cell coupled to a 5" diameter

Table 4.1: The relative angles θ_n, θ_{nf1}, and θ_{nf2} of BC501A detectors N1 - N16, used in the present experiment. see the Figure 4.2 for details.

Detector	θ_n (deg.)	θ_{nf1} (deg.)	θ_{nf2} (deg.)	Detector	θ_n (deg.)	θ_{nf1} (deg.)	θ_{nf2} (deg.)
N1	18	22	138	N9	162	122	78
N2	36	4	156	N10	162	158	42
N3	54	14	174	N11	144	176	24
N4	72	32	168	N12	126	166	6
N5	90	50	150	N13	108	148	12
N6	108	68	132	N14	90	130	30
N7	126	86	114	N15	72	112	48
N8	144	104	96	N16	18	58	102

photomultiplier tube (PMT), model *Hamamatsu R4144*. These liquid scintillators are mounted on the geodesic dome structure of the NAND facility, providing a 175 cm flight path for fast neutrons. Figure 4.2 shows the neutron detectors of the reaction plane alone, which are labelled as N1 to N16. The relative angles of these detectors w.r.t beam (CN), fission fragment 1 ($f1$) and fragment 2 ($f2$) are listed in Table 4.1. To minimize the secondary radiation background due to the interaction of the beam on the tantalum sheet mounted at the end of the beam line, a beam dump made of borated paraffin and lead is installed 4.5 m downstream from the target.

The light output among the scintillators for a given energy radiation varies due to differences in the gain of PMT. To ensure uniform light output response from all detectors used, the bias voltages of all neutron detectors were optimized to achieve similar light output for known gamma rays from radioactive sources such as ^{22}Na, ^{137}Cs, and ^{60}Co. Typically, the bias voltages vary in the range $\approx$ - 1500 V to - 1800 V. Two Passivated Ion Implanted Planar Silicon (PIPS) detectors of thickness 300 μm, labelled as M1 and M2 in the Figure 4.2, were mounted at $\approx 12^{\circ}$ on either sides w.r.t beam direction. These detectors were used for continuous monitoring of the beam.

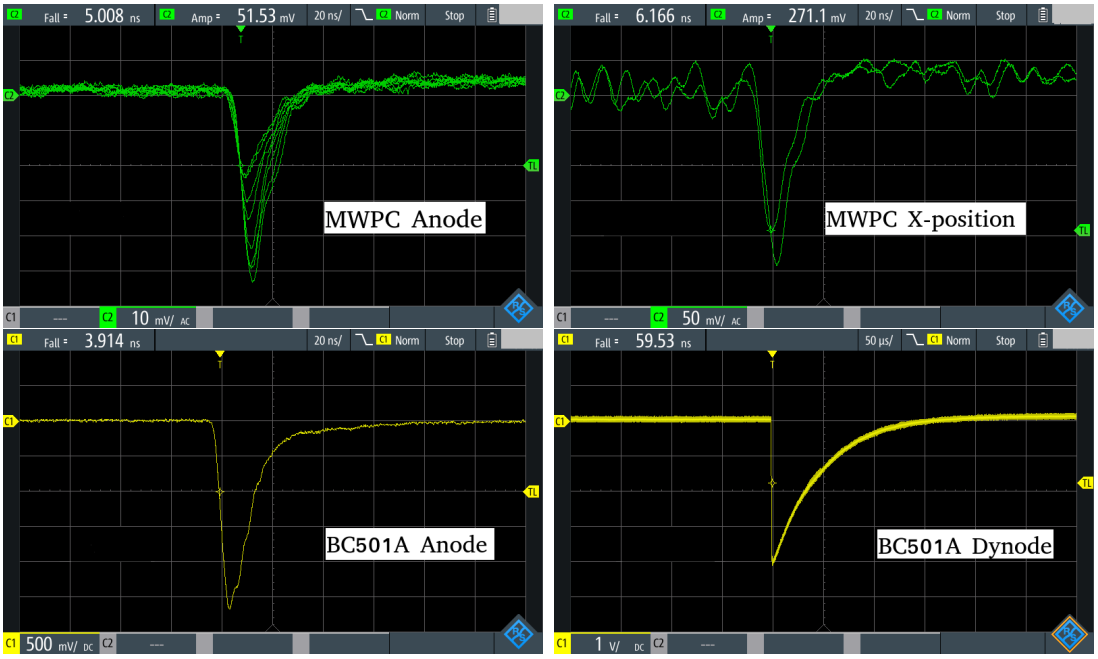

Figure 4.4: (top) Timing and X-position signals derived from one of the MWPC detectors. (bottom) Timing and light output signals extracted from the photomultiplier tube of a BC501A detector.

Figure 4.4 displays the raw signals obtained from one of the MWPC detectors and a BC501A detector. The timing signal extracted from the anode of MWPC, and one of the position signals processed through a fast timing amplifier are shown in the top panels. The bottom panels show the timing and light output signals derived from a BC501A detector. The timing signal was obtained from the last dynode (anode) of the PMT whereas the light output pulse was derived from one of the intermediate dynodes, which is later processed through a charge-sensitive preamplifier.

4.5 Signal processing electronics and data acquisition

The electronics used for analog signal processing are primarily intended to derive the interaction position and time of flight (TOF) of complementary fission fragments as well as the TOF of associated neutrons. Signal processing and data

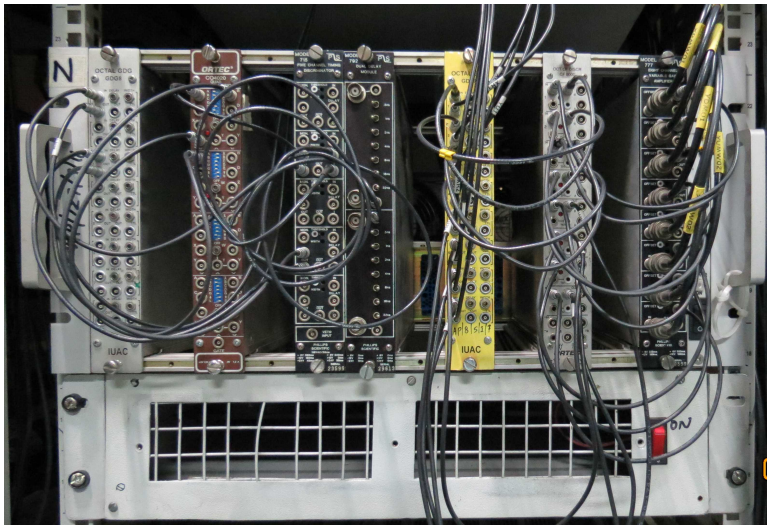

Figure 4.5: Signal processing electronics for fission detectors.

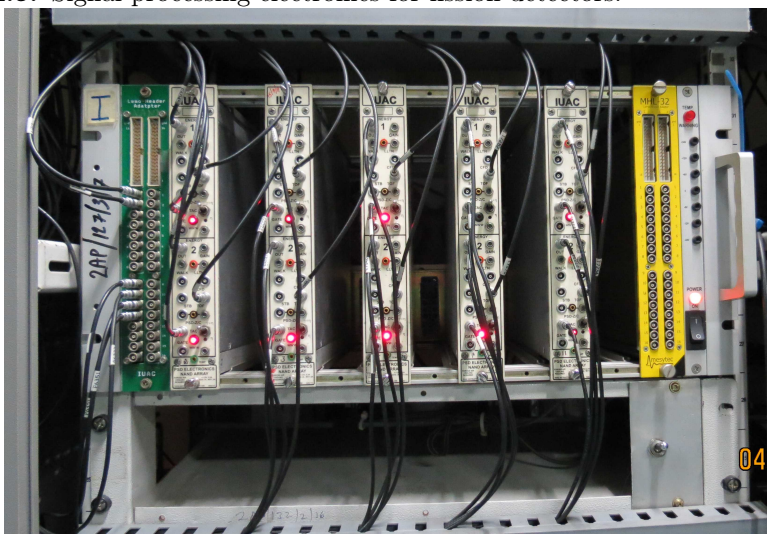

Figure 4.6: Signal processing electronics for neutron detectors.

collection systems are composed of three distinct sections: (i) signal processing electronics for fission detectors; (ii) electronics for neutron detectors; and (iii) VME-based data acquisition. The data acquisition trigger was derived from a coincidence between the radio-frequency (RF) signal of the pulsed beam and fission detectors. Figures 4.5 and 4.6 show various electronic modules used for processing the signals from fission and neutron detectors.

A block diagram of the electronics setup used for processing the signals from MWPC and neutron detectors for coincidence measurements is shown in the

Figure 4.7. Each MWPC detector provides five signals: a timing signal and four position signals (XL, XR, YU, and YD). All the signals were preamplified using indigenously developed vacuum-compatible timing preamplifiers. The timing signal, derived from the avalanche electrode, shows sufficient amplitude after the pre-amplifier for further processing. But the signals derived from position electrodes need to be amplified. The position signals were processed through fast amplifiers (*Phillips Scientific, model 777*) and Constant Fraction Discriminators (CFD) (*EG&G Ortec, model CF-8000*) for time pick-off. The threshold voltage for all CFD modules was kept relatively low, ≈ 30 mV, well above the noise level, to ensure maximum detection efficiency.

The timing signals from MWPCs in coincidence with the RF signal of the beam pulse were used for setting the data acquisition trigger logic, which is shown in the Figure 4.8. In the first step, the timing signals from MWPC detectors were processed through a CFD (*Phillips Scientific, model 715*) and fed to a logic OR unit (*Ortec, model CO-4020*). The OR module gives a NIM signal at the output if any one of the MWPCs is triggered by charged particle radiations. The OR output was stretched for ≈ 200 ns, known as the coincidence window. The RF signal processed through the CFD (*Phillips Scientific, model 715*) module was properly delayed to fall within the coincidence window (see Figure 4.8). These signals (OR output and RF) were given to a logic AND unit (*Ortec, model CO-4020*). The output of the logic AND unit implies a coincidence between the RF of pulsed beam and the MWPC signal. The intrinsic spread in the RF was ≈ 1.3 ns. The RF signal, in coincidence with MWPC signals, was used as the *trigger* for the TOF measurements. Indigeneously developed VME crate control module receives the coincidence signal from the logic AND unit and generates acquisition strobes for the ADC (*CAEN, v785*) and TDC (*CAEN, v775*) modules for data collection [13]. An in-house developed root-based data acquisition software, NiasMARS, is used for collecting data in list-mode/ event-mode [14].

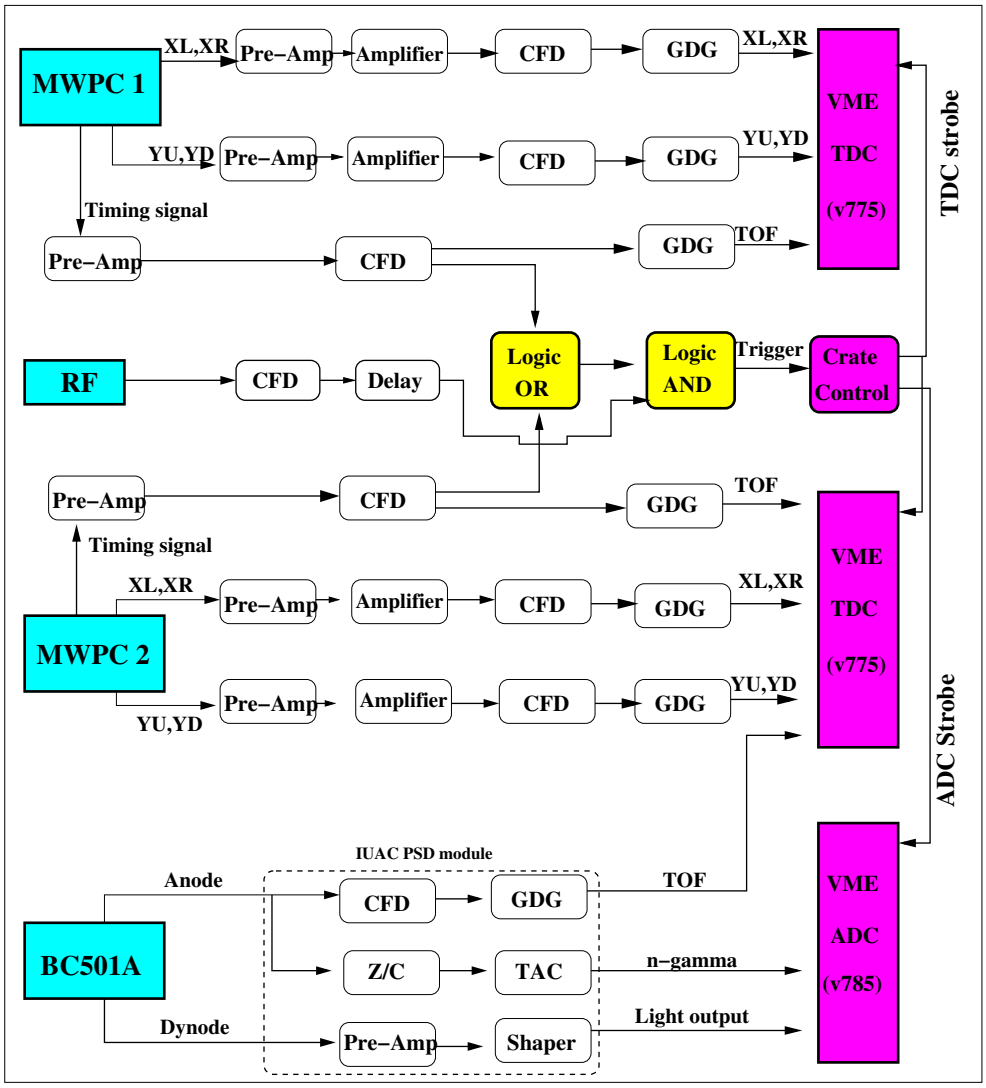

Figure 4.7: A block diagram of electronics used for the analog signal processing and data acquisition to measure the mass distribution and neutron multiplicities.

Figure 4.9 shows the position and TOF signals of MWPC detectors. Figures 4.9(a) and (b) are the TOF spectra obtained from MWPCs mounted at forward and backward angles, respectively. A clear separation of fission fragments from scattered beams can be observed in these plots. In the Figures 4.9(c) and (d), the interaction positions X ($X = X_L - X_R$) and Y ($Y = Y_U - Y_D$) of fission fragments are displayed. These difference-spectra span around 3200 channels in X and 1600 channels in Y. The distributions in the position spectra are proportional to the end-to-end delay (160 ns and 80 ns in X and Y, respectively) of the delay chips

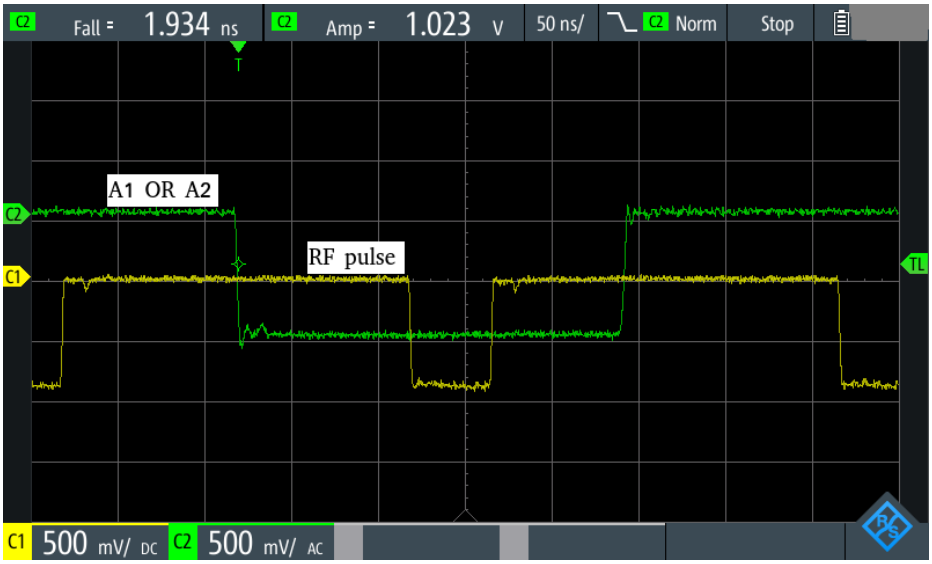

Figure 4.8: Figure shows a typical coincidence condition applied for binary fission measurements. The green pulse represents a LOGIC OR of timing signals from MWPCs. RF of the beam pulse, shown in yellow line, is delayed to coincide with MWPC signal.

used in the X and Y electrodes.

Neutron detector signals were processed using custom-built pulse shape discrimination modules [15]. Figure 4.7 shows the block diagram for signal processing of one of the neutron detectors used in the present study. The dynode signal from PMT is routed through a charge-sensitive preamplifier and fed to a uni-polar shaping amplifier. This output represents the total light output, which was used to set the energy threshold for each neutron detector. The detection threshold was set to obtain ≈ 0.5 MeV neutron energy. The anode signal was split into two. One branch was processed through a zero-cross (Z/C) over circuit for neutron gamma ($n - gamma$) discrimination, and the other branch was routed through a CFD for time pick-off. The prompt CFD signals, derived from all neutron and fission detectors, were delayed properly w.r.t the *trigger* by means of Gate and Delay Generator (GDG) modules to confine them within the TDC range of 400 ns. The NIM output from GDG was converted to an ECL signal using a NIM-ECL converter module, and fed to the TDC module as $STOP$ signal for time of flight measurements. The $START$ was provided by the

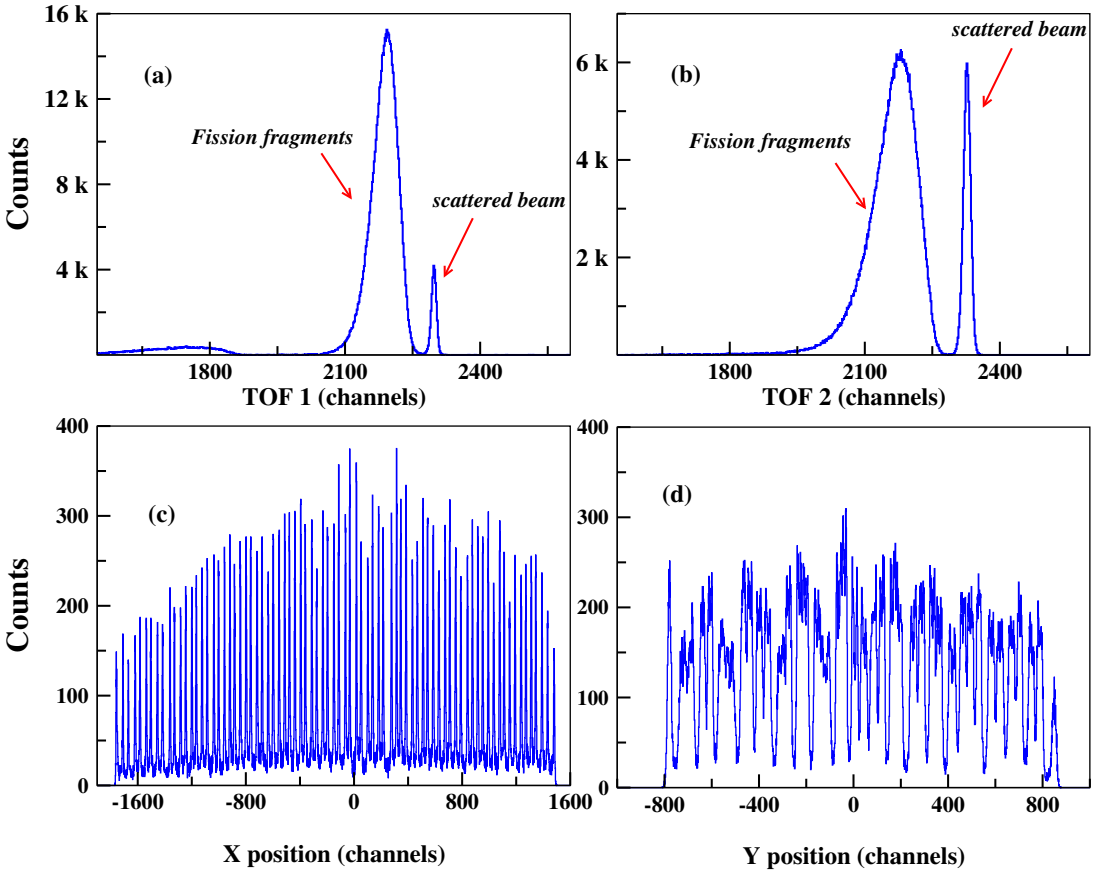

Figure 4.9: Histograms representing various signals of the MWPC detectors. (a) and (b) are the TOF spectra of the front and back-angle MWPC respectively, measured w.r.t the coincidence pulse. (c) The horizontal position spectrum obtained by $X = X_L - X_R$. Similarly, (d) represents the vertical position spectrum obtained by $Y = Y_U - Y_D$.

coincidence logic described.

Figures 4.10 (a)-(c) show the spectra of acquired signals from one of the neutron detectors. Figure 4.10(a) shows the TOF spectrum measured in the *Common Stop* mode of data acquisition. Neutron gamma discrimination obtained through pulse analysis is shown in 4.10(b). Figure 4.10(c) represents a typical light output spectrum generated by neutron and gamma interactions in the liquid cell. Spectra similar to 4.10 (a)-(c) are obtained from all other neutron detectors used. Figure 4.10(d) is obtained by plotting TOF against the zero-cross over spectrum. It shows excellent discrimination of neutrons from γ-ray backgrounds. This 2D spectrum will be used further for gating neutron

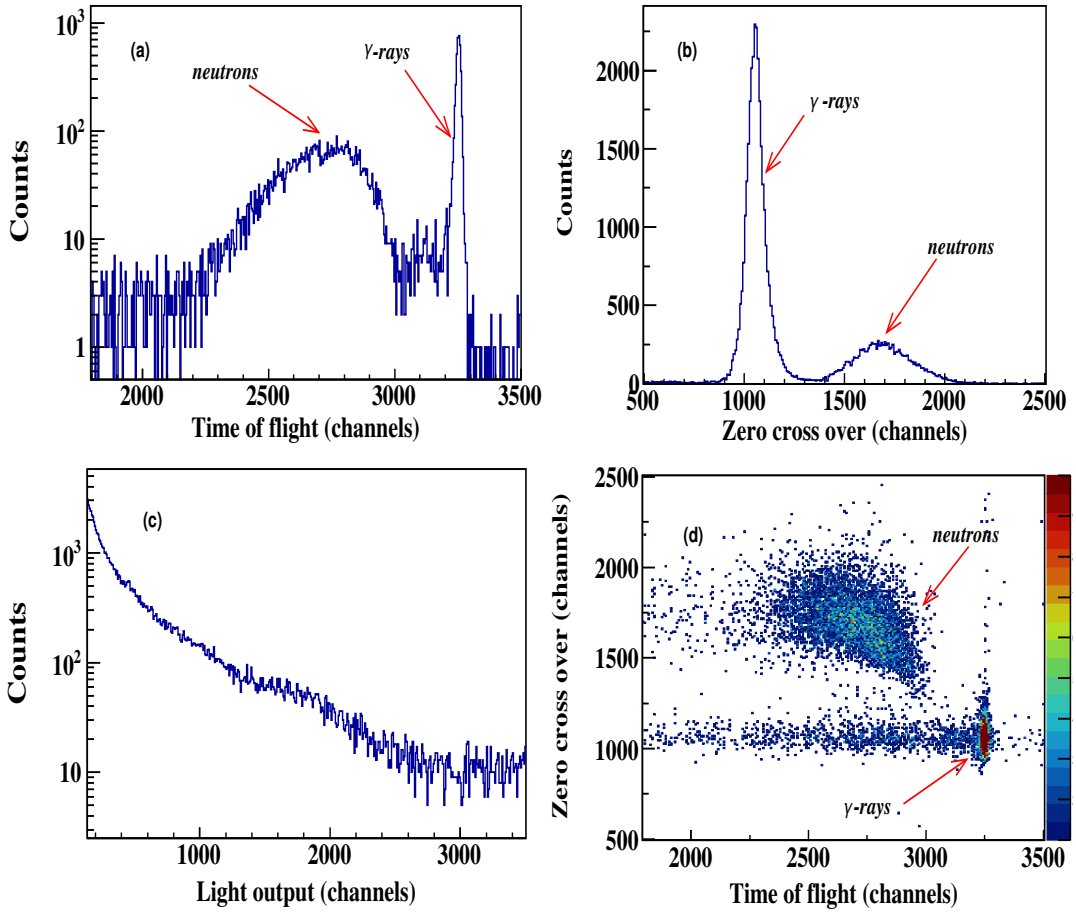

Figure 4.10: Histograms represent various signals acquired from a BC501A detector. (a) The TOF spectrum of neutrons and γ-rays measured w.r.t the coincidence pulse. (b) is the $n-\gamma$ discrimination spectrum obtained by the zero-cross over method. (c) The light output spectrum generated by combined neutron and γ-ray interactions in the liquid cell. (d) A two-dimensional histogram obtained by plotting the spectra in (b) against (a).

events in the data analysis. The data analysis methods adopted for extracting the average neutron multiplicity, fission fragment mass distribution, as well as the correlation of fragment mass with pre-scission neutron multiplicity are described in the coming chapter.

Bibliography

[1] R. Dubey, P. Sugathan, A. Jhingan, G. Kaur, I. Mukul, G. Mohanto, D. Siwal, N. Saneesh, T. Banerjee, M. Thakur, R. Mahajan, N. Kumar, and M. Chatterjee, Physics Letters B **752**, 338 (2016), https://doi.org/10.1016/j.physletb.2015.11.060.

[2] K. Banerjee, T. K. Ghosh, S. Bhattacharya, C. Bhattacharya, S. Kundu, T. K. Rana, G. Mukherjee, J. K. Meena, J. Sadhukhan, S. Pal, P. Bhattacharya, K. S. Golda, P. Sugathan, and R. P. Singh, Phys. Rev. C **83**, 024605 (2011), https://link.aps.org/doi/10.1103/PhysRevC.83.024605.

[3] M. Shareef, E. Prasad, A. Jhingan, N. Saneesh, K. S. Golda, A. M. Vinodkumar, M. Kumar, A. Shamlath, P. V. Laveen, A. C. Visakh, M. M. Hosamani, S. K. Duggi, P. S. Devi, G. N. Jyothi, A. Tejaswi, P. N. Patil, J. Sadhukhan, P. Sugathan, A. Chatterjee, and S. Pal, Phys. Rev. C **99**, 024618 (2019), 10.1103/PhysRevC.99.024618.

[4] M. Thakur, B. R. Behera, R. Mahajan, G. Kaur, P. Sharma, K. Kapoor, K. Rani, P. Sugathan, A. Jhingan, N. Saneesh, R. Dubey, A. Yadav, A. Chatterjee, M. B. Chatterjee, N. Kumar, S. Mandal, S. K. Duggi, A. Saxena, S. Kailas, and S. Pal, Phys. Rev. C **98**, 014606 (2018), DOI: 10.1103/PhysRevC.98.014606.

[5] D. J. Hinde, R. J. Charity, G. S. Foote, J. R. Leigh, J. O. Newton, S. Ogaza, and A. Chatterjee, Phys. Rev. Lett. **52**, 986 (1984), https://link.aps.org/doi/10.1103/PhysRevLett.52.986.

[6] N. Saneesh, K. Golda, A. Jhingan, S. Venkataramanan, T. Varughese, M. Kumar, M. Thakur, R. Mahajan, B. Behera, P. Sugathan, A. Chatterjee, and M. Chatterjee, Nuclear Instruments and Methods in Physics Research Section A: Accelerators, Spectrometers, Detectors and Associated

Equipment **986**, 164754 (2021), https://doi.org/10.1016/j.nima.2020.164754.

[7] G. K. Mehta and A. P. Patro, Nuclear Instruments and Methods in Physics Research Section A: Accelerators, Spectrometers, Detectors and Associated Equipment **268**, 334 (1988), https://doi.org/10.1016/0168-9002(88)90530-X.

[8] S. Ghosh, R. Mehta, G. K. Chowdhury, A. Rai, P. Patra, B. K. Sahu, A. Pandey, D. S. Mathuria, J. Chacko, A. Chowdhury, S. Kar, S. Babu, M. Kumar, S. S. K. Sonti, K. K. Mistry, J. Zacharias, P. N. Prakash, T. S. Datta, A. Mandal, D. Kanjilal, and A. Roy, Phys. Rev. ST Accel. Beams **12**, 040101 (2009), 10.1103/PhysRevSTAB.12.040101.

[9] Inter-University Accelerator Centre, https://www.iuac.res.in.

[10] T. Banerjee, S. Abhilash, D. Kabiraj, S. Ojha, G. Umapathy, M. Shareef, P. Laveen, H. Duggal, R. Amarnadh, J. Gehlot, S. Nath, and D. Mehta, Vacuum **144**, 190 (2017), https://doi.org/10.1016/j.vacuum.2017.07.022.

[11] A. Jhingan, N. Saneesh, M. Kumar, R. Mahajan, M. Thakur, G. Kaur, K. Kapoor, N. Kumar, M. Shareef, R. Dubey, S. Appannababu, E. Prasad, H. Singh, K. S. Golda, R. Ahuja, B. R. Behera, and P. Sugathan, Review of Scientific Instruments **92**, 033309 (2021), https://doi.org/10.1063/5.0029603.

[12] N. Saneesh, D. Arora, A. Chatterjee, K. Golda, M. Kumar, A. Vinodkumar, and P. Sugathan, Nuclear Instruments and Methods in Physics Research Section A: Accelerators, Spectrometers, Detectors and Associated Equipment **1013**, 165682 (2021), https://doi.org/10.1016/j.nima.2021.165682.

[13] M. Jain, E. T. Subramaniam, and S. Chatterjee, Review of Scientific Instruments **94**, 013304 (2023), https://doi.org/10.1063/5.0107168.

[14] Nxt gen. Instrumentation and Acquisition Systems, http://www.iuac.res.in/NIAS.

[15] S. Venkataramanan, A. Gupta, K. S. Golda, H. Singh, R. Kumar, R. P. Singh, and R. K. Bhowmik, Nuclear Instruments and Methods in Physics Research Section A: Accelerators, Spectrometers, Detectors and Associated Equipment **596**, 248 (2008), https://doi.org/10.1016/j.nima.2008.07.156.

Chapter 5

Data analysis methods

The binary fission data was analyzed using the ROOT-based analysis framework [1]. The analysis is primarily intended to extract the mass distribution of fission fragments, average neutron multiplicity, and the correlation of mass distribution with pre-scission neutron multiplicities at different excitation energies. These quantities were derived from the measured time of flight (TOF) data of fission fragments and neutrons. As known, the measured data will be an admixture of the time of flight of various particles. For instance, the TOF spectra measured using MWPC detectors have contributions from scattered beams, target recoils, etc., along with fission fragments. Similarly, BC501A detectors give TOF of neutrons in the γ-ray background. Therefore, proper discrimination of neutrons and fission fragments from unwanted radiation background is important. This is achieved in offline analysis by applying stringent coincidence conditions such as angular coincidence, full momentum transfer, etc. The gated events were analyzed by applying appropriate equations to extract the physical quantities of interest. In this chapter, we discuss the mathematical formulation of different methods adopted for finding the mass distribution and neutron multiplicities from time of flight measurements.

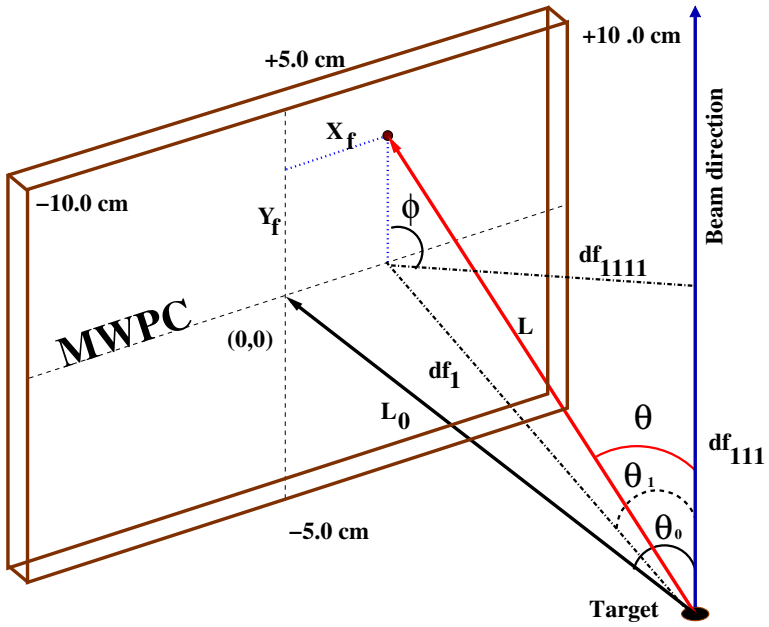

Figure 5.1: A schematic of co-ordinates (θ,ϕ) of the hit position of one of the fragments with respect to the beam direction. The black line arrow points to the co-ordinates (θ_0,ϕ_0) of detector centre. And the red arrow shows to co-ordinates (θ_i,ϕ_i) of a given fission event i.

5.1 Data analysis to find mass distribution and TKE of fission fragments

There are two methods commonly used for finding the mass distribution of binary fragments produced in a fusion-fission reactions. In the first method, known as the velocity reconstruction method or kinematic coincidence method, the absolute velocity of fission fragments was determined using the time of flight technique [2, 3]. The mass ratio of the fragments is derived from the ratios of their velocities in the centre of mass frame. This method solely relies on the measurement of the absolute time of flight of fission fragments using either a START-STOP detector set up or a pulsed beam. In situations where these facilities are not available or applicable, the absolute time of flight fragments cannot be determined. In such cases, the mass distribution of fragments is extracted from the time difference between their flight times to the fission detectors mounted at known distances. This method is known as the time of flight difference method. For the present

thesis work, the absolute time of flight of fission fragments was measured with the help of a pulsed beam. The mass ratio distribution was derived by the velocity reconstruction method. A detailed mathematical formulation of the method is described in the following section.

In this method, the velocity vectors of the binary fission events are reproduced by the accurate measurement of interaction position and TOF. The following calibration equations are used for converting the TDC channel numbers to absolute position.

Let x_1 and x_2 be the channel numbers of the two edges of the position spectrum. And y_1 and y_2 be the corresponding absolute values of positions (-10.0 cm and +10.0 cm as displayed in the Figure 5.1). Then,

$$y_1 = mx_1 + c \tag{5.1}$$

$$y_2 = mx_2 + c \tag{5.2}$$

where m and c are the slope and intercept respectively. By rearranging this, the following equations can be obtained for m and c as,

$$m = \frac{(y_1 - y_2)}{(x_1 - x_2)} \tag{5.3}$$

$$c = \frac{(x_1 y_2 - x_2 y_1)}{(x_1 - x_2)} \tag{5.4}$$

In the Figure 5.1, the coordinates of the hit position of one of the fragments are schematically shown. Knowing the distance to the centre of the detector L_0 and (θ_0, ϕ_0) of the detector centre, the precise interaction position (θ, ϕ) and path length L traversed by the fragments can be calculated from the following trigonometric relations:

$$L = \sqrt{df_1^2 + Y_f^2} \qquad where,\ df_1 = \sqrt{L_0^2 + X_f^2} \tag{5.5}$$

$$\theta_1 = \theta_0 - \tan^{-1}(\frac{X_f}{L_0}) \tag{5.6}$$

$$\theta = \cos^{-1}(\frac{df_{111}}{L}) \qquad where,\ df_{111} = df_1\ \cos(\theta_1) \tag{5.7}$$

$$\phi = \phi_0 + \tan^{-1}(\frac{Y_f}{df_{1111}}) \qquad where,\ df_{1111} = df_1\ \sin(\theta_1) \tag{5.8}$$

where X_f and Y_f are the calibrated positions derived from the MWPC signals. All the notations used are followed by the Figure 5.1. Similarly, the angular coordinates (θ, ϕ) and path length L for the complementary fragments can be determined from the other MWPC signals. To obtain the absolute time of flight of fragments, the TOF spectrum has been calibrated:

$$TOF(ns) = m\ TOF(ch.) + C \tag{5.9}$$

where m and C are the slope and intercept respectively. The TDC slope was measured using a time calibrator (*Ortec Time Calibrator, model 462*), which generates logic signals at precise time intervals. To estimate C, the TOF peak of elastically scattered beam has been used, whose energy at a given angle is known from calculations [4]. C was obtained by matching the peak of the scattered beam to the calculated TOF.

5.1.1 Velocity reconstruction method

The laboratory velocities of fragments (v_1, v_2) were determined from path length L and the calibrated TOF data. Figure 5.2 shows the vector diagram of fission fragment velocities in horizontal and vertical planes. Given that the two velocity vectors and the beam axis are co-planar, the measured velocity vectors can be decomposed into parallel and perpendicular components w.r.t. the beam axis, as shown in 5.2(a). These components are labelled as $w_1 = v_1 \cos(\theta_1)$ and $u_1 = v_1 \sin(\theta_1)$. V_1 and V_2 are the velocities of fragments in centre of mass frame. v_{par} represents the parallel component of velocity induced by the beam. In the case of full momentum transferred (FMT) events, v_{par} matches with the compound nuclear velocity $v_{cn} = 1.388\ (\sqrt{\frac{E_P}{A_P}})\ (\frac{A_P}{A_{CN}})$ where A_P and A_{CN} are the masses of

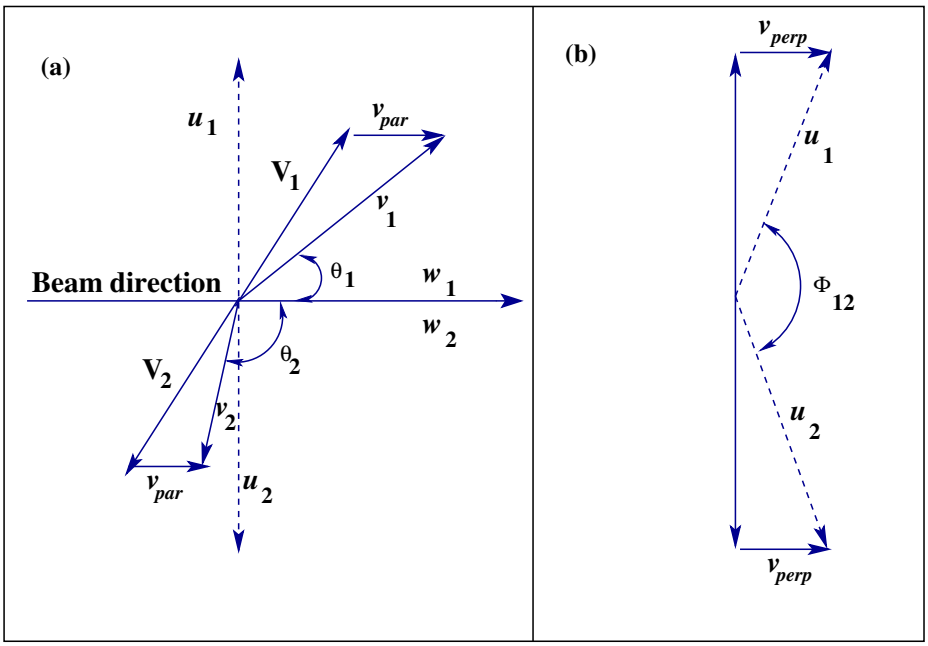

Figure 5.2: Velocity vector diagram of fission fragments in the laboratory and centre of mass frames. (a) shows the velocity vectors and their components in the plane of beam axis and (b) in the plane perpendicular to beam axis [2].

the projectile and compound nucleus, and E_P is the energy of the projectile.

From the Figure 5.2(a), we can write,

$$w_1 - v_{par} = V_1 \cos\theta_{cm1} \tag{5.10}$$

$$w_1 - v_{par} = (\frac{u_1}{\sin\theta_{cm1}}) \cos\theta_{cm1}; \quad where, \ [V_1 = \frac{u_1}{\sin(\theta_{cm1})}] \tag{5.11}$$

Similarly,

$$w_2 - v_{par} = -(\frac{u_2}{\sin(\theta_{cm1})}) \cos(\theta_{cm1}) \tag{5.12}$$

$$\frac{w_1 - v_{par}}{w_2 - v_{par}} = -(\frac{u_1}{u_2}) \tag{5.13}$$

Rearranging this, we get,

$$v_{par} = (\frac{u_1 w_2 + u_2 w_1}{u_1 + u_2}) \tag{5.14}$$

Similarly, from Figure 5.2 we get,

$$(x_1 + x_2)^2 = u_1^2 + u_2^2 - 2u_1u_2\cos(\phi_{12}); \quad where,\ \phi_{12} = \phi_1 + \phi_2 \tag{5.15}$$

By substituting the values of $x_1^2 = u_1^2 - v_{perp}^2$and $x_2 = u_2^2 - v_{perp}^2$, this equation can be simplified to,

$$v_{perp} = \frac{u_1u_2\sin(\phi_{12})}{\sqrt{u_1^2 + u_2^2 - 2u_1u_2\cos(\phi_{12})}} \tag{5.16}$$

For fission followed by full momentum transfer, $v_{par} - v_{cn}$ and v_{perp} are expected to be centered around zero. FMT events can thus be differentiated by applying a velocity filter around $v_{par} - v_{cn}$, $v_{perp} = (0,\ 0)$. Velocity vectors satisfying this criteria have been considered for FMT fission studies. The centre of mass velocities of the fragments were calculated using the equations,

$$V_1 = \sqrt{u_1^2 + v_{par}^2 - 2u_1v_{par}\cos(\theta_1)} \tag{5.17}$$

$$V_2 = \sqrt{u_2^2 + v_{par}^2 - 2u_2v_{par}\cos(\theta_2)} \tag{5.18}$$

If M_1 and M_2 are the corresponding masses of fragments, then momentum conservation yields,

$$M_1V_1 = M_2V_2 \tag{5.19}$$

This gives,

$$M_R = \frac{M_1}{M_1 + M_2} = \frac{V_2}{V_1 + V_2} \tag{5.20}$$

Thus the mass ratio M_R of fragments can be obtained from the ratio of centre of mass velocities. The total kinetic energy, TKE of the fragments were calculated as,

$$TKE = \frac{1}{2}(M_1V_1^2 + M_2V_2^2) \tag{5.21}$$

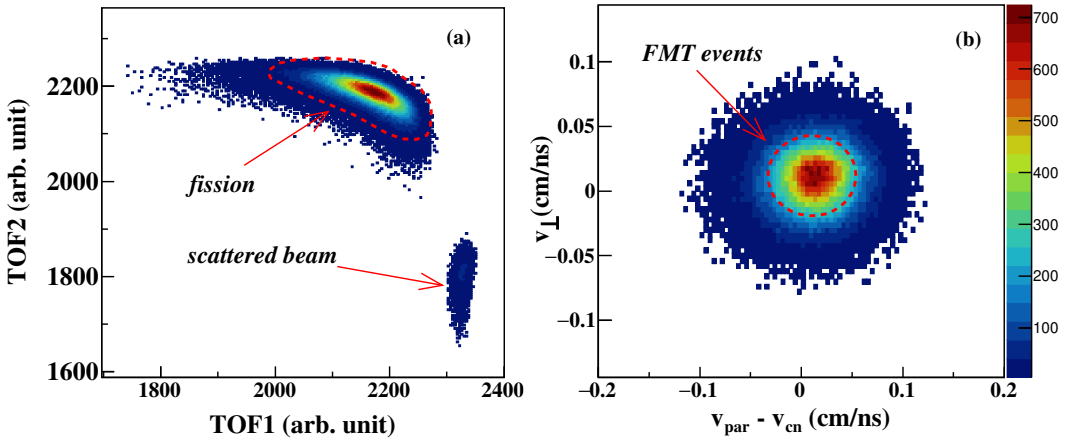

Figure 5.3: (a) Time of flight correlation of complementary events recorded using two MWPC detectors for ^{19}F+^{208}Pb reaction at 105 MeV beam energy. Events corresponding to fission fragments and scattered beam particles are indicated using arrows.(b) correlation of velocity components along the parallel and perpendicular directions with respect to the beam axis. FMT events are marked in red circle.

Figure 5.3 summarizes various coincidence conditions applied to filter the FMT events from other processes. In Figure 5.3(a) the time correlation of events detected in MWPC1 and MWPC2 is shown. Fission fragments were separated from other charged particles, such as scattered projectiles, target recoils, etc., by TOF and folding angle coincidence. Fission events are selected for analysis of fragment mass and kinetic energy distributions by applying a graphical cut around the most intensive region, as shown in Figure 5.3(a). The calibrated X, Y position information and TOF of complementary fragments have been used to find the velocity vectors of the two fragments, as described earlier. The projections of these velocity vectors to the parallel (v_{par}) and perpendicular (v_{perp}) planes with respect to the beam direction are shown in the Figure 5.3(b). A software cut around the centroid, fixed at the values (v_{perp}, v_{par} - v_{cn} = 0, where v_{cn} is the compound-nucleus velocity) was applied to select FMT events. These selected events were further analyzed to determine the velocities of the fragments (V_1, V_2) in the centre of mass frame. From V_1 and V_2, the mass ratio distribution and TKE of the fragments have been extracted using the Equations 5.20 and 5.21 respectively.

5.1.2 Energy loss correction

When a fission fragment passes through material medium such as target, entrance foil of the detectors, etc. it loses energy as predicted by the Bethe formula,

$$-\frac{dE}{dx} = \frac{4\pi n Z^2}{m_e v^2}\left(\frac{e^2}{4\pi\epsilon_0}\right)^2 \ln\left(\frac{2m_e v^2}{I}\right) \tag{5.22}$$

where Z and v are atomic number and velocity of the charged particle, n is the electron density of the material, e and m_e are the charge and mass of electrons, and I is the mean excitation energy [5, 6]. The measured velocity or energy will the residual of its original value. Fission fragment mass derived from these measured velocities must be corrected for energy loss in various media traversed by the particle.

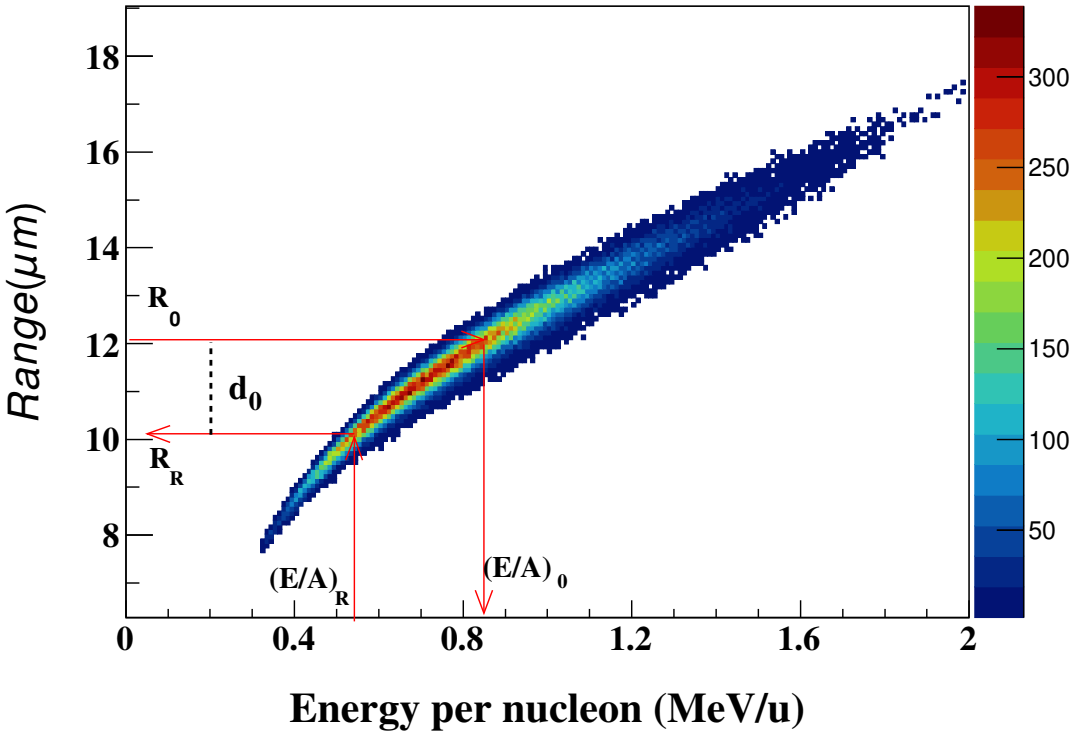

Figure 5.4: *Energy per nucleon* versus *range* relationship of fragments from the fission of ^{227}Pa at ≈46 MeV excitation energy.

The energy loss correction was applied in a simplified way by utilizing the "Energy per nucleon (E/A) - Range" relationship of charged particle in matter.

Range of the particle can be approximated by,

$$R(E) = \int_0^E (\frac{dE}{dx})^{-1}\, dE \tag{5.23}$$

The picture 5.4 depicts a typical *E/A - Range* plot obtained for fragments in the fission of ^{227}Pa at $\approx$ 46 MeV excitation energy. The measured energy per nucleon, denoted as $(E/A)_R$ and the corresponding range R_R are shown with red line. The picture also depicts the initial energy $(E/A)_0$ and the associated range R_0. When the particle of energy $(E/A)_0$ passes through a material of effective thickness d_0, the range decreases to R_R such that $R_R = R_0 - d_0$. So, from the *E/A - Range* correlation, as shown in the figure, the expected range in the absence of material medium and the corresponding energy $(E/A)_0$ can be reconstructed, knowing the $(E/A)_R$ and d_0. In a pioneering work, Northcliffe and Shilling calculated the *E/A - Range* table for heavy ions ($1 \leq Z \leq 103$) in various material media in the energy range $0.0125 \leq E/A \leq 12$ MeV/u [7]. In the current study, a C++ code that integrates these calculations was utilized to apply energy loss correction to the velocities of fission fragments in event-by-event mode [8]. The program calculates the initial energy E_0 from the mass (A), kinetic energy (E) and nuclear charge (Z) of the fragment. In the calculation, the extracted values of A and E, as described in the previous section, are used. The nuclear charge of the fragment was estimated by applying the concept of unchanged charge density (UCD) where $(A/Z)_{CN} = (A/Z)_{FF1} = (A/Z)_{FF2}$.

5.2 Analysis methods to find average neutron multiplicity

In the evolution of a fully equilibrated compound nucleus towards fission, neutrons can be emitted at various stages. Primarily, pre-scission neutrons and post-scission neutrons are separated from the total by exploring their kinematic

relationship with neutron sources. The overall effect of source velocity is the kinematic focusing of emitted particles along source direction and energy change based on emission angle. This effect has been visualized using a Monte Carlo calculation using FLUKA code which simulated the angular distribution of neutrons evaporated by moving sources [9, 10]. Figure 5.5 displays the two dimensional spatial distribution of neutrons in the plane of beam axis, emitted by two moving sources. Figure 5.5(a) and (b) are respectively the spatial distribution of neutrons emitted by a compound nucleus and fission fragment (FF). The simulation takes into account typical values of mass and kinetic energy of moving sources. Though the neutrons are emitted isotropically in the rest frame of sources, their distribution in the laboratory frame are substantially modified. The figure clearly demonstrate the influence of source velocity on the angular distribution of neutrons. Particles emitted by the slow moving CN are nearly isotropic in laboratory frame too. Whereas in the case of fast moving FF, the distribution is highly focused on the source direction.

The changes in the kinetic energy of emitted neutrons due to source velocity are shown in the Figure 5.6. In the c.m. frame, the FLUKA parameters are defined to yield identical neutron energy spectra. Figure 5.6(a) shows the energy spectra obtained in the lab. frame at two relative angles $\theta_{ns} = 0°$ and $90°$. The neutron source is a slow moving CN. When comparing the $90°$ detector w.r.t the $0°$ detector, a slight decrease in neutron yield and a change in the energy spectrum towards lower energy may be observed. The results of similar calculation for fast moving fragments are shown in 5.6(b). The neutron spectra calculated at the same relative angles $\theta_{ns} = 0°$ and $90°$ depicts the magnitude of kinematic effects on spectral distribution with increase in source velocity. These kinematic correlations between neutrons and their sources are utilized to determine the number of neutrons emitted by CN or fission fragments from the sum spectra.

The method used to extract neutron multiplicity, which is the number of

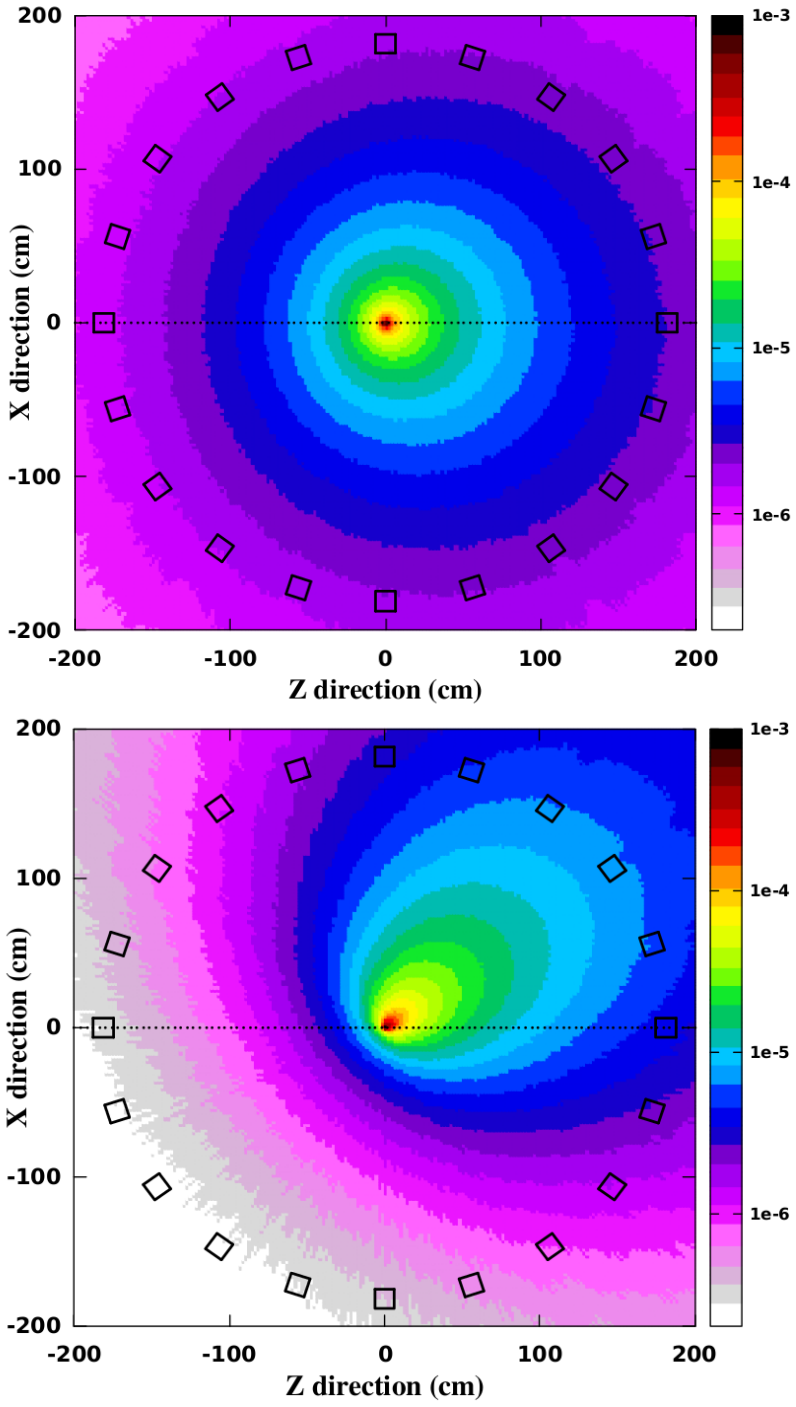

Figure 5.5: Spatial distribution of neutron fluence emitted by moving sources in the plane of beam axis (X-Z plane), simulated using FLUKA. Figure on the top corresponds to the neutron emission from CN moving along Z direction and the bottom figure shows the same from fragments moving at 40° w.r.t. Z direction.

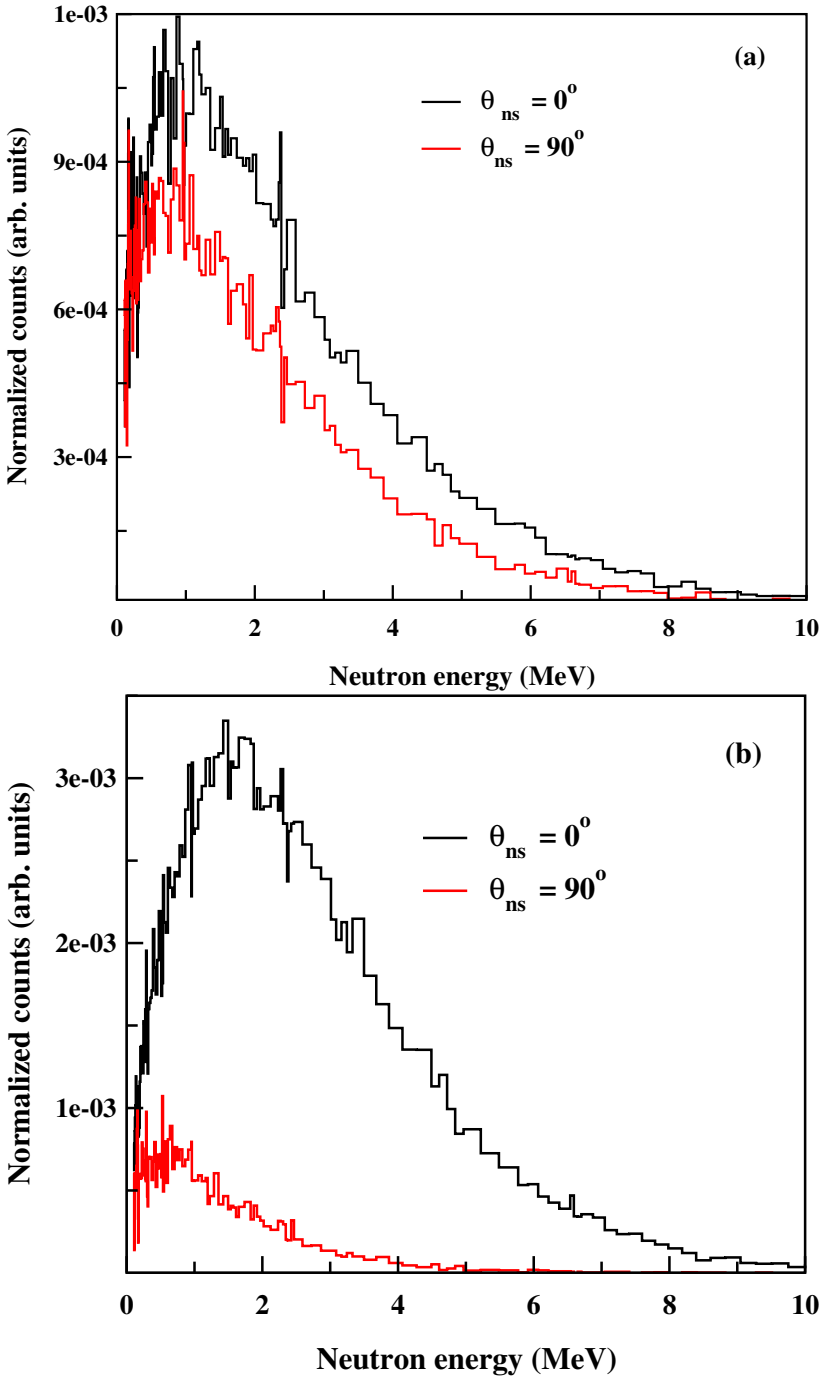

Figure 5.6: Kinetic energy distribution of neutrons emitted by moving sources at various angles. Figures show the changes in yield and spectrum of neutrons as the relative angle increases from $\theta_{ns} = 0°$ to 90°. (a) neutrons emitted by slow moving CN. (b) neutrons emitted by fast moving fission fragments.

neutrons per fission, is based on fitting the experimental neutron energy spectra at different angles by minimizing the χ^2. As known, the reliability of parameters extracted by χ^2 minimization techniques is critically dependent on the neutron evaporation model used. Neutron energy spectra at various angles as well as the relative angle between neutron source and neutron are the other two decisive parameters for extracting neutron multiplicity by the multi-source fitting procedure. In the following sub-sections, estimation of these two parameters and the formulation of the moving source model are described.

5.2.1 Measurement of neutron kinetic energy

The kinetic energy of fast neutrons was measured by the TOF technique. The flight path between the target and the front face of the BC501A detector of the NAND array is precisely set to be 175 cm. TOF of the fast neutrons in coincidence with the fission was recorded in event-by-event mode. As known, BC501A detectors are sensitive to both neutrons and γ-rays. Discrimination of neutrons from the γ-ray has been achieved by time of flight difference and pulse shape analysis. Figure 5.7 shows a typical n-γ discrimination spectrum obtained in the present measurement. To derive the energy spectrum, the TOF of neutrons, shown in the gated region, was calibrated by using the position of prompt γ_{peak} as the time reference,

$$T_{abs.}(ns) = m\ (TOF_{ch} - \gamma_{peak}) + T_{\gamma} \tag{5.24}$$

where m is the calibration constant expressed in ns/channels, TOF_{ch} is the TOF of neutrons in channels, γ_{peak} and T_{γ} are the position of reference γ-peak and its time of flight in ns respectively. Calibrated TOF data was converted energy histogram using the conventional equation,

$$E_n(MeV) = (\frac{1}{1.388^2})\ m_n\ v_n^2; \quad where, \quad v_n = \frac{distance(cm)}{T_{abs.}(ns)} \tag{5.25}$$

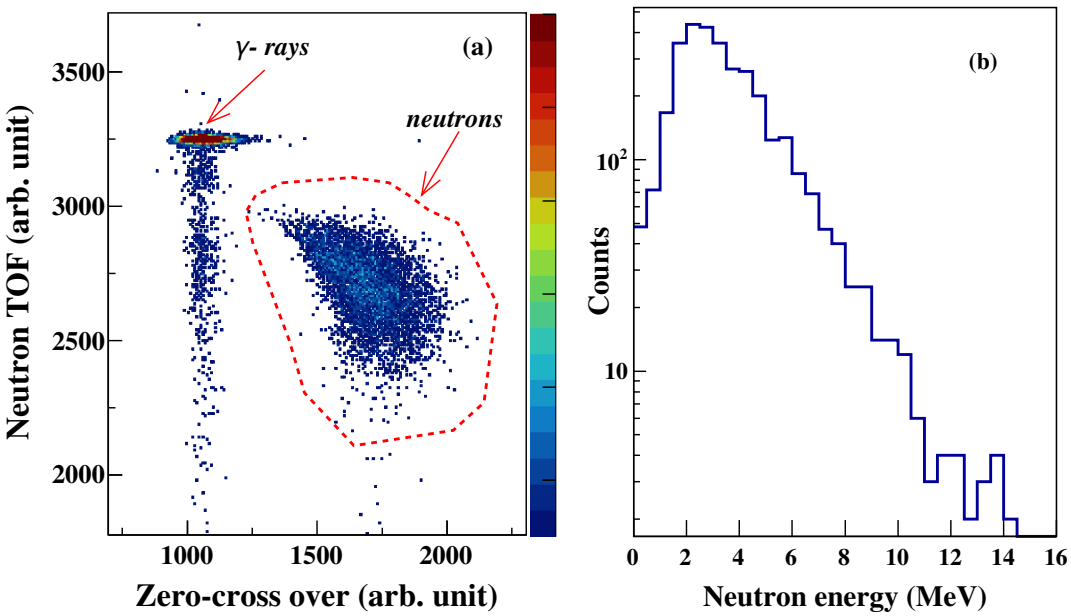

Figure 5.7: (a) Two dimensional plot of time of flight versus zero-cross over recorded in a BC501A detector. Well-separated neutron and γ bands are labelled in the figure. (b) A typical kinetic energy spectrum of neutrons derived from time of flight by applying n-γ discrimination gate, shown in the figure (a).

where m_n is the mass of neutron and v_n is its velocity in cm/ns.

5.2.2 Moving source model : Kinematic calculation

In the model used for χ^2 minimization, three neutron-emitting sources are considered: a slow-moving compound nucleus and two fast-moving fission fragments [11]. In the frame where the sources are at rest, the statistical model expression for neutrons evaporated from an excited nucleus is,

$$f(\overline{E})d\overline{E} \propto \overline{E}\ \sigma_{inv}(\overline{E})\ \exp(-\frac{\overline{E}}{T})d\overline{E} \tag{5.26}$$

where $\overline{E}$ is the neutron energy in rest frame $\sigma_{inv}(\overline{E})$ is the capture cross section for inverse reaction and T is the mean nuclear temperature [12, 13]. Symbols with bars indicate the parameters in the c.m. frame. From this equation, the double differential of neutron multiplicity for a given energy and solid angle ($d\Omega$)

is obtained as,

$$\frac{d^2M}{d\overline{E}d\overline{\Omega}} = M\ K\ \overline{E}\ \sigma_{inv}(\overline{E})\ \exp{(-\frac{\overline{E}}{T})} \tag{5.27}$$

where M is the neutron multiplicity and K is the normalization constant calculated by setting the integral $\frac{1}{4\pi}\int_0^\infty f(\overline{E})(d\overline{E})$ to unity. $\sigma_{inv}(\overline{E})$ can be expressed in simplified form as $1/\sqrt{\overline{E}}$ or calculated using parametric formula. In our computations, a parametric form proposed by Chatterjee et al. to $\sigma_{inv}(\overline{E})$ is used [14, 15]. The conversion from rest frame to the laboratory frame was performed using standard kinematics, including the Jacobian determinant as,

$$\frac{d^2M}{dE_Ld\Omega_L} = \frac{d^2M}{d\overline{E}d\overline{\Omega}}\ J(\frac{\overline{E}, d\overline{\Omega}}{E_L, \Omega_L}) \tag{5.28}$$

The explicit form of the Jacobian is a 2×2 determinant [16]:

$$J(\frac{\overline{E}, d\overline{\Omega}}{E_L, \Omega_L}) = \begin{vmatrix} \frac{\partial\overline{E}}{\partial E_L} & \frac{\partial\overline{E}}{\partial\Omega_L} \\ \frac{\partial\overline{\Omega}}{\partial E_L} & \frac{\partial\overline{\Omega}}{\partial\Omega_L} \end{vmatrix}$$

Figure 5.8 shows the velocity vector diagram of neutrons emitted by a moving source as well as the interdependence of velocity vectors in the c.m. and the laboratory frame. The following equations are derived to find the energy and emission angle of neutrons emitted by three moving sources [17, 18].

$$v_{c.m.}^2\ =\ v_L^2\ +\ v_S^2\ -\ 2\ v_L\ v_S\ cos(\theta_L) \tag{5.29}$$

$$\theta_{c.m.}\ =\ tan^{-1}(\ \frac{sin(\theta_L)}{cos(\theta_L) - v_S/v_L}) \tag{5.30}$$

where v_S is the velocity of neutron source, $v_{c.m}$ and v_L are velocities of neutrons in rest frame and laboratory frame respectively. $\theta_{c.m}$ is the emission angle in c.m frame and θ_L is the laboratory angle. Rewriting Equation 5.29 in terms of

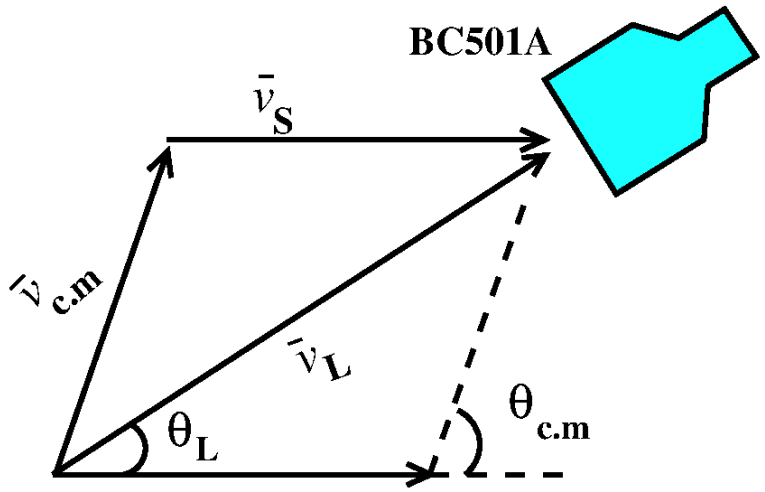

Figure 5.8: Diagram showing interdependence of velocity vectors in c.m. and laboratory frame for neutrons emitted from an accelerated source. The labels v_L and $v_{c.m.}$ represent the velocities in lab and c.m. frames respectively. v_S is the velocity of the source.

energy, we get,

$$E_{c.m} = E_L \; + \; Es/As \; - \; 2\sqrt{\frac{E_L \; E_S}{A_S}} \; cos(\theta_L) \tag{5.31}$$

where $E_{c.m}$ is the energy of neutron in the rest frame and E_S/A_S indicates the kinetic energy per nucleon of the neutron source.

Using the relations,

$$d\bar{\Omega} \; = \; 2\pi \; sin(\bar{\theta})d\bar{\theta}, \quad d\Omega_L \; = \; 2\pi \; sin(\theta_L)d\theta_L \tag{5.32}$$

as well as the Equations 5.30 and 5.31, the partial derivatives given in the Jaco-

bian determinant are calculated.

$$\frac{\partial \overline{E}}{\partial E_L} = 1 - r\ cos(\theta_L) \tag{5.33}$$

$$\frac{\partial \overline{\Omega}}{\partial E_L} = -(\frac{\pi\ r}{E_L})\frac{sin^3(\theta_{cm})}{sin(\theta_L)} \tag{5.34}$$

$$\frac{\partial \overline{E}}{\partial \Omega_L} = \frac{r\ E_L}{\pi} \tag{5.35}$$

$$\frac{\partial \overline{\Omega}}{\partial \Omega_L} = (1 - r\ cos(\theta_L))\ \frac{sin^3(\theta_{cm})}{sin^3(\theta_L)} \tag{5.36}$$

where $r = \frac{v_S}{v_L}$. And finally, the formula for Jacobian determinant is calculated as,

$$J(\frac{\overline{E}, d\overline{\Omega}}{E_L, \Omega_L}) = (1.0 - r\ cos\theta_L)^2\ \frac{sin^3\theta_{cm}}{sin^3\theta_L} + r^2\ \frac{sin^3\theta_{cm}}{sin\theta_L} \tag{5.37}$$

Equation 5.27 combined with the Jacobian transformation is used for predicting the double differential of neutron multiplicity spectrum at a given solid angle. For each neutron source, $\frac{d^2M}{dE_L d\Omega_L}$ is calculated separately using its multiplicity, temperature, source velocity, relative angle and mass. And the total is obtained by summing the contribution from each source,

$$\left\{\frac{d^2M}{dE_L d\Omega_L}\right\}_T = \left\{\frac{d^2M_{pre}}{dE_L d\Omega_L}\right\}_{CN} + \left\{\frac{d^2M_{post}}{dE_L d\Omega_L}\right\}_{F1} + \left\{\frac{d^2M_{post}}{dE_L d\Omega_L}\right\}_{F2} \tag{5.38}$$

where M_{pre} also labelled as ν_{pre} is the pre-scission neutron multiplicity and M_{post} (or, ν_{post}) is the post-scission neutron multiplicity. The measured neutron energy spectra at various angles were fitted with $\left\{\frac{d^2M}{dE_L d\Omega_L}\right\}_T$, by minimizing the χ^2, to extract the average neutron multiplicity and nuclear temperature.

5.2.3 Moving source model : Watt formula

B. E. Watt proposed a simplified formula to fit the energy spectrum of neutron from the thermal fission of ^{235}U [19]. The formula includes the following fundamental assumptions: (1) neutron emission is isotropic in the rest frame of

fragments, (2) neutrons are emitted from the fully accelerated fragments and (3) a simplified form of the neutron emission spectrum proportional to $\sqrt{E}\ \exp(-\frac{E}{T})$ in the c.m. frame. The formula reproduced the experimental data quite well in the measured energy range and was later termed the Watt formula. The Watt expression in the following form is widely used to represent the double differential of neutron multiplicity from three moving sources in heavy ion-induced fusion-fission,

$$\frac{d^2M}{dE_n d\Omega_n} = \sum_{i=1}^{3} \frac{\nu_i \sqrt{E_n}}{2(\pi T_i)^{3/2}}\ exp(-\frac{E_n + E_i/A_i - 2cos\theta_i \sqrt{E_n E_i/A_i}}{T_i}) \quad (5.39)$$

where A_i, E_i, T_i and ν_i are the mass number, kinetic energy, temperature and multiplicity of each neutron emitting source i, respectively. E_n is the laboratory energy of neutron and $d\Omega_n$ is the solid angle subtended by each BC501A detector. θ_i denotes the relative angle between neutron source and neutron detector. Though the Watt formula is an empirical equation, it is widely used for determining the neutron multiplicity and temperature of neutron sources due to its simplicity and ease of implementation in calculations [20–24].

5.2.4 Relative angle between neutron sources and neutrons

As emphasized in the previous sections, the angular distribution of neutrons in the laboratory frame is substantially modified in comparison to c.m. distribution due to kinematic effects. The three parameters that influence the laboratory distribution are the source's kinetic energy, kinetic energy of neutrons, and the relative angle between the neutron emission direction and the neutron source. The total number of neutrons registered in a given detector at a specific (θ, ϕ) is expected to have contribution from three moving sources: CN, fragment 1 and 2. The angle between the neutron detector and neutron sources is known as the relative angles, labelled as θ_n, θ_{nf1} and θ_{nf2} for the three sources CN, $f1$, and $f2$ respectively. The reference coordinate system (right handed Cartesian

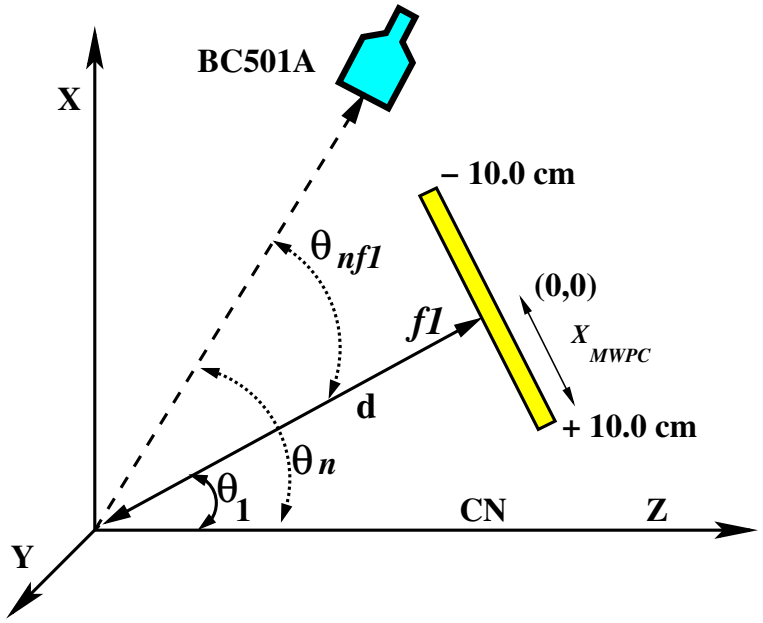

Figure 5.9: The Cartesian co-ordinate system, defining relative angles with respect to the direction of CN and fission fragments.

coordinates) is defined such that the beam travels down the Z axis. The following Figure 5.9 shows the coordinate system used and relevant angles.

Out of these moving sources, CN always moves nearly in beam direction (Z-axis). As a result, the relative angle θ_n is same as θ measured w.r.t. the reference coordinate system. On the other hand, fragments move in an angle θ_1 as shown in the Figure 5.9, where $0 < \theta_1 < 180$. Therefore the relative angle θ_{nf1} differs from θ of the reference system. The relative angle can be determined easily by taking the dot product of unit vectors along the fragment and neutron directions as,

$$\hat{a}.\hat{b} = |a|\,|b|\;\; cos\theta_{nf1} \tag{5.40}$$

$$\theta_{nf1} = cos^{-1}(a_x b_x + a_y b_y + a_z b_z) \tag{5.41}$$

The components of unit vectors (a_x, a_y, a_z) along the direction of neutron detectors are calculated from their known (θ, ϕ), using the standard conversion

equations,

$$a_x = sin\theta\ cos\phi \tag{5.42}$$

$$a_y = sin\theta\ sin\phi \tag{5.43}$$

$$a_z = cos\theta \tag{5.44}$$

The fission detectors provide the two dimensional positions (X_{MW}, Y_{MW}) w.r.t. their centre. To determine the components of unit vectors (b_x, b_y, b_z) of fragments w.r.t. the reference coordinate system (X,Y,Z), coordinate transformation has been performed. This comprises a rotation about the origin by θ_1 followed by a translation of d. The following transformation equations give the components of vectors along the (X,Y,Z) direction in terms of MWPC positions (X_{MW}, Y_{MW}).

$$b_x = -X_{MW}\ cos\theta_1\ + d\ sin\theta_1 \tag{5.45}$$

$$b_y = Y_{MW} \tag{5.46}$$

$$b_z = X_{MW}\ sin\theta_1\ + d\ cos\theta_1 \tag{5.47}$$

The component vectors are normalized with $R = \sqrt{b_x^2 + b_y^2 + b_z^2}$ to get the unit vector. The spherical polar coordinates of the fragment $f1$, (θ, ϕ), is calculated using the equations,

$$\theta_{f1} = cos^{-1}(\frac{b_z}{R}) \tag{5.48}$$

$$\phi_{f1} = tan^{-1}(\frac{b_y}{b_x}) \tag{5.49}$$

If $\phi_{f1} < 0.0$,then $\phi_{f1} = \phi_{f1} + 360.0$. By applying Equations 5.42 - 5.44 and 5.45 - 5.47 in formula 5.40, the relative angle θ_{nf1} has been calculated. Similarly, the relative angle θ_{nf2} can also be calculated by coordinate transformation of θ_2 and d. But, since (θ_{f1}, ϕ_{f1}) of the first fragment is known, the folding angle (θ_{fold})

correlation can be applied to find (θ_{f2}, ϕ_{f2}) of the second fragment as,

$$\theta_{f2} \;=\; \theta_{fold} \;-\; \theta_{f1} \tag{5.50}$$

If $\phi_{f1} < 180.0$; $\phi_{f2} = \phi_{f1} + 180.0$; else, $\phi_{f2} = \phi_{f1} - 180.0$. The components of the Cartesian coordinates (c_x, c_y, c_z) corresponding to (θ_{f2}, ϕ_{f2}) are calculated by,

$$c_x \;=\; sin\theta_2\ cos\phi_2 \tag{5.51}$$

$$c_y \;=\; sin\theta_2\ sin\phi_2 \tag{5.52}$$

$$c_z \;=\; cos\theta_2 \tag{5.53}$$

Then the relative angle for the complementary fragment θ_{nf2} has been calculated from the dot product $\theta_{nf2} = cos^{-1}(\hat{a}\ .\ \hat{c})$ as prescribed by 5.40.

The angle θ_1 between the MWPC centre and the beam direction in a given measurement is typically pre-determined. For example, in the current experiment setup, θ_1 was fixed at 40°. Due to the large angular coverage of MWPC detectors, more than 20° at d = 25 cm, there will be a significant degree of uncertainty in the relative angles θ_{nf1} and θ_{nf2}. To reduce the angular uncertainty, position gates were applied in the offline analysis which restricted the angular coverage to ± 8°.

5.3 Mass gated pre-scission neutron multiplicity

Mass gated neutron multiplicity measurements are generally performed to find the correlation of prompt neutron emission with fragment mass to investigate various aspects of fission dynamics. The current investigation focuses on the fusion-fission of ^{227}Pa in which the measurements were conducted within the excitation energy range of ≈ 30 - 60 MeV. Experimental investigations in this energy range show the evidences of shell effects in fragment mass distribution

and its attenuation with increase of excitation energy [25, 26]. The existence of shell effects at relatively higher excitation energy can be correlated with neutron emission from the compound nucleus before fission. Changes in the yields of fission modes can be correlated with the decrease in excitation energy at fission caused by multi-chance fission. In order to figure out the dependence of pre-scission neutron emission on fragment mass, ν_{pre} was extracted as a function of fragment mass for symmetric (A = 108u - 118u) and asymmetric (A = 128u - 140u) partition of mass distribution. The measurements were carried out energies E^* = 32.4 MeV ($\approx$ 4 % below the Coulomb barrier), 46.1 MeV and 59.6 MeV. In the following chapter, the salient results of neutron multiplicity measurements will be analyzed in the framework of theoretical calculation.

Bibliography

[1] R. Brun and F. Rademakers, Nuclear Instruments and Methods in Physics Research Section A: Accelerators, Spectrometers, Detectors and Associated Equipment **389**, 81 (1997), new Computing Techniques in Physics Research V, https://doi.org/10.1016/S0168-9002(97)00048-X.

[2] D. J. Hinde, M. Dasgupta, J. R. Leigh, J. C. Mein, C. R. Morton, J. O. Newton, and H. Timmers, Phys. Rev. C **53**, 1290 (1996), https://link.aps.org/doi/10.1103/PhysRevC.53.1290.

[3] A. C. Berriman, D. J. Hinde, D. Y. Jeung, M. Dasgupta, H. Haba, T. Tanaka, K. Banerjee, T. Banerjee, L. T. Bezzina, J. Buete, K. J. Cook, S. Parker-Steele, C. Sengupta, C. Simenel, E. C. Simpson, M. A. Stoyer, B. M. A. Swinton-Bland, and E. Williams, Phys. Rev. C **105**, 064614 (2022), https://link.aps.org/doi/10.1103/PhysRevC.105.064614.

[4] LISE++, https://lise.nscl.msu.edu/lise.html, https://lise.nscl.msu.edu/lise.html.

[5] H. Bethe and J. Ashkin, *Experimental Nuclear Physics* (John Wiley, New York 1953).

[6] D. Grimes, D. Warren, and M. Partridge, Scientific Reports **7**, 9781 (2017), https://doi.org/10.1038/s41598-017-10554-0.

[7] L. Northcliffe and R. Schilling, Atomic Data and Nuclear Data Tables **7**, 233 (1970), https://doi.org/10.1016/S0092-640X(70)80016-X.

[8] stopping power and range C/C++ library, https://github.com/ricardoyanez/rangelib.

[9] T. T. Böhlen, F. Cerutti, M. P. W. Chin, A. Fasso‘, A. Ferrari, P. G. Ortega, A. Mairani, P. R. Sala, G. Smirnov, and V. Vlachoudis, Nucl. Data Sheets **120**, 211 (2014).

[10] A. Ferrari, P. R. Sala, A. Fasso', and J. Ranft, CERN-2005-10(2005), INFN/TC_05/11, SLAC − R − 773 (2005).

[11] A. Chatterjee, S. N., and P. Sugathan, Proceedings of the DAE Symposium on Nuclear Physics **59**, 408 (2014), http://www.sympnp.org/proceedings/.

[12] V. Weisskopf, Phys. Rev. **52**, 295 (1937), https://link.aps.org/doi/10.1103/PhysRev.52.295.

[13] K. Le Couteur and D. Lang, Nuclear Physics **13**, 32 (1959), https://doi.org/10.1016/0029-5582(59)90136-1.

[14] A. Chatterjee, K. H. N. Murthy, and S. K. Gupta, Pramana **16**, 391 (1981), https://www.ias.ac.in/article/fulltext/pram/016/05/0391-0402.

[15] I. Dostrovsky, Z. Fraenkel, and G. Friedlander, Phys. Rev. **116**, 683 (1959), https://link.aps.org/doi/10.1103/PhysRev.116.683.

[16] G. L. Catchen, J. Husain, and R. N. Zare, The Journal of Chemical Physics **69**, 1737 (1978), https://doi.org/10.1063/1.436749.

[17] N. Saneesh, D. Arora, A. Chatterjee, K. Golda, M. Kumar, A. Vinodkumar, and P. Sugathan, Nuclear Instruments and Methods in Physics Research Section A: Accelerators, Spectrometers, Detectors and Associated Equipment **1013**, 165682 (2021), https://doi.org/10.1016/j.nima.2021.165682.

[18] A. Göök, F.-J. Hambsch, and M. Vidali, Phys. Rev. C **90**, 064611 (2014), https://link.aps.org/doi/10.1103/PhysRevC.90.064611.

[19] B. E. Watt, Phys. Rev. **87**, 1037 (1952), https://link.aps.org/doi/10.1103/PhysRev.87.1037.

[20] D. Hilscher and H. Rossner, Ann. Phys. Fr. **17**, 471 (1992), https://doi.org/10.1051/anphys:01992001706047100.

[21] D. J. Hinde, D. Hilscher, H. Rossner, B. Gebauer, M. Lehmann, and M. Wilpert, Phys. Rev. C **45**, 1229 (1992), https://link.aps.org/doi/10.1103/PhysRevC.45.1229.

[22] D. Hinde, R. Charity, G. Foote, J. Leigh, J. Newton, S. Ogaza, and A. Chattejee, Nuclear Physics A **452**, 550 (1986), https://doi.org/10.1016/0375-9474(86)90214-9.

[23] M. Thakur, B. R. Behera, R. Mahajan, G. Kaur, P. Sharma, K. Kapoor, K. Rani, P. Sugathan, A. Jhingan, N. Saneesh, R. Dubey, A. Yadav, A. Chatterjee, M. B. Chatterjee, N. Kumar, S. Mandal, S. K. Duggi, A. Saxena, S. Kailas, and S. Pal, Phys. Rev. C **98**, 014606 (2018), DOI: 10.1103/PhysRevC.98.014606.

[24] N. Kumar, S. Verma, S. Mohsina, J. Sadhukhan, K. Rojeeta Devi, A. Banerjee, N. Saneesh, M. Kumar, R. Mahajan, M. Thakur, G. Kaur, A. Rani, Neelam, A. Yadav, Kavita, R. Kumar, Unnati, S. Mandal, S. Kumar, B. Behera, K. Golda, A. Jhingan, and P. Sugathan, Physics Letters B **814**, 136062 (2021), https://doi.org/10.1016/j.physletb.2021.136062.

[25] M. G. Itkis, L. Calabretta, F. Hanappe, Y. M. Itkis, A. Kelic, N. A. Kondratiev, E. M. Kozulin, Y. Oganessian, I. V. Pokrovsky, E. V. Prokhorova, G. Rudolf, A. Y. Rusanov, and L. Stuttge, Nuclear Physics A **654**, 870c (1999), https://doi.org/10.1016/S0375-9474(00)88563-2.

[26] R. Dubey, P. Sugathan, A. Jhingan, G. Kaur, I. Mukul, G. Mohanto, D. Siwal, N. Saneesh, T. Banerjee, M. Thakur, R. Mahajan, N. Kumar, and M. Chatterjee, Physics Letters B **752**, 338 (2016), https://doi.org/10.1016/j.physletb.2015.11.060.

Chapter 6

Results and discussion : Impact of multi-chance fission

The mechanism of mass division in the fission of an excited nucleus has been the subject of intense research since the discovery of fission. Generally, it is observed that fission in the actinide region has bimodal characteristics (symmetric and asymmetric) [1–4]. Fission at higher excitation energies (E^*) leads to a symmetric distribution of fragment masses, as predicted by the macroscopic liquid drop model [5]. On the other hand, mass distribution is generally found to be asymmetric at lower excitation energies [6]. An overlap of these two distinct fission modes may occur when fission is preceded by consecutive particle emission, a phenomenon called multi-chance fission (MCF).

Neutron emission reduces the initial excitation energy of the compound nucleus (CN) to $E^* - S_n - E_n$, where S_n is the neutron separation energy and E_n is the neutron kinetic energy. Chance fission occurs only at higher E^*, sufficient for allowing fission after neutron evaporation, and it is important to account for its probability when interpreting the observables of fission at higher excitation energies. In a seminal work by Hirose *et al.*, the influence of multichance fission in actinide nuclei at higher excitation energies was investigated through fragment mass distribution [7]. In the experimental studies, fission in actinide

targets was induced by the multi-nucleon transfer (MNT) process. The apparent mass-asymmetric fission at higher excitation energies ($\approx$ 60 MeV) was explained in light of MCF. Despite the high initial E^*, the multichance or sequential nature of fission decay restored the shell effects in these nuclei.

Unlike fission induced by MNT, the full momentum transfer (FMT) process (e.g in fusion reactions) results in the formation of neutron-deficient compound nuclei. The probability of a higher chance fission is lower in such systems compared to CN formed via MNT. Therefore, an early washout of the shell effects as a function of E^* can be expected in these nuclei [8]. However, if the MCF, particularly higher chance fission contributes significantly at any given excitation energy, the revival of microscopic effects needs to be invoked to explain the experimental results. As described earlier, the measurement of pre-scission neutron multiplicity (ν_{pre}) and ν_{pre} in correlation with fission fragment mass can provide precise data to comment on the role of pre-scission emission on mass division.
To investigate the impact of multi-chance fission in experiment observables, we have measured the mass distribution of fragments, average ν_{pre} and mass gated ν_{pre} in a lighter actinide nucleus ^{227}Pa formed via ^{19}F+^{208}Pb fusion reaction. The experimental techniques and analysis methods are described in detail in the previous chapters. In this chapter, we discuss the results of these measurements, the theoretical calculations performed to understand the experimental observables and their correlation, etc.

6.1 Results of mass distribution, $< \nu_{pre} >$ and mass gated ν_{pre} measurements

Fission fragment mass distribution, average ν_{pre} and mass gated ν_{pre} of the excited compound nucleus ^{227}Pa were extracted at different beam energies in the range 90 - 120 MeV. For proper validation of the theoretical model, $< \nu_{pre} >$ was measured at laboratory energies: E_{lab} = 90 MeV, 95 MeV, 100 MeV, 105 MeV,

and 120 MeV. Analysis to derive the mass distribution and mass gated ν_{pre} were concentrated at E_{lab} = 90 MeV, which is ≈ 4 % below the Coulomb barrier, 105 MeV, and 120 MeV. The corresponding excitation energies are E^* = 32.4 MeV, 46.1 MeV and 59.6 MeV respectively.

6.1.1 Mass distribution

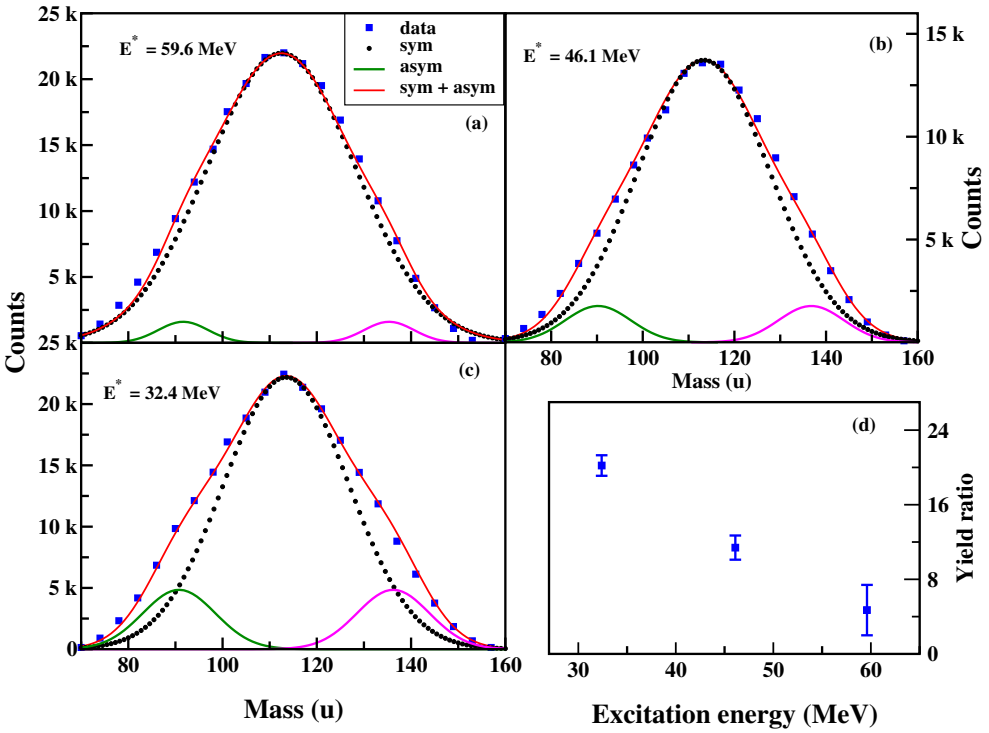

Figure 6.1: Panels (a)-(c) Mass distribution of fission fragments at three excitation energies. Measurements are shown in filled squares. The results of multi-Gaussian fit to the measurements are also shown. The black dotted curve represents the symmetric component and asymmetric components are shown with green and pink lines. The red solid line indicates the sum of symmetric and asymmetric components of mass distribution. (d) The ratio, in percentage, of asymmetric component to the total mass yield at three excitation energies.

Mass distribution was extracted by the velocity reconstruction method. The obtained mass distribution of fragments at E* = 32.4 MeV, 46.1 MeV, and 59.6 MeV are shown in the Figure 6.1. At the highest excitation energy studied (E* = 59.6 MeV), the mass curve is nearly symmetric and can be fitted fairly well with a single Gaussian function. On the other hand, at lower excitation energies,

the mass distribution deviates from the symmetric Gaussian shape and exhibits the contributions of asymmetric components.

To quantify the asymmetric yield, multi-Gaussian functions were used to fit the mass distribution curve. The underlying assumption is that, the broadening and resultant deviation from symmetric Gaussian curve is due to asymmetric splitting of the compound nucleus at lower excitation energies. Furthermore, the asymmetric components have equal area and their masses sum to compound nuclear mass (A_1+A_2=A_{CN}) for all asymmetric fission. The following three Gaussian functions were applied to fit the experimental mass curve by χ^2 minimization method.

$$G_s(x) = \frac{a_1}{\sigma_1\sqrt{2\pi}}\ exp(-\frac{(x-\mu_1)^2}{2\sigma_1^2}) \tag{6.1}$$

$$G_{as1}(x) = \frac{a_2}{\sigma_2\sqrt{2\pi}}\ exp(-\frac{(x-\mu_2)^2}{2\sigma_2^2}) \tag{6.2}$$

$$G_{as2}(x) = \frac{a_3}{\sigma_3\sqrt{2\pi}}\ exp(-\frac{(x-\mu_3)^2}{2\sigma_3^2}) \tag{6.3}$$

where $G_s(x)$, $G_{as1}(x)$ and $G_{as2}(x)$ are the Gaussian functions used to represent symmetric and asymmetric components of fission. Given the complementarity of fragments in binary fission ($a2 = a3, \sigma_2 = \sigma_3, \mu_3 = A_{CN} - \mu_2$), the nine variables (a, σ, μ) of three Gaussian function can be constrained to six. Moreover, the centroid of the symmetric fission can be fixed to $\mu_1 = A_{CN}/2$. Further, the width of symmetric Gaussian was also fixed based on theoretical calculations [9]. And the experimental mass distribution curve was fitted with,

$$F(x) = G_s(x) + G_{as1}(x) + G_{as2}(x) \tag{6.4}$$

considering a_1, a_2, σ_2 and μ_2 as free parameters. The fit results are summarized in the Table 6.1. Figure 6.1(a)-(c) shows the relative contribution of three Gaussian curves to the total experimental mass curve at these excitation energies. The yield ratio (Y), which is the ratio of asymmetric to symmetric fission yield, is

Table 6.1: Results of three-Gaussian fit to the mass distribution measured at different excitation energies.

E^* (MeV)	σ_1 (u)	σ_2 (u)	μ_1	μ_2	Yeild ratio (%)
32.4	15.7	7.7	91	136	20.2 ± 1.1
46.1	14.4	7.2	90	137	11.4 ± 1.3
59.6	13.2	5.4	91	136	4.8 ± 2.7

defined as,

$$Y(\%) \;=\; \frac{2\ a_2}{(a_1 + 2\ a_2)}\ 100 \tag{6.5}$$

where a_1 and a_2 are the area under symmetric and asymmetric Gaussian curves. Error in the yiels ratio (σ_Y) can be calculated as,

$$\sigma_Y(\%) \;=\; \sqrt{(\frac{\partial Y}{\partial a_1})^2\ \sigma_{a1}^2\ + (\frac{\partial Y}{\partial a_2})^2\ \sigma_{a2}^2} \qquad \textit{which gives;} \tag{6.6}$$

$$\sigma_Y(\%) \;=\; 2\ \frac{\sqrt{a_1^2\ \sigma_{a2}^2 + a_2^2\ \sigma_{a1}^2}}{(a_1\ + 2\ a_2)^2}\ 100 \tag{6.7}$$

where σ_{a1} and σ_{a2} are the errors in a_1 and a_2 respectively. Figure 6.1(d) shows the yield ratio extracted by fitting the experimental mass curve.

6.1.2 Average neutron multiplicity

Neutron multiplicity was extracted by fitting the energy spectra of neutrons measured at various angles relative to three moving neutron sources. A global fit to the double differential neutron spectra ($\frac{d^2M}{dEd\Omega}$) at various angles was applied by minimizing the χ^2 to obtain the pre-scission and post-scission neutron multiplicities.

Figure 6.2 shows an example of the moving source fit to the experimental neutron multiplicity spectrum in the laboratory frame for E^* = 46.1 MeV. In Figure 6.2(a) and (b), the double differential of neutron multiplicity are shown

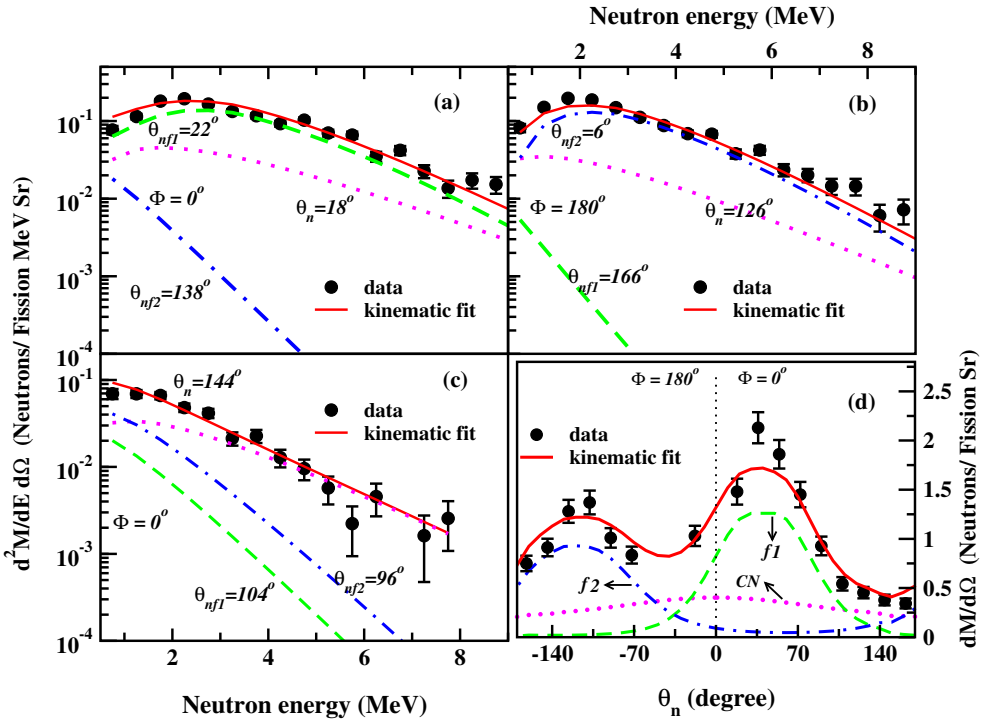

Figure 6.2: Panels (a)-(c) Examples of the three-moving-source fits to double differential neutron multiplicity spectra in the laboratory frame at various angles for ^{19}F+^{208}Pb reaction at 105 MeV beam energy. (d) Angular correlation of neutron yield $dM/d\Omega$ as a function of θ_n for 16 detectors in the reaction plane. The contributions from individual neutron sources are indicated by curves; green dashed (fragment 1), blue dot-dashed (fragment 2) and pink dotted (CN source). The red solid line indicate total contributions from all sources and black solid circles denote data points with statistical errors. The dotted vertical line in (d) at $\theta_n = 0°$ separates the data measured at $\Phi = 0°$ and 180°.

as a function of neutron energy for two NAND detectors near the MWPCs in the reaction plane. As expected, due to kinematic focusing, these spectra are dominated by contributions from their respective fission fragments. Figure 6.2(c) shows the fit result of the data from the NAND detector at backward angle. This spectrum shows the largest contribution from pre-scission neutrons (CN source). In Figure 6.2(d), the derivative of the total neutron multiplicity $dM/d\Omega$ is plotted as a function of relative angle θ_n for 16 NAND detectors mounted in the reaction plane. It shows the contribution of three neutron emitting sources to the total neutron yield $dM/d\Omega_n$ at various angles and the corresponding value obtained from the kinematic fit. The excellent agreement between multiple moving-source fits and experimental spectra displayed in Figure 6.2(a), (b), (c) & (d) indicates

Table 6.2: Experimentally obtained pre-scission neutron multiplicities (average and mass-gated) of ^{227}Pa at different excitation energies.

E_{lab} (MeV)	E^* (MeV)	$< \nu_{pre} >$	$< \nu_{post} >$	$< \nu_{pre} >_{sym}$	$< \nu_{pre} >_{asym}$
76.0	24.2	0.92 ± 0.14		0.81 ± 0.14	1.00 ± 0.14 [10]
90.0	32.4	1.44 ± 0.25	1.46 ± 0.08	1.32 ± 0.31	1.60 ± 0.36
95.0	36.6	1.55 ± 0.22	1.64 ± 0.08		
100.0	41.4	1.83 ± 0.18	1.53 ± 0.11		
105.0	46.1	1.96 ± 0.25	1.85 ± 0.08	2.01 ± 0.27	1.83 ± 0.33
120.0	59.6	2.58 ± 0.32	2.04 ± 0.11	2.66 ± 0.35	2.43 ± 0.43

the data are well described by three moving sources. The average ν_{pre} and ν_{post} extracted from the fitted spectra are listed in Table 6.2.

6.1.3 Mass gated pre-scission neutron multiplicity

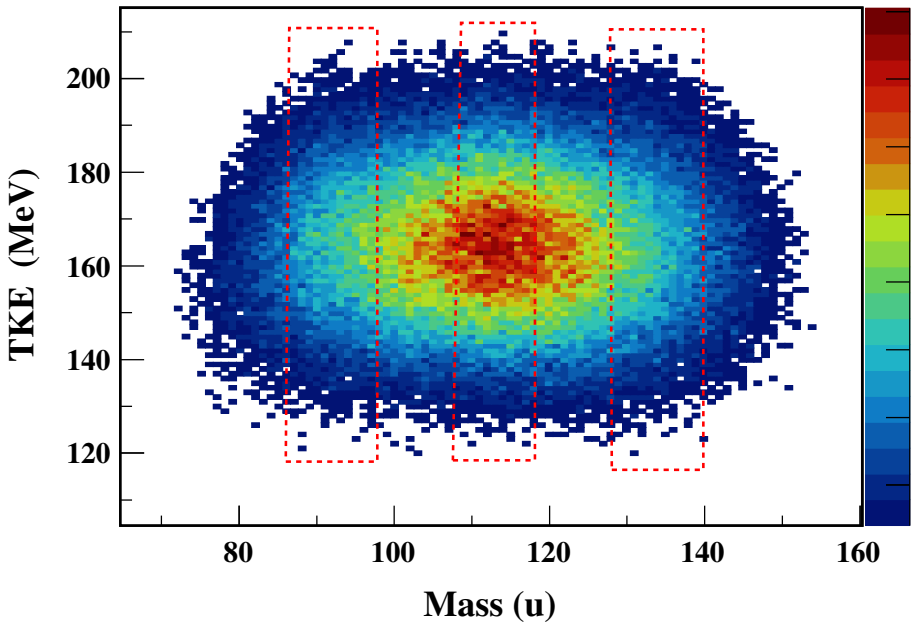

Figure 6.3: Distribution of total kinetic energy of fission fragments as function of mass for ^{19}F+^{208}Pb reaction at 105 MeV beam energy. The vertical rectangles represent the mass gates defined at symmetric and asymmetric region of the distribution to extract mass-gated neutron multiplicity.

To find the dependence of pre-scission neutron emission on fragment mass,

ν_{pre} was extracted for symmetric (108u - 118u) and asymmetric (86u - 98u (left) and 128u - 140u (right)) partition of mass distribution at E* = 32.4 MeV, 46.1 MeV and 59.6 MeV. Figure 6.3 shows the $Mass - TKE$ correlation spectrum obtained for E* = 32.4 MeV in which various mass gates (symmetric and asymmetric) used for finding ν_{pre} are drawn in red dotted lines. The mass gated neutron multiplicities for measured energies are shown in Table 6.2. The table also includes the mass gated ν_{pre} for ^{227}Pa measured at E* = 24.2 MeV. In this measurement [10], the compound nucleus ^{227}Pa was populated by fusion of ^{18}O with ^{209}Bi target.

6.2 GEF model calculations

At lower excitation energies, we have experimentally observed the occurrence of asymmetric components in the mass distribution. Additionally, the results of mass gated ν_{pre} measurements at E* = 32.4 MeV suggest a larger probability of asymmetric fission upon higher pre-scission neutron emission. But the asymmetric components of mass are negligible at the highest excitation energy studied (E* $\approx$ 60 MeV). At this energy, the mass gated ν_{pre} exhibits the typical pattern seen in the liquid drop fission [11]. The observed deviations at lower excitation energies can be attributed to the multi-chance nature of fission.

It is challenging to determine the probability or impact of a given fission chance since the experimental data is an admixture of all fission chances. However, theoretical calculations that consider MCF in the fission decay [9, 12, 13] can be used to determine the contribution of each chance to overall fission outcomes if the calculation reproduces experimental observables. Average ν_{pre} is one such observable that has a direct relationship with MCF probability. Comparison of experimental ν_{pre} with theory for various E^* shall validate the MCF probability incorporated in the theoretical model. Validated MCF models can therefore be used to predict the influence of neutron emission on fission modes at different excitation energies. Thus, a direct comparison between experiments

Table 6.3: Results of the coupled channels calculation to estimate the average angular momentum of the compound nucleus at different beam energies.

E^{lab} (MeV)	$E_{c.m}$ (MeV)	σ_{fus} (mb)	$< l >$ ($\hbar$)	$\sigma_{fus}(exp)$ [14] (mb)
90	82.4	2	7.5	43 ± 0.2
95	87.0	124	11.7	163 ± 0.8
100	91.6	351	18.0	382 ± 2
105	96.2	514	23.8	515 ± 3
120	109.9	960	34.2	953 ± 5

and model predictions can be applied to deduce the influence of various fission chances on experimental observables. The calculations were performed using GEneral description of Fission observables (GEF) model [9]. For the present study, *GEF Version 2021/1.1* is used. GEF is a semi-empirical code widely used in low energy fission for describing fission observables and their correlations using global parameter values [9, 15, 16]. It describes the sequential decay of a nucleus specified by its excitation energy (E^*) and average angular momentum ($< l >$). For the compound nucleus ^{227}Pa formed in fusion reaction ^{19}F+^{208}Pb at various excitation energies, the $< l >$ corresponding to each excitation energy was determined using coupled-channels calculation code CCFULL [17]. The input parameters for CCFULL calculation such as the nuclear potential, radius parameter, diffuseness parameter, etc. were taken from [18]. With these parameters, the measured cross-sections were reproduced quite well in the whole energy range, and the corresponding $< l >$ values were obtained [14, 18]. It is worth to note that in the lower $< l >$ range ($l < 15$), small deviations in $< l >$ values does not influence the fission chance probability considerably. Table 6.3 shows the results of the CCFULL calculation along with the experimentally measured fusion cross section. GEF model calculations were performed for different values of ($E^*, < l >$) corresponding to measured beam energies, taking into account the multi-chance fission in the CN decay scheme. The distributions of fission fragment mass, kinetic energy, neutron multiplicity, and their correlations were

obtained from the list-mode output generated by GEF.

6.3 Validation of GEF model calculation

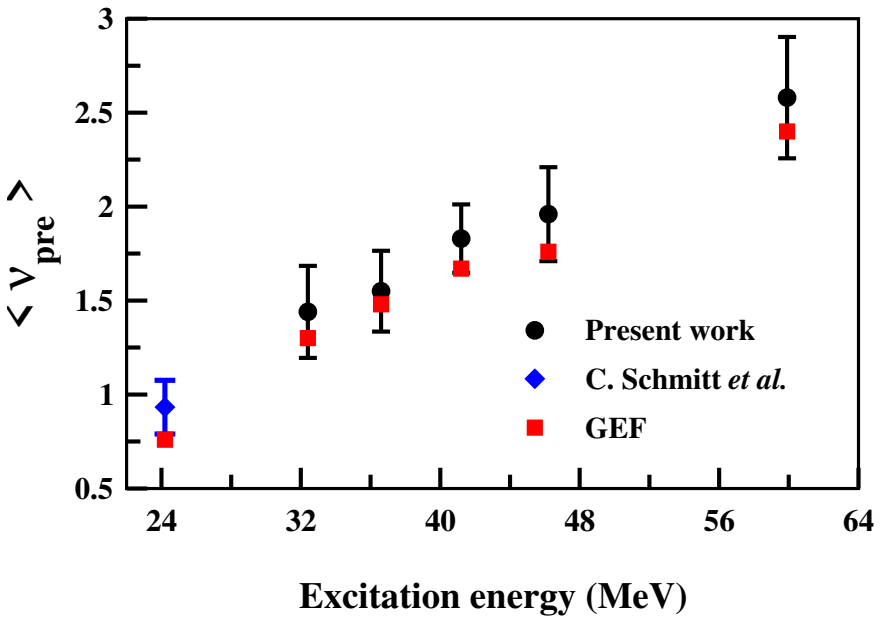

Figure 6.4: Pre-scission neutron multiplicity measured for ^{227}Pa in the range of E* = 24.2 - 59.6 MeV. Present measurements are shown in filled circles and previous measured data is denoted with filled diamond [10]. GEF model prediction corresponding each measurement is shown in filled squares.

As described earlier, the fission decay probability incorporated in the GEF model can be validated through $< \nu_{pre} >$ measurements. ν_{pre} is the sum of pre-saddle (ν_{ps}) and saddle to scission (ν_{ss}) neutron multiplicities. The pre-saddle neutron multiplicity can be related to various fission chances as,

$$< \nu_{ps} > = \frac{\sum_{i=1}^{n} (i-1)\ P_i^f}{\sum_{i=1}^{n} P_i^f} \tag{6.8}$$

where P_i^f is the probability of fission for a given chance i. Post-saddle emission does not alter the observables or probability of fission [9, 19]. In Figure 6.4, the average ν_{pre} obtained from the GEF model calculation is compared with the experiment results. The black-filled circle symbols represent data from the

present measurement. The error bars shown are only statistical errors. The data represented using the filled diamond symbol is from Ref.[10], where CN ^{227}Pa was studied using the reaction ^{18}O+^{209}Bi. The filled-square symbols show the GEF results. It is observed that the GEF model reproduces the experimental data within error bars reasonably well across all measured energy in the range, E* $\approx$ 24 MeV - 60 MeV. This ascertains that sequential fission decay analysis incorporating a specific yield to a given fission chance (P_i^f) can describe the experimental results. As particle emission lowers the excitation energy, the potential energy surface that governs the fission modes will be modified after each fission chance [1]. Therefore, analyzing the observables (mass distribution and kinetic energy) of each fission chance separately can give important information about the revival of shell effects on pre-saddle neutron emission. Since $< \nu_{pre} >$ measurements validate the sequential fission decay scheme of GEF, the calculation has been extended to study the observables of each fission chance by analyzing the GEF list-mode outputs at initial excitation energies E^*= 59.6 MeV, 46.1 MeV, 32.4 MeV, and 24.2 MeV where mass gated $< \nu_{pre} >$ results have been obtained.

6.4 Multi-chance fission and its impact on experimental observables

6.4.1 Mass distribution : Theory and measurements

GEF model calculation was performed to find the mass distribution of fission fragments from the fission of ^{227}Pa at E*= 59.6 MeV, 46.1 MeV and 32.4 MeV. The sequential decay of CN, validated by $< \nu_{pre} >$ measurements, was incorporated in the calculation. In the previous section 6.1.1, the percentage of asymmetric fission that was determined by fitting the experiment data is discussed. Experiment data shows a relatively higher contribution of asymmetric fission at

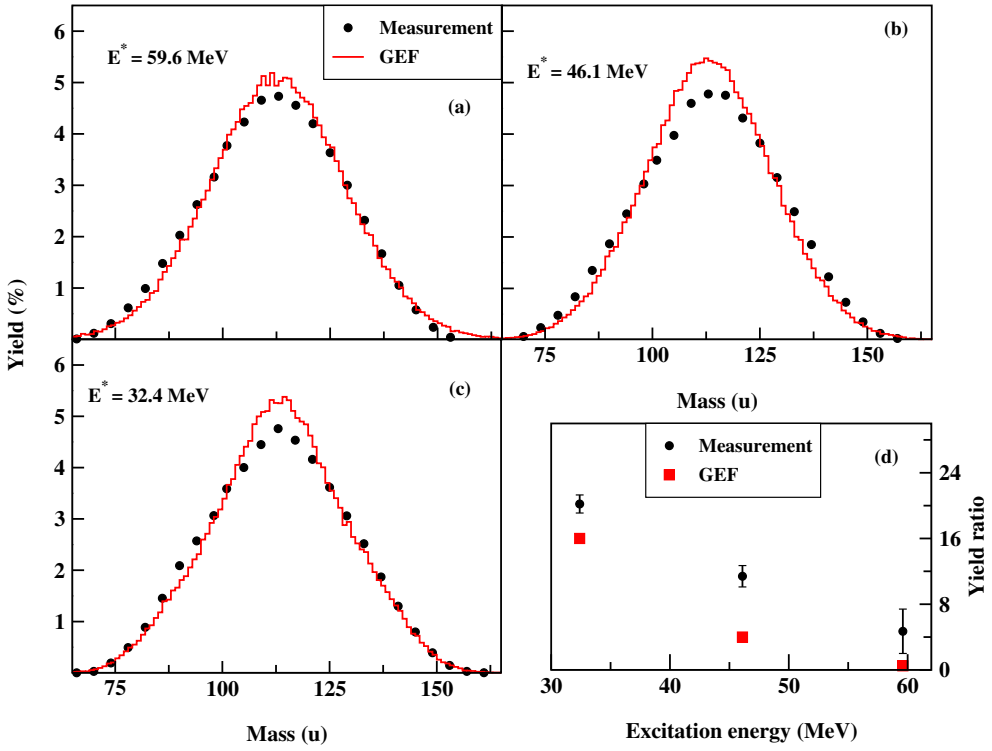

Figure 6.5: Panels (a)-(c) Comparison of experimental mass distribution with GEF model calculations at three excitation energies. (d) Asymmetric yield ratio, in percentage, predicted by GEF at these excitation energies is compared with the results of multi-Guassian fit to the experimental data.

all measured energies. In the Figure 6.5, a comparison of GEF calculations with measurements for these excitation energies is presented. Figures 6.5(a), (b), and (c) show the overall mass distribution obtained from measurements and calculations. The Y-axes are normalized to 200 %. And Figure 6.5(d) compares the percentage yield of asymmetric fission.

GEF model predicts ≈ 16 % of asymmetric fission of type S-II [4] at E^*= 32.4 MeV, ≈ 4 % at E^*= 46.1 MeV and ≈ 0.5 % at E^*= 59.6 MeV. Model calculation excluding multi-chance fission gives negligible yield (< 0.3%) of asymmetric fission at all these energies. This implies that the shell influenced asymmetric fission, represented by S-II, is originated by the neutron emission and the subsequent decrease in excitation energy at fission. An admixture of symmetric and asymmetric fission modes results in the final mass spectrum slightly deviated from Guassian distribution. Figure 6.5 shows mass distribution at E^*=

59.6 MeV matches quite well with GEF predictions. And slight deviations from the GEF model can be observed in Figure 6.5(b) (E^*= 46.1 MeV) and Figure 6.5(c) (E^*= 32.4 MeV). At these energies, expriment data shows higher percentage of asymmetric fission as highlighted in the Figure 6.5(d). Since the mass distribution curves (Figure 6.5(a), (b) and (c)) are normalized uniformily, yield percentage of symmetric fission has to be lower than GEF prediction at these energies. As anticipated, Figure 6.5(b) and Figure 6.5(c) show lower yield for symmetric fission in the experiment data. On the whole, though slight deviations are observed between theory and measurements, inclusion of multi-chance fission is inevitable to explain the experimental results.

6.4.2 $Mass$ - TKE correlation : GEF model

The changes in the total kinetic energy of fission fragments as a function of mass at different compound nuclear excitation energies is one of the probes used for studying various fission modes [1, 20]. In low energy fission of actinide nuclei, shell effects give rise to asymmetric mass division with heavier mass centred around A $\approx$ 140 and an increase in TKE due to the compact configuration of nascent fragments [4]. Measuring the $Mass$ - TKE correlation following each chance fission is a big experimental challenge. However, the contribution from each step of multi-chance fission has been theoretically investigated using the GEF code. For the present study of ^{227}Pa at four initial excitation energies, GEF predicted chance fission probability (P_i^f) is listed in Table 6.4. Multi-chance fission with a probability less than 5 % is not considered here as they do not contribute significantly to the total fission yield. The average saddle point excitation energy ($< E_{sp} >_i$), also called the excitation energy at fission, for a given chance fission i and the saddle point excitation energy averaged over all chances ($< E_{sp} >$) are also given in the Table 6.4. The E_{sp} after particle emission is the minimum for last-chance fission. Therefore, the influence of fragment shells, if exist, will be seen predominantly in the observables arising out of last-chance

Table 6.4: GEF model calculation showing the probabilities of various fission chances, average saddle point energy and pre-saddle multiplicity at different excitation energies of ^{227}Pa.

E^* (MeV)	fission chances	P_i^f (%)	$< E_{sp} >_i$ (MeV)	$< \nu_{ps} >$	$< E_{sp} >$ (MeV)
59.6	1	7.4	59.6	2.24	38.1
	2	17.0	49.1		
	3	30.7	39.9		
	4	32.0	30.4		
	5	10.6	23.3		
46.1	1	11.6	46.1	1.76	30.0
	2	26.1	35.9		
	3	37.8	27.4		
	4	21.9	18.6		
32.4	1	17.6	32.4	1.30	20.8
	2	39.3	22.8		
	3	38.1	15.3		
	4	5.0	7.3		
24.2	1	34.7	24.2	0.76	17.5
	2	54.3	15.2		
	3	11.0	8.1		

fission.

From GEF list-mode output, the $Mass - TKE$ correlations were calculated independently for every chance fission given in Table 6.4. Figure 6.6 (panels (a) through (u)) shows the findings for each chance fission (labelled as ch1, ch2, etc.) and their weighted average for E* = 59.6 MeV, 46.1 MeV, 32.4 MeV, and 24.2 MeV. The upper panels (a), (b), (c), and (d) display the $Mass - TKE$ distribution from first chance fission events. The spectra do not reveal any detectable signs of shells at any of the excitation energies. The next lower panels (e), (f), (g) and (h)) display the results for second chance fission. Similar findings may be seen except for panel (h) which show the occurrence of asymmetric fission caused by fragment shell effects. An enhanced contribution of asymmetric components to the total mass distribution is seen in the subsequent lower panels (k), (l), and (o). At E* = 24.2 MeV and 32.4 MeV, the last chance fission (ch3 and ch4 respectively) show the highest contribution of shell mediated asymmetric

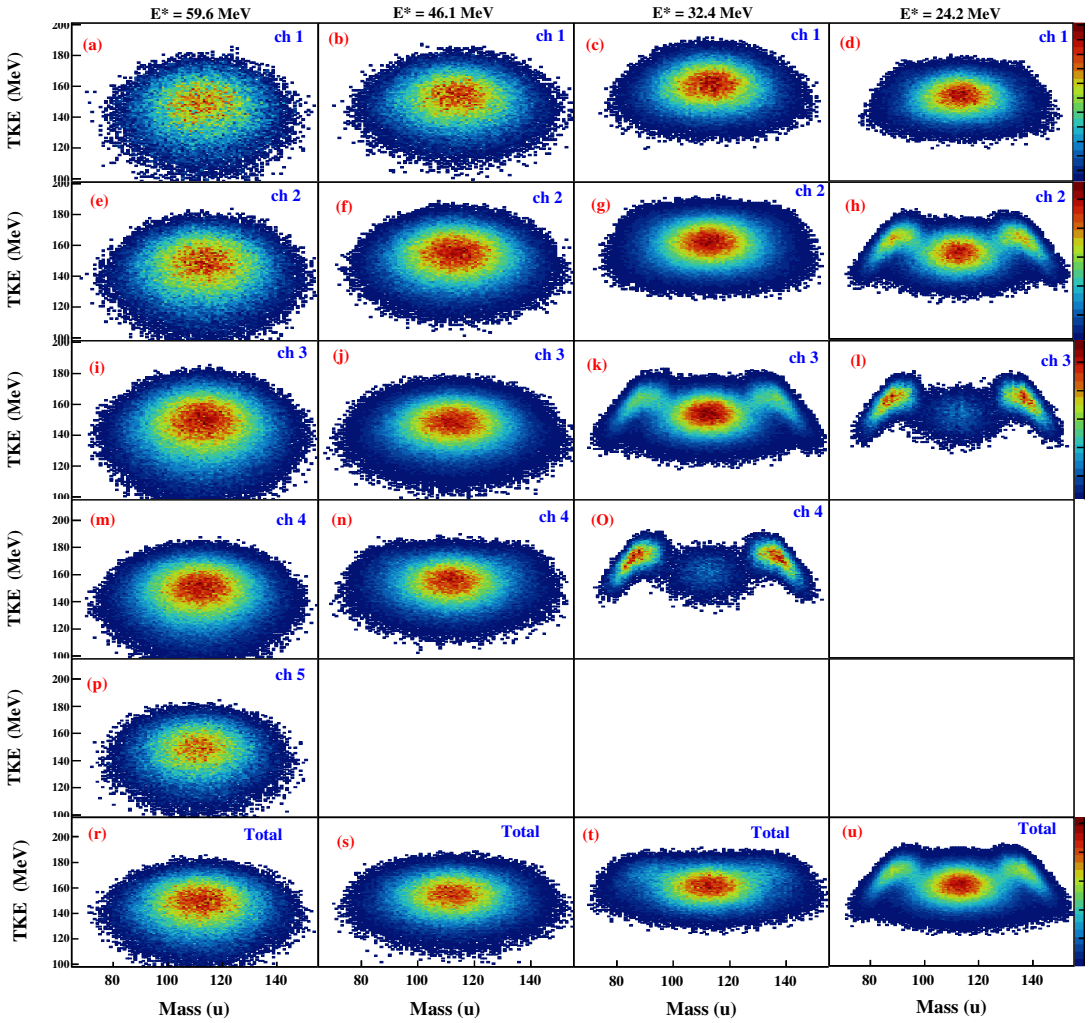

Figure 6.6: GEF predicted $Mass$ - TKE correlations for ^{227}Pa at E* = 59.6, 46.1, 32.4 and 24.2 MeV. The upper panels (a)-(d) correspond to GEF produced $Mass$ - TKE spectra corresponding to the first chance fission. Similarly, the $Mass$ - TKE spectra for second, third, fourth and fifth chances are shown in panels (e)-(h), (i)-(l), (m)-(o) and (p) respectively. Blank region indicates the absence of corresponding fission chances at that excitation energy. Bottom panels (r)-(u) show the $Mass$ - TKE spectra obtained by the averaging all the fission chances according to their probability, for a given excitation energy.

fission to the total fission due to their excitation lower energy at fission ($< E_{sp} >_i$) as given in Table 6.4. On the other hand, the spectra corresponding to E* = 46.1 MeV and 59.6 MeV show no evidence of shell mediated asymmetric fission at any stage of multi-chance fission (see the spectra of *ch1* to *ch5* for 59.6 MeV and *ch1* to *ch4* for 46.1 MeV). The bottom panels (r),(s),(t) and (u) display the overall $Mass - TKE$ distribution, taking into account all fission chances. As

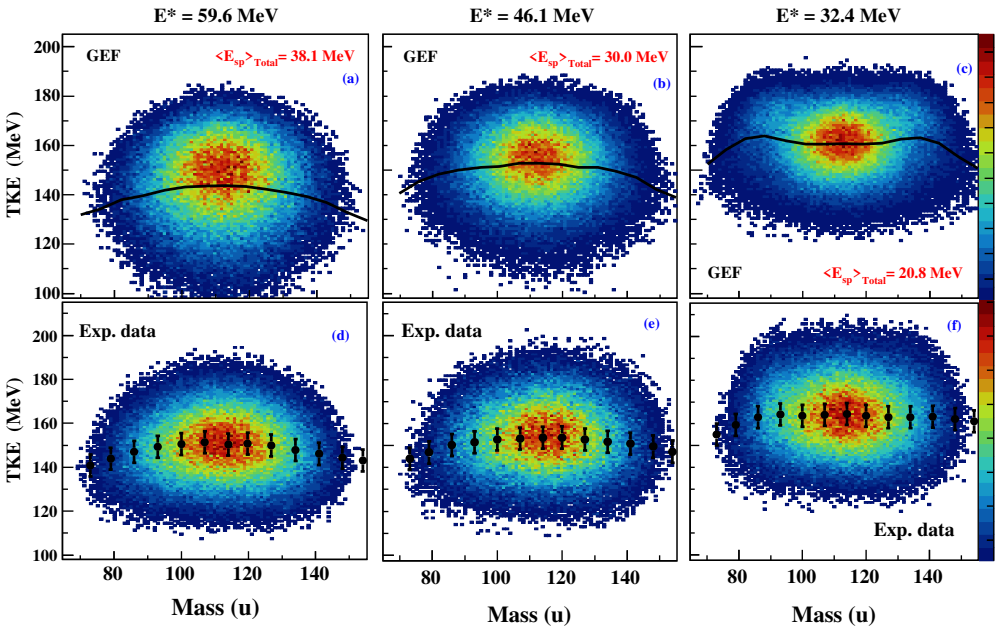

Figure 6.7: Comparison of experimental $Mass - TKE$ correlations in ^{227}Pa at E* = 59.6, 46.1 and 32.4 MeV. with GEF calculations. Panels (a)-(c) GEF calculations including multi-chance fission. The average excitation energy at saddle point, $< E_{sp} >$, are shown in each panel. The black solid lines indicate the average of kinetic energy. Panels (d)-(f) Measurements. The black circles with error bars represent the average of kinetic energy for a given mass bin.

observed in the panels (r) and (s), the $Mass - TKE$ plot at E* = 46.1 MeV and 59.6 MeV do not reveal any noticeable signs of shell effects. However, a modest enhancement in kinetic energy corresponding to asymmetric fission as well as an overall departure in the distribution compared to the higher energies are shown in the $Mass - TKE$ plot of E* = 24.2 MeV and 32.4 MeV (panels (t) and (u)). Current detailed analysis at each stage of sequential decay reveals that the asymmetric component in the final mass distribution is caused by the revival of shell effects at higher fission chances.

6.4.3 $Mass$ - TKE correlation : Measurements

The $Mass$ - TKE correlation estimated by GEF is compared with measurements made at E* = 59.6 MeV, 46.1 MeV, and 32.4 MeV in Figure 6.7. In order to account for the effect of finite mass resolution, GEF data were purposely

broadened by the present experimental mass resolution of σ_m=5 u. The solid line represents the GEF predicted average TKE as a function of fragment mass. The solid circle represents the averaged TKE over the 5 u mass bin. At three measured energies, the $Mass-TKE$ distribution predicted by GEF, accounting for all possibilities, closely matches the measured data. At E^* = 59.6 MeV and 46.1 MeV, the average TKE shows a parabolic relationship on fragment mass in both the measurement and GEF results. As shown in Figure 6.7(c) and (f), the average TKE is found to be almost constant for a range of fragment masses and moderately higher for asymmetric masses at E^* = 32.4 MeV. However, the observed spectrum does not show any noticeable asymmetric mass shoulders. At this energy, shell effects cause a significant amount of asymmetric fission and an increase in kinetic energy in the third and fourth chance fissions, as shown in Figure 6.6(k) and (o), which modifies the overall $Mass-TKE$ distribution. Therefore, asymmetric fission modes at higher chance fission may be attributed to the change in $Mass-TKE$ distribution observed when the excitation energy was reduced from 59.6 MeV to 32.4 MeV (Figure 6.7(d) and (f)). A closer look at the $Mass-TKE$ distributions in Figure 6.7 panels (d), (e), and (f) indicates that there may be a transition from symmetric to asymmetric fission at $E^* \approx 46$ MeV.

6.4.4 $Mass$ - ν_{pre} correlation

To determine the dependence of ν_{pre} on fragment mass, we further analyzed the GEF output for mass distribution corresponding to each chance fission for a given excitation energy. The mass gated pre-scission neutron multiplicity, ν_{pre}^M was calculated using the expression,

$$\nu_{pre}^M = \frac{\sum_{i=1}^{n}(i-1)\ N_i^M}{\sum_{i=1}^{n} N_i^M} \tag{6.9}$$

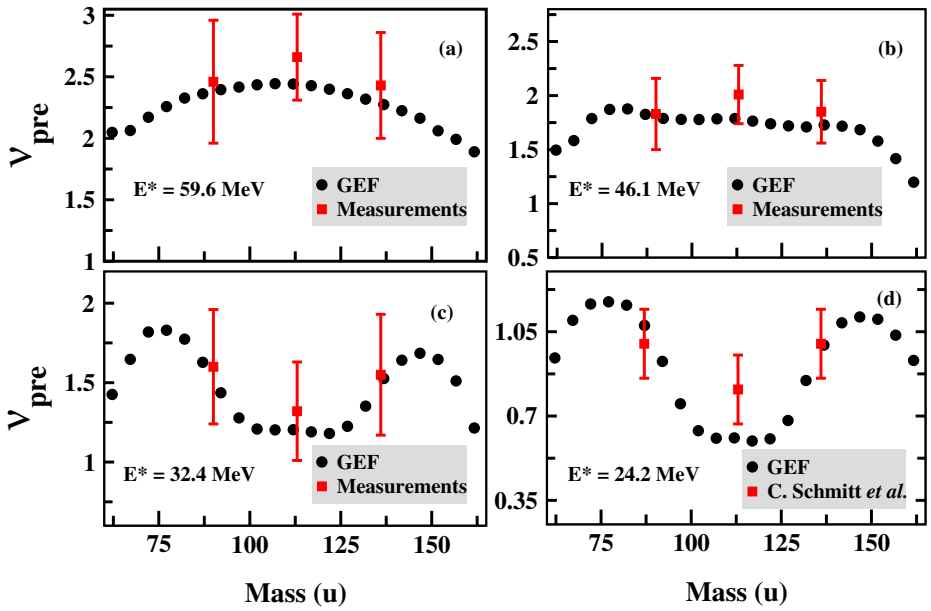

Figure 6.8: Correlation between experimental ν_{pre} and fragment mass compared with GEF model calculation for ^{227}Pa at E* = 59.6, 46.1, 32.4 and 24.2 MeV. Filled squares with error bars denote the ν_{pre} extracted from symmetric and asymmetric mass cuts to total mass distribution. Data of E* = 24.2 MeV is from [10].

where N_i^M is the fission yield for a given fragment mass M. The value of N_i^M for a given mass bin was obtained by averaging the multi chances according to their probability. The variation of ν_{pre} as a function of fragment mass is summarized in Figure 6.8. GEF results are compared to present measurements made at 59.6 MeV (Figure 6.8(a)), 46.1 MeV (Figure 6.8(b)) and 32.4 MeV (Figure 6.8(c)). Figure 6.8(d) shows a comparison of mass gated pre-scission neutron multiplicity of ^{227}Pa at 24.2 MeV reported in [10] with GEF calculation. According to GEF, due to multi-chance fission, shell effects are prevalent at this excitation energy which is displayed in the Figure 6.6(h), (l) and (u).

At E* = 59.6 MeV and 46.1 MeV, the measured data show higher ν_{pre} for symmetric mass division than for asymmetric mass. Similar findings were reported for compound nuclei at high excitation energies [11, 21]. This is attributed to the difference in the timescales of symmetric and asymmetric fission of the system at higher excitation energies [11]. At lower excitation energies, 32.4 MeV and 24.2 MeV (Figure 6.8(c) and (d)), higher ν_{pre} correlates with asymmetric

fission. GEF calculations, that account for the multi-chance nature of fission, reproduce similar $Mass - \nu_{pre}$ correlations at these energies. This indicates that at these two energies, multi-chance fission strongly influences the fission mode. $Mass - TKE$ correlation shown in Figure 6.6 also unambiguously indicates the presence of shell effects at higher fission chances for E* = 32.4 MeV and 24.2 MeV.

The chance fission probabilities given in Table 6.4 for 32.4 MeV shows that $\approx$ 43 % of fission occurs at $< E_{sp} > \approx$ 14.4 MeV (*ch3* and *ch4*, where the presence of shell effect was observed). Similarly, at E* = 24.2 MeV, the second and third chance fission (where shell effects were noticed) together account for $\approx$ 65 % of fission at $< E_{sp} > \approx$ 13.9 MeV. This suggests that even though the compound nucleus was formed at E* of 32.4 MeV and 24.2 MeV, pre-saddle neutron emission leads to the restoration of the shell effects when the excitation energy at the saddle point is greatly reduced, leading to asymmetric fission. Therefore, the correlation between higher ν_{pre} and asymmetric mass division can be interpreted as a feature of the fragment shell effect reinstated by multi-chance fission in actinide nucleus ^{227}Pa. For E* = 59.6 MeV and 46.1 MeV, GEF calculations predict multi-chance fission and an overall decrease in E_{sp} as shown in the Table 6.4. However, neither $Mass - TKE$ nor $Mass - \nu_{pre}$ distributions show significant evidence of shell- mediated asymmetric fission.

The saddle point excitation energy was sufficient for the attenuation of shell effects in ^{227}Pa formed at energies of 59.6 MeV and 46.1 MeV. In contrast, fission of neutron-rich compound nuclei formed by the MNT process shows evidence of shells even at higher E* up to $\approx$ 60 MeV [7, 22]. Dynamical model calculation using the Langevin approach by including MCF successfully reproduced these experimental mass spectra [12]. In neutron-rich CN, the neutron emission probability is higher than fission [9, 12, 23] and $< E_{sp} >$ of the fissioning nucleus is reduced, promoting shell-mediated mass asymmetric fission. Present work, together with works by others [7, 12, 13, 22] shows that the fission observables in

these two extreme scenarios (neutron-deficient CN formed by FMT and neutron-rich CN formed by MNT) can be explained by the proper inclusion of pre-saddle particle emission and the resulting saddle point excitation energy.

6.5 Summary and Conclusion

Using time of flight technique and fragment-neutron angular correlation, we have determined the mass distribution, prompt neutron multiplicities in the fission of ^{227}Pa populated by ^{19}F+^{208}Pb complete fusion at different excitation energies. The measurements were carried out for excitation energies as low as 32.4 MeV, which is $\approx$ 4 % below the Coulomb barrier and up to E* = 59.6 MeV. The influence of pre-scission neutron emission on mass division (symmetric or asymmetric) of ^{227}Pa was determined by investigating the variation of pre-scission neutron multiplicity as a function of fragment mass. Semi-empirical calculations within the framework of GEF model, incorporating multi-chance nature of fission, were carried out to determine the $Mass - TKE$ and $Mass - \nu_{pre}$ correlations in ^{227}Pa at measured excitation energies. The sequential fission decay incorporated in GEF model was ascertained by comparing the $< \nu_{pre} >$ at multiple energies with measurement.

For each excitation energy, the $Mass - TKE$ distribution corresponding to different fission chances was examined using the GEF model. From this, it is concluded that there is no noticeable asymmetric fission mediated by shell effects at E* = 59.6 MeV and 46.1 MeV according to $Mass-TKE$ correlation. Whereas, at E* = 32.4 and 24.2 MeV, the average TKE is found to be virtually constant over a range of fission fragment masses. This change in $Mass-TKE$ distribution as compared to the corresponding spectra at E* = 59.6 MeV and 46.1 MeV is attributed to the existence of asymmetric fission modes due to higher chance fission. The experimental $Mass - TKE$ distributions at these energies agree well with the overall trend anticipated by the GEF calculation.

In light of multi-chance fission, we have demonstrated the theoretical distri-

bution of pre-scission neutron multiplicity as a function of fragment mass. The measured $Mass - \nu_{pre}$ correlation and its variation with excitation energy are in good agreement with predictions from the GEF model. At higher excitation energies (46.1 and 59.6 MeV), ν_{pre} was seen to be larger for symmetric fission as reported in literature. However, higher ν_{pre} was correlated with asymmetric mass division at lower excitation energies (24.2 and 32.4 MeV). According to GEF calculations, higher chance fission significantly reduces the saddle point energy (E_{sp}) at these excitation energies. At these lower saddle point energies, shell effects are prominent which give rise to an interplay of asymmetric fission modes. From these results, it is concluded that the correlation of higher ν_{pre} with asymmetric fission than symmetric fission is a signature of shell effects reinstated by sequential fission decay. Though ^{227}Pa nucleus populated at 46.1 and 59.6 MeV also exhibit multi-chance fission and resultant decrease in saddle point excitation energy, the available excitation energy appears sufficient for the attenuation of shell effects.

Bibliography

[1] P. Moller, D. G. Madland, A. J. Sierk, and A. Iwamoto, Nature **409**, 785 (2001), https://doi.org/10.1038/35057204.

[2] V. S. Ramamurthy, S. S. Kapoor, and S. K. Kataria, Phys. Rev. Lett. **25**, 386 (1970), https://link.aps.org/doi/10.1103/PhysRevLett.25.386.

[3] E. K. Hulet, J. F. Wild, R. J. Dougan, R. W. Lougheed, J. H. Landrum, A. D. Dougan, M. Schadel, R. L. Hahn, P. A. Baisden, C. M. Henderson, R. J. Dupzyk, K. Sümmerer, and G. R. Bethune, Phys. Rev. Lett. **56**, 313 (1986), https://link.aps.org/doi/10.1103/PhysRevLett.56.313.

[4] U. Brosa, S. Grossmann, and A. Muller, Physics Reports **197**, 167 (1990), https://doi.org/10.1016/0370-1573(90)90114-H.

[5] N. Bohr and J. A. Wheeler, Phys. Rev. **56**, 426 (1939), https://link.aps.org/doi/10.1103/PhysRev.56.426.

[6] A. Turkevich and J. B. Niday, Phys. Rev. **84**, 52 (1951), https://link.aps.org/doi/10.1103/PhysRev.84.52.

[7] K. Hirose, K. Nishio, S. Tanaka, R. Léguillon, H. Makii, I. Nishinaka, R. Orlandi, K. Tsukada, J. Smallcombe, M. J. Vermeulen, S. Chiba, Y. Aritomo, T. Ohtsuki, K. Nakano, S. Araki, Y. Watanabe, R. Tatsuzawa, N. Takaki, N. Tamura, S. Goto, I. Tsekhanovich, and A. N. Andreyev, Phys. Rev. Lett. **119**, 222501 (2017), https://link.aps.org/doi/10.1103/PhysRevLett.119.222501.

[8] A. V. Ignatyuk, G. N. Smirenkin, and A. S. Tishin, Yad. Fiz. **21**, 485 (1975), https://www.osti.gov/biblio/4175339.

[9] K.-H. Schmidt, B. Jurado, C. Amouroux, and C. Schmitt, Nuclear Data Sheets **131**, 107 (2016), special Issue on Nuclear Reaction Data, https://doi.org/10.1016/j.nds.2015.12.009.

[10] C. Schmitt, J. Bartel, A. Surowiec, and K. Pomorski, Acta Physica Polonica B **34**, 2135 (2003).

[11] D. J. Hinde, D. Hilscher, H. Rossner, B. Gebauer, M. Lehmann, and M. Wilpert, Phys. Rev. C **45**, 1229 (1992), https://link.aps.org/doi/10.1103/PhysRevC.45.1229.

[12] S. Tanaka, Y. Aritomo, Y. Miyamoto, K. Hirose, and K. Nishio, Phys. Rev. C **100**, 064605 (2019), https://link.aps.org/doi/10.1103/PhysRevC.100.064605.

[13] A. C. Berriman, D. J. Hinde, D. Y. Jeung, M. Dasgupta, H. Haba, T. Tanaka, K. Banerjee, T. Banerjee, L. T. Bezzina, J. Buete, K. J. Cook, S. Parker-Steele, C. Sengupta, C. Simenel, E. C. Simpson, M. A. Stoyer, B. M. A. Swinton-Bland, and E. Williams, Phys. Rev. C **105**, 064614 (2022), https://link.aps.org/doi/10.1103/PhysRevC.105.064614.

[14] D. J. Hinde, A. C. Berriman, M. Dasgupta, J. R. Leigh, J. C. Mein, C. R. Morton, and J. O. Newton, Phys. Rev. C **60**, 054602 (1999), https://link.aps.org/doi/10.1103/PhysRevC.60.054602.

[15] K.-H. Schmidt and B. Jurado, Reports on Progress in Physics **81**, 106301 (2018), https://dx.doi.org/10.1088/1361-6633/aacfa7.

[16] C. Schmitt, K.-H. Schmidt, and B. Jurado, Phys. Rev. C **98**, 044605 (2018), https://link.aps.org/doi/10.1103/PhysRevC.98.044605.

[17] K. Hagino, N. Rowley, and A. Kruppa, Computer Physics Communications **123**, 143 (1999), https://doi.org/10.1016/S0010-4655(99)00243-X.

[18] Z. Huanqiao, L. Zuhua, X. Jincheng, X. Kan, L. Jun, and R. Ming, Nuclear Physics A **512**, 531 (1990), https://doi.org/10.1016/0375-9474(90)90085-Z.

[19] A. V. Karpov, P. N. Nadtochy, D. V. Vanin, and G. D. Adeev, Phys. Rev. C **63**, 054610 (2001), https://link.aps.org/doi/10.1103/PhysRevC.63.054610.

[20] Y. Nagame, I. Nishinaka, K. Tsukada, Y. Oura, S. Ichikawa, H. Ikezoe, Y. Zhao, K. Sueki, H. Nakahara, M. Tanikawa, T. Ohtsuki, H. Kudo, Y. Hamajima, K. Takamiya, and Y. Chung, Physics Letters B **387**, 26 (1996), https://doi.org/10.1016/0370-2693(96)01027-1.

[21] D. Hilscher and H. Rossner, Ann. Phys. Fr. **17**, 471 (1992), https://doi.org/10.1051/anphys:01992001706047100.

[22] R. Léguillon, K. Nishio, K. Hirose, H. Makii, I. Nishinaka, R. Orlandi, K. Tsukada, J. Smallcombe, S. Chiba, Y. Aritomo, T. Ohtsuki, R. Tatsuzawa, N. Takaki, N. Tamura, S. Goto, I. Tsekhanovich, C. Petrache, and A. Andreyev, Physics Letters B **761**, 125 (2016), https://doi.org/10.1016/j.physletb.2016.08.010.

[23] M. Sin, R. Capote, M. Herman, and A. Trkov, Nuclear Data Sheets **139**, 138 (2017), special Issue on Nuclear Reaction Data, https://doi.org/10.1016/j.nds.2017.01.003.

Chapter 7

Summary and future outlook

Nuclear fission stands out as one of the most fascinating discoveries of 20^{th} century, profoundly impacting human life through its potential applications. Decades of dedicated research have significantly enhanced our comprehension of this phenomenon. However, there remain emerging areas in the field that warrant thorough investigation [1–3]. Experimentally, nuclear fission has been studied through the measurements of fragment mass distribution, angular distribution, mass - energy correlation, etc. The advancements in light particle detectors have expanded the scope of investigation to encompass particle multiplicities and their correlations with other fission observables. Notably, among the light particles, neutron emission width (Γ_n) is orders of magnitude higher than charged particles as it does not experience any Coulomb force. This makes neutron measurements an efficient probe in the study of nuclear reaction dynamics.

One of the intriguing area in the field of nuclear research that has emerged in recent years is the fission of neutron-rich actinide nuclei at higher excitation energies [2, 4]. This area of study holds significant importance, particularly in the context of applications such as the Accelerator Driven Sub-critical system (ADS) program, which aims to convert long-lived actinide nuclear waste into shorter-lived fission products. In a seminal work, Hirose *et al.* studied the

fission of neutron-rich actinides, formed through multi-nucleon transfer (MNT) [4]. Their observation of shell mediated asymmetric fission above $E^* \approx 50$ - 60 MeV stands remarkably away from the notions about fission at higher excitation energies. Subsequent theoretical calculations incorporating multi-chance fission have yielded reasonably accurate mass spectra. A series of experimental and theoretical studies, inspired from [2, 4], underscored the necessity to incorporate the multi-chance fission for the comprehensive description of fission in actinide nuclei [5–7].

The primary focus of the investigations presented in this thesis is to examine the influence of multi-chance fission on the decay of compound nuclei (CN) formed through the conventional full-momentum transfer (FMT) fusion process. Fusion via FMT typically results in the formation of neutron-deficient CN. In such systems, the emission probability, denoted as Γ_n, tends to be relatively low compared to neutron-rich nuclei formed through multi-nucleon transfer (MNT). However, the significant contribution of multi-chance fission can alter the fission modes, leading to substantial changes in the overall mass distribution. To address these phenomena, we conducted studies focusing on the role of multi-chance fission by measuring the mass distribution, mass-energy distribution, and additionally exploring the correlation of pre-scission neutrons with fragment mass. Detection of fast neutrons coinciding with fission events was accomplished using the National Array of Neutron Detectors (NAND) facility [8]. The thesis also provides a comprehensive overview of the facility and includes Monte Carlo calculations performed to assess its performance characteristics [8, 9].

A neutron detector array comprising a hundred BC501A organic liquid scintillators has been developed and installed at the Inter-University Accelerator Centre (IUAC) in New Delhi for the study of heavy ion induced fission and associated phenomena. These are commercially available 5” $\times$ 5” scintillators, each coupled to 5” diameter photomultiplier tubes. High detection efficiency, excellent neutron-gamma discrimination (FOM $\approx$ 1.6 at $\approx$ 0.5 MeV threshold), apprecia-

bly good time resolution ($\Delta T < 1$ ns), and excellent scintillation response to incident radiations make the BC501A detectors a versatile tool for fast neutron measurements. For the detection of binary fission fragments, a pair of large-area (20×10 cm^2), two-dimensional position-sensitive Multi-Wire Proportional Counters (MWPCs) with fast timing capabilities ($\Delta T \approx 500$ ps) have been designed and developed [10]. One major challenge in the fission studies employing multi-neutron arrays is the occurrence of cross-talk between neighbouring detectors. The cross-talk probability between a pair of BC501A detectors of NAND array was measured offline, using an ^{241}Am-^{9}Be source. For typical nuclear reaction studies where neutron emission per fragment is less than 5, cross-talk probability is estimated to be $\approx 1.4\times10^{-3}$ [8], consistent with the results obtained from the DEMON array [11]. The performance characteristics of BC501A detectors and the array were simulated using FLUKA Monte Carlo calculation code [12, 13]. FLUKA simulation was utilized to calculate the resolution parameters of 5" $\times$ 5" liquid cells, and the scintillation output for mono-energetic neutrons. The intrinsic efficiency was calculated and compared with measured data, in the neutron energy range of $\approx$ 0.5 MeV to 10 MeV. Based on the FLUKA calculation, it was concluded that the loss of neutron flux due to scattering from the chamber wall made of stainless steel is $\approx$ 12 %. Considering proper inclusion of geometric solid angle subtended by 100 detectors, integral efficiency, and the loss of flux due to scattering, the absolute efficiency of the full array was estimated to be $\approx$ 1.40 % at 0.5 MeV threshold energy.
Following optimal tuning and performance evaluation, the neutron array has been utilized for heavy ion induced fission research.

In our experimental approach, we conducted measurements of the mass distribution, average neutron multiplicity (ν_{pre}), and correlations between fragment mass and pre-scission neutron multiplicity ($Mass - \nu_{pre}$) in ^{227}Pa compound nucleus formed through the complete fusion reaction ^{19}F + ^{208}Pb, in the excitation energy range of $\approx$ 30 to 60 MeV [14]. To analyze the data, we employed well-

established techniques such as the velocity reconstruction method for deriving the mass distribution [15] and the moving source fit method [16] for determining neutron multiplicity. The results were analyzed theoretically using GEF model calculation, incorporating the multi-chance fission [17, 18]. While chance fission is present across all energy regimes above the neutron binding energy, its impact on mass division becomes particularly pronounced when the excitation energy at fission decreases significantly. Analysis of the $Mass - TKE$ correlation spectra at $E^* = 59.6$ MeV and 46.1 MeV suggests that multi-chance fission does not substantially influence the fission modes. However, at lower excitation energies of 32.4 MeV and 24.2 MeV, the measurement has shown the evidences of asymmetric fission. Theoretical analysis at these two energies reveals a significant occurrence of asymmetric fission driven by fragment shell effects. Thus the observed trend in $Mass-TKE$ distribution as compared to the corresponding spectra at higher energies is attributed to the presence of shell-influenced asymmetric fission modes facilitated by higher chance fission. This conclusion is ascertained by $Mass - \nu_{pre}$ correlation measurements performed at these energies. At higher excitation energies, the shape of mass distribution remains unaltered by pre-scission neutron emission. Whereas at lower excitation energies, $Mass-\nu_{pre}$ relationship indicates asymmetric fission when more number of pre-scission neutrons are emitted. GEF calculations suggest that higher chance fission substantially reduces the saddle point energy (E_{sp}). At these two lower energies, around 50 % of the fission occurs at $E_{sp} \approx 14$ MeV, where shell effects play a prominent role, promoting an interplay of asymmetric fission modes.

In conclusion, our findings suggest that the correlation of higher pre-scission neutron multiplicity with asymmetric fission is a signature of shell effects reinstated by multi-chance fission.

Future outlook

From the present study, we have concluded that the multi-chance fission plays a decisive role in the fission of actinide nuclei. It facilitates the revival of shell effect at higher fission chances that leads to an overall increase in the width mass distribution. By examining pre-scission neutrons in coincidence with fragment mass, we have been able to clearly discern shifts in fission modes. However, it is crucial to note that the widening of the mass distribution may not solely stem from shell effects but also from phenomena like deformation-dependent quasi-fission. Studies using deformed actinide targets near the Coulomb barrier energies have demonstrated that target orientation contributes to a broadened mass distribution due to incomplete mass equilibration [19–21]. Taking into account of our results, it's plausible that the final mass distribution comprises contributions from both quasi-fission and asymmetric fission facilitated by multi-chance fission. Our results suggest that a coincident measurement of fragment mass and ν_{pre} at energies near the Coulomb barrier could provide conclusive insights for a comprehensive understanding of fission phenomena. Further, the development of very large-area fragment detectors, spanning wide emission angle $\approx 5\ ^\circ$ - $90\ ^\circ$, will enable the exploration of di-nuclear system evolution through the measurements of $Mass - Angle$ correlation, $Mass - TKE$ correlation, and $Mass - \nu_{pre}$ correlations simultaneously.

The neutron detector array developed for the neutron-based research is one of the kind which enables a wide range of scientific inquiries. These include investigations into the impact of entrance channels on fission dynamics, nuclear dissipation at extremely high excitation energy and angular momentum, the timescale of fusion-fission and quasi-fission processes, among others. With upcoming accelerator facilities such as the High Current Injector (HCI) at IUAC, it would be possible to explore the heavy ion reaction dynamics using low-abundant beam species (^{13}C, ^{15}N, ^{22}Ne, ^{36,38}Ar, etc.), and at very low excitation energies.

Bibliography

[1] A. N. Andreyev, J. Elseviers, M. Huyse, P. Van Duppen, S. Antalic, A. Barzakh, N. Bree, T. E. Cocolios, V. F. Comas, J. Diriken, D. Fedorov, V. Fedosseev, S. Franchoo, J. A. Heredia, O. Ivanov, U. Köster, B. A. Marsh, K. Nishio, R. D. Page, N. Patronis, M. Seliverstov, I. Tsekhanovich, P. Van den Bergh, J. Van De Walle, M. Venhart, S. Vermote, M. Veselsky, C. Wagemans, T. Ichikawa, A. Iwamoto, P. Möller, and A. J. Sierk, Phys. Rev. Lett. **105**, 252502 (2010), https://link.aps.org/doi/10.1103/PhysRevLett.105.252502.

[2] R. Léguillon, K. Nishio, K. Hirose, H. Makii, I. Nishinaka, R. Orlandi, K. Tsukada, J. Smallcombe, S. Chiba, Y. Aritomo, T. Ohtsuki, R. Tatsuzawa, N. Takaki, N. Tamura, S. Goto, I. Tsekhanovich, C. Petrache, and A. Andreyev, Physics Letters B **761**, 125 (2016), https://doi.org/10.1016/j.physletb.2016.08.010.

[3] A. N. Andreyev, K. Nishio, and K.-H. Schmidt, Reports on Progress in Physics **81**, 016301 (2017), https://dx.doi.org/10.1088/1361-6633/aa82eb.

[4] K. Hirose, K. Nishio, S. Tanaka, R. Léguillon, H. Makii, I. Nishinaka, R. Orlandi, K. Tsukada, J. Smallcombe, M. J. Vermeulen, S. Chiba, Y. Aritomo, T. Ohtsuki, K. Nakano, S. Araki, Y. Watanabe, R. Tatsuzawa, N. Takaki, N. Tamura, S. Goto, I. Tsekhanovich, and A. N. Andreyev, Phys. Rev. Lett. **119**, 222501 (2017), https://link.aps.org/doi/10.1103/PhysRevLett.119.222501.

[5] S. Tanaka, Y. Aritomo, Y. Miyamoto, K. Hirose, and K. Nishio, Phys. Rev. C **100**, 064605 (2019), https://link.aps.org/doi/10.1103/PhysRevC.100.064605.

[6] A. C. Berriman, D. J. Hinde, D. Y. Jeung, M. Dasgupta, H. Haba,

T. Tanaka, K. Banerjee, T. Banerjee, L. T. Bezzina, J. Buete, K. J. Cook, S. Parker-Steele, C. Sengupta, C. Simenel, E. C. Simpson, M. A. Stoyer, B. M. A. Swinton-Bland, and E. Williams, Phys. Rev. C **105**, 064614 (2022), https://link.aps.org/doi/10.1103/PhysRevC.105.064614.

[7] M. J. Vermeulen, K. Nishio, K. Hirose, K. R. Kean, H. Makii, R. Orlandi, K. Tsukada, I. Tsekhanovich, A. N. Andreyev, S. Ishizaki, M. Okubayashi, S. Tanaka, and Y. Aritomo, Phys. Rev. C **102**, 054610 (2020), https://link.aps.org/doi/10.1103/PhysRevC.102.054610.

[8] N. Saneesh, K. Golda, A. Jhingan, S. Venkataramanan, T. Varughese, M. Kumar, M. Thakur, R. Mahajan, B. Behera, P. Sugathan, A. Chatterjee, and M. Chatterjee, Nuclear Instruments and Methods in Physics Research Section A: Accelerators, Spectrometers, Detectors and Associated Equipment **986**, 164754 (2021), https://doi.org/10.1016/j.nima.2020.164754.

[9] N. Saneesh, D. Arora, A. Chatterjee, K. Golda, M. Kumar, A. Vinodkumar, and P. Sugathan, Nuclear Instruments and Methods in Physics Research Section A: Accelerators, Spectrometers, Detectors and Associated Equipment **1013**, 165682 (2021), https://doi.org/10.1016/j.nima.2021.165682.

[10] A. Jhingan, N. Saneesh, M. Kumar, R. Mahajan, M. Thakur, G. Kaur, K. Kapoor, N. Kumar, M. Shareef, R. Dubey, S. Appannababu, E. Prasad, H. Singh, K. S. Golda, R. Ahuja, B. R. Behera, and P. Sugathan, Review of Scientific Instruments **92**, 033309 (2021), https://doi.org/10.1063/5.0029603.

[11] I. Tilquin, Y. E. Masri, M. Parlog, P. Collon, M. Hadri, T. Keutgen, J. Lehmann, P. Leleux, P. Lipnik, A. Ninane, F. Hanappe, G. Bizard, D. Durand, P. Mosrin, J. Péter, R. Régimbart, and B. Tamain, Nu-

clear Instruments and Methods in Physics Research Section A: Accelerators, Spectrometers, Detectors and Associated Equipment **365**, 446 (1995), https://doi.org/10.1016/0168-9002(95)00425-4.

[12] T. T. Böhlen, F. Cerutti, M. P. W. Chin, A. Fasso', A. Ferrari, P. G. Ortega, A. Mairani, P. R. Sala, G. Smirnov, and V. Vlachoudis, Nucl. Data Sheets **120**, 211 (2014).

[13] A. Ferrari, P. R. Sala, A. Fasso', and J. Ranft, CERN-2005-10(2005), INFN/TC_05/11, SLAC − R − 773 (2005).

[14] N. Saneesh, D. Arora, A. Chatterjee, N. Kumar, A. Parihari, C. Kumar, I. Ahmed, S. Kumar, M. Kumar, A. Jhingan, K. S. Golda, A. M. Vinodkumar, and P. Sugathan, Phys. Rev. C **108**, 034609 (2023), https://link.aps.org/doi/10.1103/PhysRevC.108.034609.

[15] D. J. Hinde, M. Dasgupta, J. R. Leigh, J. C. Mein, C. R. Morton, J. O. Newton, and H. Timmers, Phys. Rev. C **53**, 1290 (1996), https://link.aps.org/doi/10.1103/PhysRevC.53.1290.

[16] B. E. Watt, Phys. Rev. **87**, 1037 (1952), https://link.aps.org/doi/10.1103/PhysRev.87.1037.

[17] K.-H. Schmidt, B. Jurado, C. Amouroux, and C. Schmitt, Nuclear Data Sheets **131**, 107 (2016), special Issue on Nuclear Reaction Data, https://doi.org/10.1016/j.nds.2015.12.009.

[18] K.-H. Schmidt and B. Jurado, Reports on Progress in Physics **81**, 106301 (2018), https://dx.doi.org/10.1088/1361-6633/aacfa7.

[19] D. J. Hinde, M. Dasgupta, J. R. Leigh, J. C. Mein, C. R. Morton, J. O. Newton, and H. Timmers, Phys. Rev. C **53**, 1290 (1996), https://link.aps.org/doi/10.1103/PhysRevC.53.1290.

[20] D. J. Hinde, D. Y. Jeung, E. Prasad, A. Wakhle, M. Dasgupta, M. Evers, D. H. Luong, R. du Rietz, C. Simenel, E. C. Simpson, and E. Williams, Phys. Rev. C **97**, 024616 (2018), https://link.aps.org/doi/10.1103/PhysRevC.97.024616.

[21] K. Banerjee, T. K. Ghosh, S. Bhattacharya, C. Bhattacharya, S. Kundu, T. K. Rana, G. Mukherjee, J. K. Meena, J. Sadhukhan, S. Pal, P. Bhattacharya, K. S. Golda, P. Sugathan, and R. P. Singh, Phys. Rev. C **83**, 024605 (2011), https://link.aps.org/doi/10.1103/PhysRevC.83.024605.